

UNIVERSIDAD DE CANTABRIA  
DOCTORADO EN CIENCIA Y TECNOLOGÍA



Estudio de células cancerosas mediante  
métodos ópticos: polarimetría aplicada al  
análisis de la muerte celular inducida por  
quimioterapia

---

Study of cancer cells with optical methods:  
polarimetric techniques applied to the  
analysis of chemotherapy-induced cell death

Realizada por:  
**Andrea Fernández Pérez**

Dirigida por:  
**José María Saiz Vega y José Luis Fernández Luna**

TESIS DOCTORAL  
Santander, Noviembre de 2019  
Escuela de Doctorado de la Universidad de Cantabria



A Ma, Pa y Mani.

*"¿Qué se ve en un espejo que se mira en otro espejo?  
¿Lo sabes tú, Señora de los Deseos, la de los Ojos Dorados?"*  
La historia interminable - Michael Ende



## Agradecimientos

En primer lugar agradecer a mis directores **José María Saiz Vega** y **José Luis Fernández Luna** por su ayuda y guía y por todo el trabajo, ganas y esfuerzo que han puesto en la realización de esta tesis.

Además, este trabajo no se podría haber realizado sin la colaboración de:



La Universidad de Cantabria.



El grupo de Óptica (Dpto. de Física Aplicada) de la Universidad de Cantabria



La Unidad de Genética del Hospital Universitario Marqués de Valdecilla y el IDIVAL



The Applied Optics Polarimetry Group (LPICM) de L'École Polytechnique

Finalmente, y de manera personal, agradecer a mi familia, amigos y compañeros por vuestro apoyo, ayuda y ánimo a lo largo de estos 4 años. A todos, muchas gracias.

Finally, thanks to my family, friends and colleagues for your support, help and encouragement over these 4 years. To all of you, thank you very much.



## Abstract

Polarimetry has proven to be a very useful tool in problems that involve light-matter interaction, being a field of increasing activity with many successful applications in areas such as astronomy, agriculture, weather radar, environmental science, etc. Thanks to its non-destructive nature and its potential to identify local properties in media in which it propagates, nowadays imaging polarimetry is being used in biology and medicine, specifically, in the area of diagnosis. In this context, it is reasonable to consider that polarimetry could be used to identify cellular processes typically related to the development of tumors such as cell death, surface adhesion, mitosis, etc. These processes can alter locally the optical properties and, therefore, be detectable by the light that, when interacting with the biological system, changes its polarization .

These changes can be analysed using the Mueller matrix  $\mathbf{M}$ , which describes the polarimetric response of the medium. An image of each element of this matrix provides spatially resolved local information about the polarimetric behaviour. Because this matrix is a complex object, a transformation is often required to interpret the information and obtain some physical insight.

This thesis focuses on the study of different processes related to cell cultures by means of optical techniques, mainly optical polarimetry. The approach chosen has been the analysis of several cancerous cell lines following two main approaches. First, an experimental study of the efficacy of chemotherapy on several cancer cell lines was carried out in parallel with a polarimetric analysis of the samples at different times with respect to the application of the therapy. This has involved a specific work in sample preparation and has allowed a comparison of the values provided by the polarimetric measurement and the efficacy of the therapy. Secondly, we have developed a model to better understand the relationship between the processes of adhesion and separation of cells to a substrate and their polarimetric image. In the first case, we propose that this could be used to develop new protocols that serve to quantify and asses, in an objective way, the effect of certain chemotherapy drugs and the mortality of different cell lines. In the second case, the practical objective would be the search for a tool that helps to quantify the degree of adhesion of a cell population, which in turn can be related to cell death. Together, it is a tool that could help introduce procedures for evaluation and diagnosis, gaining both speed and independence from the observer.



## Resumen

La polarimetría ha demostrado ser una herramienta muy útil en problemas de interacción luz-materia, siendo un campo de actividad creciente con muchas aplicaciones exitosas en áreas tales como astronomía, agricultura, radar, meteorología, ciencia ambiental, etc. Gracias a su carácter no destructivo y a su potencial para identificar propiedades locales en los medios en los que se propaga, actualmente la polarimetría de imagen se está empleando en biología y medicina, en concreto en el área de diagnóstico. En este contexto, es razonable considerar que la polarimetría podría servir para la identificación de procesos celulares típicamente relacionados con el desarrollo de tumores, como la muerte celular, la adherencia a una superficie o la mitosis. Estos procesos pueden alterar las propiedades ópticas localmente y, por lo tanto, ser detectables para la luz que, al interactuar con el sistema biológico, cambia su polarización. Estos cambios se pueden analizar mediante la matriz de Mueller  $\mathbf{M}$ , que describe la respuesta polarimétrica de un medio. Una imagen de cada elemento de esta matriz proporciona información local, espacialmente resuelta, sobre el comportamiento polarimétrico. Debido a que esta matriz es un objeto complejo, a menudo se requiere una transformación para interpretar la información y obtener una visión física.

Esta tesis doctoral se centra en el estudio de diferentes procesos relacionados con cultivos de células mediante técnicas ópticas y, en particular, mediante técnicas polarimétricas de imagen. El enfoque elegido ha sido el análisis de muestras de células cancerosas siguiendo dos líneas principales. En primer lugar, un estudio experimental de la eficacia de la quimioterapia sobre varias líneas celulares cancerosas realizada en paralelo con un análisis polarimétrico. Esto ha conllevado un trabajo específico de preparación de muestras y ha permitido comparar los valores proporcionados por la medida polarimétrica con la eficacia de la terapia. En segundo lugar, hemos desarrollado un modelo para comprender mejor la relación entre los procesos de adhesión y separación de células a un sustrato y su imagen polarimétrica. En el primer caso, proponemos que esto podría usarse para desarrollar nuevos protocolos y ensayos que sirvan para cuantificar o evaluar de forma objetiva el efecto de ciertos medicamentos de quimioterapia y la mortalidad en diferentes líneas celulares. En el segundo caso, el objetivo práctico sería la búsqueda de una herramienta que ayude a cuantificar el grado de adhesión de una población de células, que a su vez puede estar relacionado con la muerte celular. En conjunto, se trata de una herramienta que podría ayudar a introducir procedimientos de evaluación y diagnóstico, ganando tanto velocidad como independencia del observador.



# Table of contents

<b>List of figures</b>	<b>xv</b>
<b>List of tables</b>	<b>xxi</b>
<b>1 Introduction</b>	<b>1</b>
1.1 Motivation . . . . .	2
1.2 Objectives and thesis overview . . . . .	4
<b>I THEORETICAL BACKGROUND</b>	<b>7</b>
<b>2 Light propagation and scattering</b>	<b>9</b>
2.1 Electromagnetic description . . . . .	9
2.2 Geometrical optics . . . . .	11
2.3 Reflection and refraction: Fresnel coefficients . . . . .	13
2.4 Light scattering by a spherical particle: Mie scattering . . . . .	15
2.5 Speckle and biospeckle . . . . .	17
<b>3 Polarization and Polarimetry</b>	<b>21</b>
3.1 Polarization of light . . . . .	21
3.2 Stokes vector and Mueller matrix formalism . . . . .	23
3.3 Polarimetric properties of any system . . . . .	26
3.3.1 Diattenuation . . . . .	27
3.3.2 Retardance . . . . .	27
3.3.3 Depolarization . . . . .	28
3.4 Mueller matrix analysis and decomposition . . . . .	29
<b>4 Fundamentals of cell biology and their optical response</b>	<b>35</b>
4.1 Introduction to cells . . . . .	35
4.1.1 Cell structure . . . . .	35
4.1.2 The cell cycle . . . . .	37
4.1.3 Cellular adhesion and cellular motility . . . . .	39
4.2 Cell death . . . . .	40
4.2.1 Apoptosis and necrosis . . . . .	41
4.2.2 Protocols to quantify cell death . . . . .	42
4.3 Optical properties of cells . . . . .	42
4.3.1 Cell Imaging . . . . .	43

<b>II</b>	<b>RESULTS</b>	<b>45</b>
<b>5</b>	<b>Polarimetry of cancerous cells</b>	<b>47</b>
5.1	Introduction . . . . .	47
5.2	Experimental setup . . . . .	48
5.2.1	Dual Rotating Compensator Polarimeter (UC) . . . . .	48
5.3	Initial tests . . . . .	51
5.3.1	Operating the setup with a birefringent media . . . . .	51
5.4	Cell samples . . . . .	52
5.4.1	Cell deposition methods . . . . .	53
5.4.2	Measurement of the Mueller matrices of cells . . . . .	54
5.4.3	Detections of PBS crystals . . . . .	56
5.5	Cell state assessment: apoptosis detection . . . . .	57
5.5.1	Polarimetric sensitivity to cell death: initial experiments . . . . .	59
5.5.2	Sample preparation and treatment: final protocol . . . . .	61
5.5.3	Evaluation of cell death . . . . .	62
5.6	Conclusions . . . . .	73
<b>6</b>	<b>Droplet-particle on a substrate: Curvature and degree of adherence</b>	<b>75</b>
6.1	Introduction . . . . .	75
6.2	Experimental setup . . . . .	76
6.2.1	Sample preparation and AFM measurements . . . . .	76
6.2.2	Polarimetric microscope (LPICM) . . . . .	78
6.3	Polarization model for normal incidence imaging . . . . .	80
6.4	Results . . . . .	82
6.4.1	Mueller matrix of spheres and spherical caps . . . . .	82
6.4.2	Adherence and matrix transformation parameters . . . . .	84
6.4.3	Influence of the numerical aperture . . . . .	88
6.5	Analysis and conclusions . . . . .	89
<b>7</b>	<b>Other approaches</b>	<b>91</b>
7.1	Mie Scattering . . . . .	91
7.1.1	Isolated sphere . . . . .	91
7.1.2	Coated sphere . . . . .	94
7.2	Discrete Dipole Approximation (DDA) . . . . .	97
7.3	Speckle and cell motility . . . . .	98
7.3.1	Experimental method . . . . .	98
7.3.2	Results . . . . .	100
7.4	Analysis and conclusions . . . . .	103
<b>8</b>	<b>Summary</b>	<b>105</b>
8.1	Completed tasks . . . . .	105
8.2	General conclusions . . . . .	106
8.2.1	Polarimetry in cancerous cells: cell death detection . . . . .	106
8.2.2	Adherence of spherical particles to a flat surface . . . . .	107
8.3	Future work . . . . .	108

<b>III APPENDIX</b>	<b>111</b>
<b>Appendix A Conferences contributions and publications</b>	<b>113</b>
A.1 Scientific publications . . . . .	113
A.2 Conference contributions . . . . .	113
<b>References</b>	<b>115</b>



# List of figures

2.1	Representation of an electromagnetic wave with their electric and magnetic field orthogonal to the propagation direction $z$ . . . . .	9
2.2	Representation of the Snell's law. Reflection and refraction of light at the surface between two mediums of different refractive index $n_1$ and $n_2$ . 13	
2.3	Reflectance and transmittance (left) and amplitude coefficients (right) given by the Fresnel equations for a wave travelling from glass ( $n = 1.5$ ) to air ( $n = 1$ ). Black dotted line shows the critical angle, $\theta_c$ , from which total internal reflection occurs. . . . .	15
2.4	A laser speckle pattern obtained from the light scattered by a metallic rough surface illuminated with a He-Ne laser ( $\lambda = 633$ nm). . . . .	17
3.1	Polarization ellipse for different values of the phase shift $\delta$ . $\varphi$ is the azimuth and $\chi$ is the ellipticity angle. Image taken from [1]. . . . .	22
3.2	Two different ways of representing the polarization of light. a) Polarization ellipse, modified from [1] and b) Poincaré sphere, taken from [1]. . . . .	23
4.2	Diagram of the cell cycle . . . . .	37
5.1	Schematic of the imaging dual rotating compensator polarimeter. The light source is a supercontinuum laser. A diffraction grating placed on a rotary stage (RS) together with a pinhole allow to select the desired wavelength. P1 and P2 are polarizers, R1 and R2 are retarders (quarter waveplate) and MO is the microscope objective. PSG and PSA stand for Polarization State Generator and Analyser respectively. 48	
5.2	Pictures of the two arms of the polarimeter: a) supercontinuum source and polarizer state generator (PSG) and b) Sample holder, microscope objective (MO), polarizer state analyser (PSA) and camera (CCD). . . . .	49
5.3	a) Mean values of the elements of the experimental calibration matrix (red) compared with the ideal one (4x4 identity matrix in blue) and b) image Mueller matrix of a calibration cycle. . . . .	50
5.4	Diattenuation ( $D_T$ ), anisotropy (A), total dichroism (TD), total birefringence (TB) and depolarization index (DI) obtained from a calibration measurement. Error bar is the standard deviation of 5 calibration cycles. . . . .	50
5.5	Units of the four samples of Scotch <sup>TM</sup> tape oriented in different directions used to perform the experimental test. Dashed lines represent the geometrical axis of the samples. . . . .	51
5.6	Linear and circular birefringence of several units of an anisotropic sample stacked on vertical position (left) and horizontal position (right). 52	

5.7	Linear and circular birefringence of several units of an anisotropic sample stacked at $45^\circ$ position (left) and $-45^\circ$ position (right). . . . .	52
5.8	Images of different situations encountered when testing several cell deposition methods. a) <i>Method 1</i> : drying and crystal formation (black arrows), b) <i>Method 3</i> : low contrast, c) <i>Method 4</i> : cells adhered to a cover showing a good contrast and d) inhomogeneities due to high concentration of agarose. . . . .	54
5.9	Experimental Mueller matrix image of a HT29 cell line performed at $\lambda = 634$ nm with a 5x microscope objective. . . . .	55
5.10	Total diattenuation ( $D_T$ ) and anisotropy ( $A$ ) for a sample of HT29 cell line. . . . .	56
5.11	Intensity images ( $m_{11}$ ) and total diattenuation parameter (TD) of some PBS crystals formed during measurements of cells using deposition <i>Methods 1</i> (right) and 2 (left). Big crystals are marked with a black ellipse and small ones with black arrows. . . . .	57
5.12	Metabolic activity of U937 and HT29 cells obtained by Alamar Blue test when treated with increasingly higher concentrations of cisplatin for 24 hrs. Error bars are the standard deviation of three measurements. Measurements were done at Unity of Genetics (Hospital Universitario Marqués de Valdecilla) . . . . .	58
5.13	Metabolic activity of HT29 cells obtained by Alamar Blue test when treated with increasingly higher concentrations of etoposide and doxorubicin for 24 hrs. Error bars are the standard deviation of three measurements. Measurements were done at Unity of Genetics (Hospital Universitario Marqués de Valdecilla) . . . . .	58
5.14	Metabolic activity of HT29 cells obtained by Alamar Blue test when treated with increasingly higher concentrations of cisplatin for 24 hrs. Error bars are the standard deviation of three measurements. Measurements were done at Unity of Genetics (Hospital Universitario Marqués de Valdecilla) . . . . .	58
5.15	Mean values of diattenuation in HT29 and MCF7 control samples and treated samples at 24hrs. and 48 hrs. after the treatment with cisplatin. Error bars represent the standard deviation of the mean values of the images taken in each case. . . . .	59
5.16	Mean values of diattenuation for three images of control samples and treated U937 cells sample ( $20 \mu\text{g}/\text{ml}$ of cisplatin). Error bars represent the standard deviation of the mean values of the images taken in each case. On the right side images taken with the microscope are shown. . . . .	60
5.17	Mean values of diattenuation for two images of control samples and treated HT29 cells with etoposide for 24 and 48 hrs. Error bars represent the standard deviation of the mean values of the images taken in each case. . . . .	61
5.18	Mean values of diattenuation and anisotropy for three images of control samples and treated HT29 cells with two different chemotherapy medications for 24 hrs. Error bars represent the standard deviation of the mean values of the images taken in each case. . . . .	61

5.19	U937 sample images taken by phase contrast microscopy. A) Control sample (non-treated). B), C) and D) 24, 48 and 72 hrs. treatment with 20 $\mu\text{g}/\text{ml}$ of cisplatin. White dashed square represent the size of the image taken with the polarimeter ( $640 \times 640$ pixels.) . . . . .	63
5.20	U937 image ( $m_{11}$ ) at 72 hrs. of treatment before and after binarizing.	64
5.21	Images of individual cells taken by phase contrast microscopy at different time points of the treatment with cisplatin. The same magnification has been used in the capturing and rendering of these images. Images are $100 \times 100$ pixels. . . . .	64
5.22	Cell death of U937 cells over time treated with 20 $\mu\text{g}/\text{ml}$ of cisplatin evaluated with trypan blue exclusion test at several time points. Error bar is the standard deviation of three measurements. . . . .	65
5.23	Metabolic activity of U937 cells following a treatment with cisplatin at different time points using the Alamar Blue assay. a.u., arbitrary units. Error bar is the standard deviation of three measurements . . .	65
5.24	Mueller matrix images of U937 samples at 4 time points during a treatment with 20 $\mu\text{g}/\text{ml}$ of cisplatin. . . . .	66
5.25	Mean diattenuation ( $D_T$ ) of each of the five images taken from control and cisplatin treated samples of U937 cells. Figure a) shows the 5 measurements taken for each time in the first experiment. Figure b) shows the mean values at each time for the triplicate experiment (numbered as 1, 2 and 3). Data is shown before ( $\square$ , dashed bars) and after ( $\bullet$ , solid line) applying the the correction given by Eq. 5.1. When the bar is not duplicated means that $f_c = 1$ for the measured image and no filling correction is required. Error bars represent the standard deviation of the image. . . . .	67
5.26	Mean total diattenuation, anisotropy, total birefringence, total dichroism and depolarization index of the 5 measurements made at each time in the first experiment. Data is shown before ( $\square$ , dashed bars) and after ( $\bullet$ , solid line) applying the correction given by Eq. 5.1. When the bar is not duplicated means that $f_c = 1$ for the measured image. Error bars represent the mean standard deviation of the 5 images of each parameter. . . . .	68
5.27	Mean values of the diattenuation ( $D_T$ ) obtained from the triplicate experiment with U937 cells as a function of cell death. Values of the diattenuation directly obtained from the image ( $D_i$ ) and diattenuation from cells corrected by Equation 5.1 ( $D_c$ ) are represented with $\square$ and $\bullet$ respectively. Error bars represent the mean standard deviation of the 3 experiments. . . . .	69
5.28	Total diattenuation images ( $D_T$ ) of U937 cells at different times of the treatment with 20 $\mu\text{g}/\text{ml}$ of cisplatin. . . . .	70
5.29	Death of THP1 cells over time treated with 20 $\mu\text{g}/\text{ml}$ of cisplatin evaluated with trypan blue exclusion test (left). Metabolic activity of THP1 cells under the same treatment using the Alamar Blue assay. a.u., arbitrary units (right). . . . .	71

5.30	Mean total diattenuation ( $D_T$ ), anisotropy ( $A$ ), total birefringence ( $TB$ ), total dichroism ( $TD$ ), depolarization index ( $D_I$ ) of the 5 measurements made for each sample of THP1. Error bars represent the mean standard deviation of the 5 images of each parameter. . . . .	72
5.31	Mean values of the diattenuation ( $D_T$ ) obtained from the triplicate experiment with THP1 cells as a function of the cell death. Error bar is the mean standard deviation of the diattenuation images over the three experiments. . . . .	73
6.1	Images of biological cells adhered to a microscope slide (left) and latex spheres of 10 $\mu\text{m}$ diameter deposited on a glass substrate (right). Scale is the same for both images. . . . .	76
6.2	Schematics of the melting process of a latex sphere on a glass substrate (above). Profile of a melted sphere (dashed red line) ( $a_m = 8.6 \mu\text{m}$ , $h_m = 3.3 \mu\text{m}$ .) compared to the profile of a spherical cap (blue) that produces de best fit. The inset shows the AFM measurement of a partially melted sphere. . . . .	77
6.3	Experimental AFP measurement of the profile of three latex particles corresponding to different melting stages. . . . .	77
6.4	Schematic illustration of the multimodal imaging polarimetric microscope in transmission configuration. The position of the PSG, the PSA, the illumination (OM1) and the imaging (OM2) objectives are shown. The other acronyms refer to the spectral filter (SF), the illumination aperture diaphragm (Ill AD), the illumination field diaphragm (Ill. FD), the imaging aperture diaphragm (Im AD), and the imaging field diaphragm (Im. FD). The position of the back focal planes of the illumination (OM1 BFP) and imaging objectives (OM2 BFP) are also shown. . . . .	78
6.5	a)Description of rays travelling inside a meridian plane and the cartesian components of the incident electric field. R: reflected rays will interfere with direct rays (D) travelling outside the sphere. T: transmitted rays (the virtual path required to reach the observation plane is shown as a dashed line). b) Meridian plane $\Pi$ corresponding to a given azimuth $\varphi$ . . . . .	80
6.6	Comparison between experimental (right) and calculated (left) Mueller matrix of a latex sphere of radius 5 $\mu\text{m}$ through coherent polarization-sensitive ray tracing simulation for equatorial focusing in XY (above) and SP coordinates (below). Two color scales are shown for diagonal (d) and non-diagonal (nd) elements. Black dashed line shows the actual boundary of the sphere ( $r = 5\mu\text{m}$ ). . . . .	83
6.7	Experimental Mueller matrix of a latex melted sphere in x-y coordinates (right) and the Mueller matrix obtained through ray tracing simulation for substrate focusing and for the same volume than the sphere shown in the left. Curvature radius $r = 7.2 \mu\text{m}$ (left) in XY coordinates. The colorbar scale is shown for diagonal elements (d) and for non-diagonal elements (nd). For reference, black dashed lines shows the size of the original sphere ( $r = 5\mu\text{m}$ ). . . . .	84

6.8	Experimental measurements of dichroism and birefringence in SP coordinates for a latex sphere ( $r = 5 \mu\text{m}$ ). $LD$ is linear dichroism in x-y direction, $LD'$ is linear dichroism in $45^\circ$ direction, $CD$ is circular dichroism and $TD$ is total dichroism. Similar label criterion is used for birefringence. . . . .	85
6.9	Experimental results in SP coordinates for total linear dichroism (TLD) and total linear birefringence (TLB) of (a) a complete sphere, and (b-d) increasingly melted spheres ( $melt1$ , $melt2$ and $melt3$ ). Blue lines represent the azimuthal average of the cross-section. . . . .	86
6.10	a) Evolution of the azimuthal average of the cross section of total linear dichroism, $TLD$ , with the increase of the melting degree, b) The same for total linear birefringence, $TLB$ . . . . .	86
6.11	a) Evolution of the maxima of the cross-sections for $TLD$ and $TLB$ with the apparent radius $a$ . b) Table with the apparent traversal radius, $a$ , and the associated values for the radius of curvature of the spherical cap, $r$ , and the relative height of the cap, or aspect ratio, $h/a$ . . . . .	87
6.12	Comparative between experimental cross-sections of element $m_{12}$ of the four samples (b) and the ones simulated with the radii estimated in Figure 6.11b (a). . . . .	87
6.13	Influence of the numerical aperture in the number of visible rings. Experimental measurements of element $m_{12}$ of the Muller matrix of a $r = 5 \mu\text{m}$ sphere(below) compared to simulation (above) for two values of the $NA$ . . . . .	88
6.14	Numerical aperture at which the first interferential ring becomes visible as a function of the melting degree ( $h/a$ ) of the particle. Calculation is made for individual cases of $h/a$ (red squares), and the black dashed line is a second order polynomial fit. The inset shows two experimental measurements of element $m_{12}$ for a $NA = 0.6$ (horizontal blue line) and two different melting degrees of the particles. . . . .	89
7.1	Mueller matrix at $\lambda = 500 \text{ nm}$ for an isolated sphere in water ( $n_w = 1.33$ ) with radius $r = 5 \mu\text{m}$ and refractive index $n = 1.36$ . . . . .	92
7.2	Mueller matrix at $\lambda = 500 \text{ nm}$ for an isolated sphere in water ( $n_w = 1.33$ ) with radius $r = 5 \mu\text{m}$ and several refractive indices. . . . .	92
7.3	Mueller matrix at $\lambda = 500 \text{ nm}$ for an isolated sphere in water ( $n_w = 1.33$ ) with refractive index $n = 1.36$ and several radii. . . . .	93
7.4	Mueller matrix at several wavelengths for an isolated sphere in water ( $n_w = 1.33$ ) with radius $r = 5 \mu$ and refractive index $n = 1.36$ . . . . .	93
7.5	Mueller matrix for a coated sphere in water ( $n_w = 1.33$ ) with radius $r_1 = 2 \mu\text{m}$ and $r_2 = 5 \mu\text{m}$ and refractive index $n_1 = 1.37$ and $n_2 = 1.35$ . . . . .	94
7.6	Mueller matrix of a coated sphere in water ( $n_w = 1.33$ ) with radius $r_1 = 2 \mu\text{m}$ , $r_2 = 5 \mu\text{m}$ and index $n_2 = 1.35$ . Index $n_1$ varies. . . . .	95
7.7	Mueller matrix of a coated sphere in water ( $n_w = 1.33$ ) with radius $r_1 = 2 \mu\text{m}$ , $r_2 = 5 \mu\text{m}$ and refractive index $n_1 = 1.37$ . Index $n_2$ varies. . . . .	95
7.8	Mueller matrix of a coated sphere in water ( $n_w = 1.33$ ) with variable radius $r_1$ , $r_2 = 5 \mu\text{m}$ and refractive index $n_1 = 1.37$ and $n_2 = 1.35$ . . . . .	96

---

7.9	Mueller matrix of a coated sphere in water ( $n_w = 1.33$ ) with radius $r_1 = 2 \mu\text{m}$ , variable $r_2$ and refractive index $n_1 = 1.37$ and $n_2 = 1.35$ . . .	96
7.10	Geometry to study adherence of spherical particles to surfaces (left) and dipole discretization in dipoles for DDA calculation (right). . . .	97
7.11	a) Experimental setup used to measure the speckle produced by cell samples. A solid state laser ( $\lambda = 650 \text{ nm}$ ) illuminates a Petri dish with cells in R10 medium and a CCD camera captures images of the speckle signal at fixed time intervals. b) One image of the speckle pattern produced by $5 \times 10^5$ JURKAT cells. . . . .	99
7.12	Speckle correlation functions for three different experiments with HT29 cells in R10 medium. Fits to Equation 7.3 are shown with dashed lines	101
7.13	Evolution of four 15 min-long successive measurements of the speckle correlation of HT29 cells in R10 medium. Similar decay is observed independently of the initial time chosen for the measurement. . . .	101
7.14	Speckle correlation functions of $5 \times 10^6$ and $10^6$ HT29 and JURKAT cells in R10 medium. Fits to Equation 7.3 are shown with dashed lines.	102

# List of tables

3.1	Mueller matrix of common optical systems. $\alpha$ is the azimuth of a diattenuator and $\delta$ is the retardance of a retarder. . . . .	34
5.1	$p$ -values for each possible couple of sets of measurements of the first experiment (C is control) after the filling factor correction. Values with $p < 0.01$ mean a high significance, values between $0.01 < p < 0.05$ mean significant and values of $p > 0.1$ are not significant. . . . .	67
7.1	Values of the coefficients $a$ , $b$ , $c$ and $d$ obtained after fitting the speckle correlation decay to a sum of two exponential functions (Equation 7.3) for three independent experiments with HT29 cells. Values of $R - squared$ are also presented for each case. . . . .	102
7.2	Values of the coefficients $a$ , $b$ , $c$ and $d$ obtained after fitting the speckle correlation decay to a sum of two exponential functions (Equation 7.3) for four experiments with HT29 and JURKAT cells at two concentrations. Values of $R - squared$ are also presented for each case. .	103



# Chapter 1

## Introduction

There were an estimated 18 million cancer cases around the world in 2018: 9.5 million cases affected men and 8.5 million affected women [2]. The most common cancers globally are lung and breast, followed closely by prostate, colorectal, stomach and skin<sup>1</sup>. Cancer is the leading cause of death worldwide with more than 9.6 million deaths in 2018. Cancer with the highest mortality rate are lung, colorectal, stomach, liver and breast. Prevention, diagnosis and treatment have greatly improved in the last decades. It is estimated that in 2019, cancer will cause 1.4 millions of deaths in Europe, 5% less than five years ago<sup>2</sup>. However, the economic impact of cancer is substantial and it is raising. The total cost attributable to the disease in 2010 was around US\$  $1.16 \times 10^{12}$ , a non-negligible dimension of the problem. Both the human and the economic impacts are closely related to some specific problems: early diagnosis is not always available, and treatments are not as efficient in an advanced phase of development. Because of this, great efforts are being dedicated to prevention, early detection and efficient and inexpensive diagnose of cancer. Even so, there is still a long way to go.

Typical methods used to diagnose cancer include blood, urine or other body fluid tests since high or low presence of certain substances can be a sign of cancer. Also, imaging procedures such as MRI (Magnetic Resonance Imaging), PET scan (Positron Emission Tomography), CT scan (Computed Tomography), X-rays, nuclear scan or ultrasounds are used to localize the areas affected by the tumor<sup>3</sup>. Finally, in most cases, a biopsy is necessary in order to find out what kind of cells are conforming the tumor. This technique consist on removing a sample of the tissue and then, a trained person (a pathologist) will examine the tissue and determine if it is cancer.

Regarding the treatment, there are many options depending on the type of cancer and how advanced it is. The most commonly employed are surgery, chemotherapy, radiation, immunotherapy, targeted therapy, hormone therapy and stem cell transplant. Different treatments pursuit different goals. Among these are: removing/shrinking a tumor, reducing its growth, killing or reducing the growth of certain cancer cells, avoiding the spreading of the cancer cells, ease some cancer symptoms, etc... Usually,

---

<sup>1</sup><https://www.wcrf.org/dietandcancer/cancer-trends/worldwide-cancer-data>

<sup>2</sup><https://www.who.int/news-room/fact-sheets/detail/cancer>

<sup>3</sup><https://www.cancer.gov/about-cancer>

several treatments are combined to increase the effectiveness and the chances to eliminate the disease.

Research in this area is continuously looking for new, or more effective ways to diagnose and treat cancer, reaching new advances constantly. In this task, interdisciplinary approaches play an important role in bringing and testing techniques that are of application in other areas. In this context it is worth mentioning the continuous improving of imaging techniques that allow for a better research and diagnose methods in this field. A recent example of this is the use of polarimetry, an optical tool that has demonstrated to have a major potential in the biomedical area. Polarimetry is based on the analysis of the interaction of matter and polarized light. It allows to know the optical properties of a material. Because its high sensitivity polarimetry has applications in a wide range of fields [3, 4]:

- ▷ *Industry*: quality control, metrology, surface characterization, design, fabrication and characterization of components, corrosion detection, profilometry...
- ▷ *Food and pharmacy*: food quality control, sugar measurement, cosmetics, quiral molecules measurements...
- ▷ *Atmospheric sensing*: characterization of aerosol particles, meteorology, atmospheric studies...
- ▷ *Astronomy*: study of stars and the Sun, study of planets and its atmosphere, measurement of magnetic fields, star dust analysis...
- ▷ *Biology and medicine*: cell microscopy, study of biological tissue, ophthalmology, glaucoma detection, diagnosis...
- ▷ *Radar*: target detection, surveillance, military applications...
- ▷ *Sensing and imaging*: study of lands, erosion, crops control, ocean and glacier monitoring, gas detection...
- ▷ *Other applications*: ellipsometry, measurements of nanoparticles, optical fibres, material classification and discrimination...

Among all these areas we are specially interested in biomedical applications to which this work is dedicated. In summary, polarized light outgoing a system carries information about the structure and morphology of such system. When the system in question is a biological sample, its polarimetric information can be used for the diagnosis and discrimination between healthy and cancerous tissue [5]. Moreover, it is a non-destructive technique since the action of light on matter does not necessarily involve the destruction of the tissue or sample.

## 1.1 Motivation

As has been mentioned, polarimetry has shown to be a very useful approach in problems that involve light-matter interaction. This is supported by its many successful

applications in a variety of fields, like astronomy, agriculture, weather radar, environmental science, etc. [6, 7, 4]. More recently, imaging polarimetry has become a field of increasing activity in medicine and biology because of its non-invasive nature and its potential to identify local properties in propagating media, something particularly important in the context of biomedical diagnosis [8]. Specifically, polarized light has been used to perform several studies over different tumor tissues [5] from colon [9, 10], cervix [11], thyroid or skin [12–14]. Other studies performed polarimetry and microscopy on both cancer and healthy blood samples, finding differences in physical parameters, like retardance or depolarization [15]. Regarding diattenuation, a recent study [16] has shown that this parameter is able to reveal different brain tissue properties. There are also studies that focus their attention in the analysis of the scattered light by suspensions of cancer and normal cells [17, 18], since it is well known that both types of cells present differences in their refractive index [19, 20].

Most of the work done in the area of biology focus the attention on tissues. Regarding biological cells, previous works show that some processes occurring in cells may alter their optical properties and therefore be potentially detectable under polarimetric observation. For instance, it can be a tool for the identification and discrimination of cancerous and normal cells as in [21], where some elements of the Mueller matrix measured on reflectance configuration and parameters such as diattenuation, depolarization and retardance show significant differences between healthy and cancer cells. Polarization has also been used together with confocal imaging to distinguish cancerous and normal prostate epithelial cells [22]. Other works also employed Mueller matrix imaging for discrimination and classification of microalgae and bacteria [23–25]. Moreover, polarization together with microscopy [26] could provide a new insight into molecular orientation in tissues and cells, proteins organization or DNA dynamic. In this context, it is reasonable to consider that polarimetry could also be useful for the identification of processes that promote changes inside the cell, like cell death, adhesion to a surface, mitosis, etc... In particular, we propose that this could be used to develop new protocols and assays to quantify the effect of certain chemotherapy medications on different cell lines, or to characterize other processes occurring in cells such as adhesion [27], an essential mechanism in cell communication and regulation.

In summary, when interacting with the biological system the change in the polarimetric properties of light is related to the properties of the sample. These changes can be analysed with the Mueller matrix  $\mathbf{M}$ , that fully characterizes such changes. When this is done in the context of an imaging system the resulting matrix provides local information about the polarimetric behaviour. Then, the images of polarimetric parameters should be eventually related with the mapping of biological properties of cells or tissues.

However, between the raw polarimetric data, given by  $\mathbf{M}$  [1] values, and any other that might be of medical use, there is a step in which physically interpretable parameters can play an important role. This physical mediation is commonly done through matrix transformation operations. In other words, by means of a proper decomposition, the optical properties of each part of the system can be described

in terms of parameters with a more clear physical interpretation. Different analysis methods are widely used in the bibliography to extract the information provided by the  $\mathbf{M}$ . The two most commonly used are Polar Decomposition (MMPD) [28] and the Mueller Matrix Transformation (MMT) [29]. A third one is the Mueller Matrix Differential Decomposition (MMDD) [30]. Each of them produces a set of parameters per point, therefore transforming  $\mathbf{M}$  images into other "physical" images that contain the optical properties and behaviour -or structural characteristics- of the sample under study.

## 1.2 Objectives and thesis overview

The main objective of this dissertation consists on the study of different properties and processes of living cells by means of optical and, in particular, polarimetric techniques. The approach chosen for this work has been the analysis of biological samples of special interest through the use of polarimetric measurements. From the beginning, the case of interest for this work has been that of cancerous cells. From there, two main lines have been followed: first, living cultures of cells have been prepared according to different strategies, in order to carry out experiments mostly on chemotherapy efficiency combined with their corresponding optical analysis. Secondly, we have developed a model to better understand the relation between the adhesion process of cells and its associated polarimetric imaging.

In this frame, there is a practical objective within our scope: the search of a tool that helps to automate and quantify cellular evolution. Such a tool could not only help introducing standard procedures, gaining both speed and independence from the observer, but also open a way to quantitatively study and comprehend processes occurring in cell cultures.

In order to achieve the main goals of this thesis, different tasks have been carried out, the main ones being:

1. Study the biology of cells: structure, cycle and processes. Become familiar with the protocols to handle, treat and analyse biological samples.
2. Design and optimize a protocol to prepare and measure Mueller matrices of biological samples.
3. Develop some tools that allow to decompose, analyse and plot Mueller matrices and polarimetric information from the experimental data to better understand the optical properties of these samples.
4. Perform a polarimetric study of several tumor cell lines, focusing in the effect of some chemotherapy drugs and in the detection of the death process.
5. Design a model able to reproduce the shape and polarimetric response of a cell in a controlled way and simulate Mueller matrices in conditions similar to the laboratory ones.

The present report has been divided in three parts:

- ▷ A first block containing the theoretical elements on which this work is based. It is divided in two chapters:
  - Chapter 2 presents an introduction to the basics of light propagation and scattering.
  - Chapter 3 includes the polarimetry foundations and the Mueller matrix formalism used to analyse data in this work.
  - Chapter 4 is focused on the biological part of this thesis, with basic concepts about the structure and functioning of cells.
  
- ▷ The second part is composed of three chapters of results, each of them focused on a different aspect of this thesis. These chapters are intentionally self-consistent, containing a brief motivation, the description of the experimental setup used to carry out the corresponding experiments, results and analysis and their own conclusions section:
  - Chapter 5 is focused on the polarimetric study of several cell lines, emphasizing the study on the effectiveness of chemotherapeutic treatments and the detection of cell death.
  - Chapter 6 presents a study of the adherence of a particle to a substrate, mimicking the geometry of a cell during the adhesion process and the degree of curvature of a cell to a substrate by means of a model of spherical and melted latex particles.
  - Chapter 7 contains a description of other approaches to the problem such as scattering of spheres and study of the speckle generated by cells.
  
- ▷ Finally, the third part, chapter 8, is a summary chapter where the tasks completed during the work are reviewed and the general conclusions of this dissertation are explained. Also, some future perspectives are presented.

The dissertation includes the Appendix A that contains the scientific publications and conference contributions carried out during the realization of the thesis.



# Part I

## THEORETICAL BACKGROUND



# Chapter 2

## Light propagation and scattering

According to the classical description, light is a transverse electromagnetic wave, i.e. a wave composed of two coupled electric and magnetic fields perpendicular to the propagating direction given by its wave vector  $\mathbf{k}$ , and also to each other (see Figure 2.1).

The knowledge of the electric field is sufficient for the characterization of the wave, and because of transversality, such field requires two coordinates to be properly defined within the transverse plane. This description of the electric field is often summarized with the term polarization and its formalism will be described in detail in the next chapter.

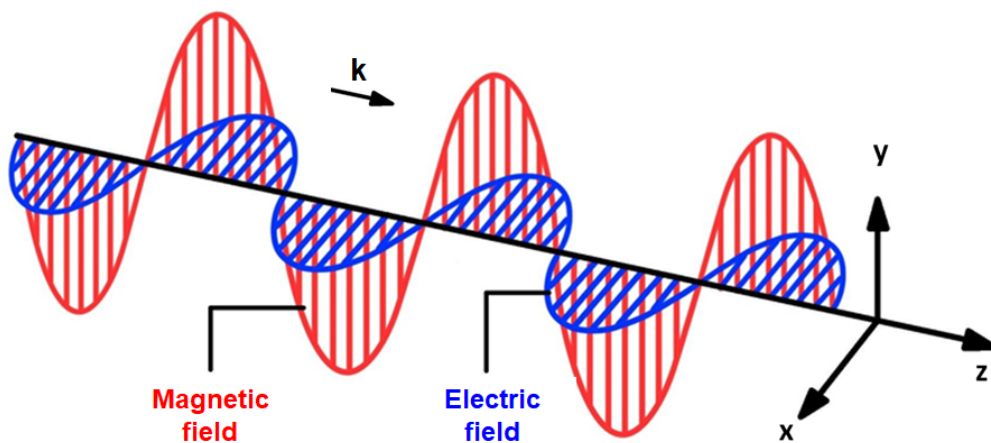


*Figure 2.1 - Representation of an electromagnetic wave with their electric and magnetic field orthogonal to the propagation direction  $z$ .*

In this chapter we summarize the wave description and propagation as well as some aspects of interest related to the interaction with matter.

### 2.1 Electromagnetic description

The starting point of the classical description of electromagnetic waves is the basic set of equations that governs the electromagnetic fields: the Maxwell equations [31]. In the International System of Units (SI), the equations can be written as:

$$\nabla \cdot \mathbf{D} = \rho \quad (2.1)$$

$$\nabla \times \mathbf{E} + \frac{\partial \mathbf{B}}{\partial t} = 0 \quad (2.2)$$

$$\nabla \cdot \mathbf{B} = 0 \quad (2.3)$$

$$\nabla \times \mathbf{H} = \mathbf{J} + \frac{\partial \mathbf{D}}{\partial t} \quad (2.4)$$

where  $\mathbf{E}$  is the electric field,  $\mathbf{H}$  is the magnetic field,  $\mathbf{B}$  is the magnetic induction and  $\mathbf{D}$  is the electric displacement,  $\mathbf{J}$  is the current density and  $\rho$  is the charge density.

At the same time,  $\mathbf{D}$  and  $\mathbf{H}$  are given by the equations:

$$\mathbf{D} = \epsilon_0 \mathbf{E} + \mathbf{P} \quad (2.5)$$

$$\mathbf{H} = \frac{\mathbf{B}}{\mu_0} - \mathbf{M} \quad (2.6)$$

being  $\mathbf{P}$  the electric polarization (electric dipole moment per unit of volume) and  $\mathbf{M}$  the magnetization (magnetic dipole moment per unit of volume).  $\mu_0$  and  $\epsilon_0$  are, respectively, the permeability and permittivity of vacuum.

The previous equations are completed with the constitutive relations of the electromagnetic field, which are related to the properties of the medium in which light is propagating:

$$\mathbf{J} = \sigma \mathbf{E} \quad (2.7)$$

$$\mathbf{B} = \mu \mathbf{H} \quad (2.8)$$

$$\mathbf{P} = \epsilon_0 \chi \mathbf{H} \quad (2.9)$$

where  $\sigma$ ,  $\mu$  and  $\chi$  are the medium conductivity, permeability and susceptibility respectively. These coefficients constitute what is often referred to as "optical properties" and depend on the constitutive nature of the medium under consideration.

Another important coefficient is the complex permittivity  $\epsilon$ , given by:

$$\epsilon = \epsilon_0(1 + \chi) + i \frac{\sigma}{\omega} \quad (2.10)$$

From Equations 2.1 to 2.4, wave equations can be deduced for  $\mathbf{E}$  and  $\mathbf{H}$  stating the conditions to be satisfied by the electromagnetic fields to constitute a physically realizable wave. Solutions can be expressed as a function of time-harmonics plane waves in the form:

$$\mathbf{E} = \mathbf{E}_0 \exp(-\mathbf{k}_2 \mathbf{r}) \exp(i\mathbf{k}_1 \mathbf{r} - i\omega t) \quad (2.11)$$

$$\mathbf{H} = \mathbf{H}_0 \exp(-\mathbf{k}_2 \mathbf{r}) \exp(i\mathbf{k}_1 \mathbf{r} - i\omega t) \quad (2.12)$$

where  $\mathbf{E}_0$  and  $\mathbf{H}_0$  are constant vectors compatible with Maxwell equations,  $\mathbf{r}$  is the position vector and  $\mathbf{k}$  is the wave vector  $\mathbf{k} = \mathbf{k}_1 + i\mathbf{k}_2$ .  $\mathbf{k}$  can be complex with  $\mathbf{k}_1$  and  $\mathbf{k}_2$  being real vectors. Then,  $\mathbf{E}_0 \exp(-\mathbf{k}_2 \mathbf{r})$  y  $\mathbf{H}_0 \exp(-\mathbf{k}_2 \mathbf{r})$  are the amplitudes of the electric and magnetic wave respectively and  $(i\mathbf{k}_1 \mathbf{r} - i\omega t)$  is the phase.

Interestingly, for an isotropic, charge-free, current-free medium, the implementation of the former solution in the Maxwell equations gives the transversality conditions already mentioned at the beginning of the chapter:

$$\mathbf{k} \cdot \mathbf{E}_0 = 0 \quad (2.13)$$

$$\mathbf{k} \times \mathbf{E}_0 = -\omega \epsilon \mathbf{E}_0 \quad (2.14)$$

$$\mathbf{k} \cdot \mathbf{H}_0 = 0 \quad (2.15)$$

$$\mathbf{k} \times \mathbf{H}_0 = \omega \epsilon \mathbf{H}_0 \quad (2.16)$$

The flux of energy energy carried by an electromagnetic wave that fulfils Equations 2.13 to 2.16 is represented by the Poynting vector,  $\mathbf{S}$ :

$$\mathbf{S} = \mathbf{E} \times \mathbf{H} \quad (2.17)$$

## 2.2 Geometrical optics

Geometrical optics [32] or ray optics describes light propagation in terms of rays. A ray represents the trajectory or path followed by light. It is oriented parallel to the Poynting vector, this is, perpendicular to the wavefront of the electromagnetic wave. Ray optics is a good approximation whenever the objects intercepting the wavefront are larger than the wavelength. (for example in the design of optical instruments).

When light propagates in a medium, its speed  $v$  gets reduced with respect to that of vacuum  $c$ . Therefore, the refractive index of such medium is defined to account for this:  $n = c/v$ .

Now, because light travels at different speed depending on the medium, a given geometrical path takes different times to be travelled by light, depending on the value of  $n$ . For this reason, the optical path is defined as:

$$L = ns \quad (2.18)$$

where  $s$  is the geometrical path.

For rays going through several media, the total optical path will be given by:

$$L_T = n_1 s_1 + n_2 s_2 + \dots \quad (2.19)$$

In relation to its refractive index, a medium can be homogeneous if its refractive index is constant and isotropic if it is independent of the propagating direction. If the refractive index depends on the direction it is called anisotropic. If it varies along the medium it is an heterogeneous medium.

Interestingly, the laws governing geometrical optics can be derived from the Fermat principle:

*"Light travels through the path in which it can reach the destination in the least time."*

Or, in modern terms, applying calculus of variations: real trajectories correspond to maximal points of the optical path function.

From this principle, the fundamental laws of geometrical optics are derived [32]:

- ▷ *Rectilinear propagation*: in a homogeneous medium, light travels in straight lines.
- ▷ *Reflection*: the angle of incidence on a surface is the same as the angle of reflection. This is, both the incident and the reflected ray form the same angle with the normal to the surface.
- ▷ *Refraction*: the trajectory followed by a light ray when it passes from a medium with refractive index  $n_1$  to a medium with refractive index  $n_2$  is given by Snell's law (Figure 2.2):

$$n_1 \sin(\theta_1) = n_2 \sin(\theta_2) \quad (2.20)$$

As long as  $n_2 > n_1$ , the incident ray will be refracted with an angle  $\theta_2$ , being  $\theta_2 < \theta_1$ . Conversely, if  $n_2 < n_1$  then  $\theta_2 > \theta_1$  and there exists a critic incident angle,  $\theta_c$ , for which the refracted angle will be equal to  $90^\circ$ . For larger values of the angle of incidence, there is no refraction and the light is totally reflected. This phenomenon is called total internal reflection (TIR).

- ▷ *Coplanarity*: the incident ray, the refracted ray and the normal to the surface have to be in the same plane, the incidence plane.
- ▷ *Reversibility*: the trajectory followed by light through a medium is reversible. This means that the optical path of a real ray (not virtual) does not depend on the propagation direction.

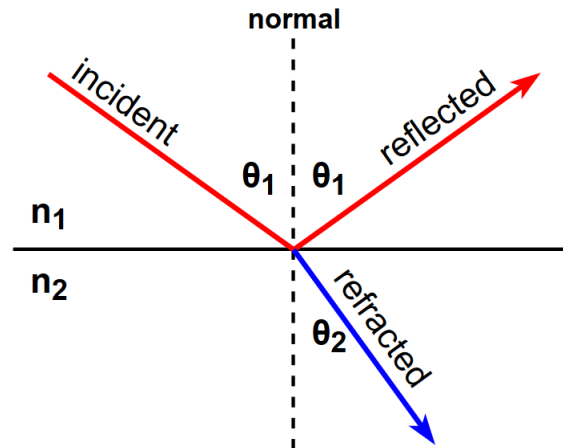


Figure 2.2 - Representation of the Snell's law. Reflection and refraction of light at the surface between two mediums of different refractive index  $n_1$  and  $n_2$ .

Regarding images, when an image is formed, the optical path  $L$  is constant for each of the rays. However, it is important to remark that in the formation of virtual images, the optical paths collected with the prolongation of rays must be accounted as negative in this formalism.

## 2.3 Reflection and refraction: Fresnel coefficients

When a plane wave hits the surface between two media of different refractive indices  $n_1$  and  $n_2$ , reflection and refraction occur. Fresnel equations describe the reflection and transmission of light on such an interface, providing the reflected and transmitted electric fields.

First, it is necessary to describe the incident field in two specific coordinates: perpendicular  $\perp$  to the plane of incidence (or s component) and parallel  $\parallel$  to the plane of incidence (or p component). These two components are considered separately by the equations in such a way that there are two reflection and two transmission coefficients, and the electric field amplitudes for transmission and reflection are given by:

$$(E_t)_\perp = t_\perp E_\perp \quad (2.21)$$

$$(E_t)_\parallel = t_\parallel E_\parallel \quad (2.22)$$

$$(E_r)_\perp = r_\perp E_\perp \quad (2.23)$$

$$(E_r)_\parallel = r_\parallel E_\parallel \quad (2.24)$$

where the Fresnel coefficients are given by [32]:

$$r_{\perp} = \frac{n_1 \cos(\theta_1) - n_2 \cos(\theta_2)}{n_1 \cos(\theta_1) + n_2 \cos(\theta_2)} \quad (2.25)$$

$$r_{\parallel} = \frac{n_1 \cos(\theta_2) - n_2 \cos(\theta_1)}{n_1 \cos(\theta_2) + n_2 \cos(\theta_1)} \quad (2.26)$$

$$t_{\perp} = \frac{2n_1 \cos(\theta_1)}{n_1 \cos(\theta_1) + n_2 \cos(\theta_2)} \quad (2.27)$$

$$t_{\parallel} = \frac{2n_1 \cos(\theta_1)}{n_2 \cos(\theta_1) + n_1 \cos(\theta_2)} \quad (2.28)$$

In these equations  $\theta_1$  and  $\theta_2$  are the incident and refraction angles respectively.

The reflectance  $R$  and transmittance  $T$  for s and p components (factors that account for the reflected or transmitted energy) are given by:

$$R_{\perp} = \left| \frac{n_1 \cos \theta_1 - n_2 \cos \theta_2}{n_1 \cos \theta_1 + n_2 \cos \theta_2} \right|^2 \quad (2.29)$$

$$R_{\parallel} = \left| \frac{n_1 \cos \theta_2 - n_2 \cos \theta_1}{n_1 \cos \theta_2 + n_2 \cos \theta_1} \right|^2 \quad (2.30)$$

And, because of energy conservation:

$$T_{\perp} = 1 - R_{\perp} \quad (2.31)$$

$$T_{\parallel} = 1 - R_{\parallel} \quad (2.32)$$

This description establishes a very important point for our calculation: in a change of medium the polarization considerations have to be done locally. As the plane of incidence may change from point to point in a curved surface the components of the incident field have to be obtained for each surface point.

For normal incidence ( $\theta_1 = \theta_2 = 0^\circ$ ) there is no distinction between polarization states. The reflectance is given by:

$$R = \left| \frac{n_1 - n_2}{n_1 + n_2} \right|^2 \quad (2.33)$$

And, as before  $T = 1 - R$ .

For a specific angle of incidence (the one that fulfils  $\theta_1 + \theta_2 = 90^\circ$ ),  $R_{\parallel}$  (see Figure 2.3) becomes zero. This angle is referred to as the Brewster angle. This implies that if a non polarized wave hits a surface between two different optical media at the Brewster's angle, then the reflected ray will be polarized in a direction perpendicular

to the plane of incidence.

As it has been mentioned, if a wave travels from a medium to another with a lower refractive index (from glass to air for example), total internal reflection will occur for  $\theta_1 > \theta_c$ , and all the light will be reflected ( $R_{\perp} = R_{\parallel} = 1$ ). As for the coefficients  $r_{\parallel}$  and  $r_{\perp}$  become complex, of modulus equal to 1, meaning that they do not change the amplitude of the wave, but just the phase.

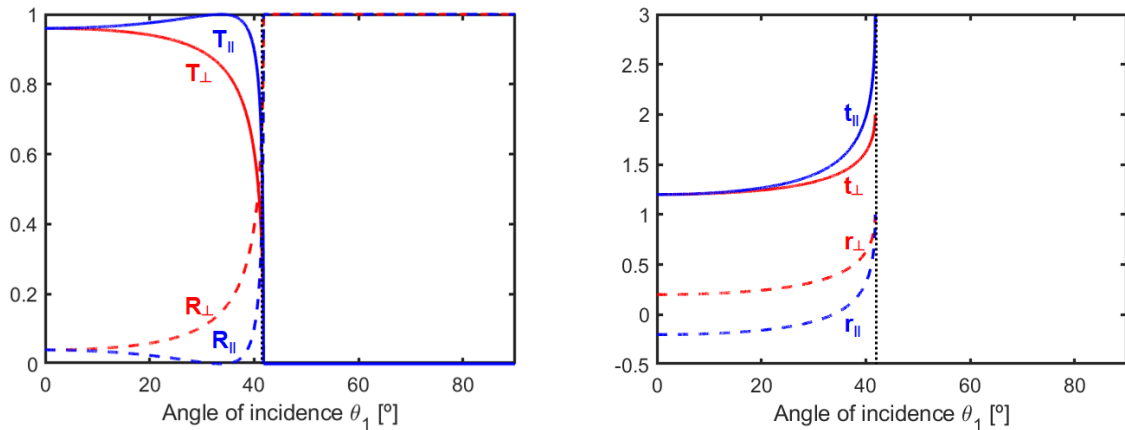


Figure 2.3 - Reflectance and transmittance (left) and amplitude coefficients (right) given by the Fresnel equations for a wave travelling from glass ( $n = 1.5$ ) to air ( $n = 1$ ). Black dotted line shows the critical angle,  $\theta_c$ , from which total internal reflection occurs.

## 2.4 Light scattering by a spherical particle: Mie scattering

Mie's theory [31] provides a general solution to Maxwell's equations that allows to calculate the scattered and absorbed field by a sphere of radius  $r$  and refractive index  $n$  illuminated by a plane wave of wavelength  $\lambda$ . The solution for a linear, isotropic, homogeneous medium can be expressed in terms of the vector harmonics. In this way, for a linearly polarized plane wave of wavelength  $\lambda$  incident on a spherical particle of radius  $r$  located in vacuum ( $\epsilon_0 = 1$ ), the incident electric and magnetic fields can be expressed as:

$$\mathbf{E}_i = E_0 \exp(i\mathbf{k} \cdot \mathbf{r}) \mathbf{e}_x \quad (2.34)$$

$$\mathbf{H}_i = H_0 \exp(i\mathbf{k} \cdot \mathbf{r}) \mathbf{e}_y \quad (2.35)$$

where  $\mathbf{e}_x$  and  $\mathbf{e}_y$  are the field unitary vectors in the  $x$  and  $y$  directions, respectively.  $\mathbf{k}$  is the wave vector and  $E_0$  and  $H_0$  are the field amplitudes.

This plane wave can be expanded in spherical harmonics  $\mathbf{M}$  and  $\mathbf{N}$  in the way [31]:

$$\mathbf{E}_i = E_0 \sum_{n=1}^{\infty} i^n \frac{2n+1}{n(n+1)} (\mathbf{M}_{o1n}^{(1)} - i\mathbf{N}_{e1n}^{(1)}) \quad (2.36)$$

$$\mathbf{H}_i = -\frac{k}{\omega\mu} E_0 \sum_{n=1}^{\infty} i^n \frac{2n+1}{n(n+1)} (\mathbf{M}_{e1n}^{(1)} - i\mathbf{N}_{o1n}^{(1)}) \quad (2.37)$$

where  $\omega$  is the angular frequency of the field,  $\mu$  the magnetic permeability of the medium, the superscript (1) indicates the spherical Bessel function of first kind,  $j_n(kr)$ ,  $\mathbf{M}_{o1n}^{(1)}$ ,  $\mathbf{M}_{e1n}^{(1)}$ ,  $\mathbf{N}_{o1n}^{(1)}$ ,  $\mathbf{N}_{e1n}^{(1)}$  are the vector spherical harmonics and  $e$  and  $o$  stand for even and odd .

The corresponding expression for the scattered field is:

$$\mathbf{E}_s = E_0 \sum_{n=1}^{\infty} i^n \frac{2n+1}{n(n+1)} (ia_n \mathbf{N}_{e1n}^{(3)} - b_n \mathbf{M}_{o1n}^{(3)}) \quad (2.38)$$

$$\mathbf{H}_s = -\frac{k}{\omega\mu} E_0 \sum_{n=1}^{\infty} i^n \frac{2n+1}{n(n+1)} (ib_n \mathbf{N}_{o1n}^{(3)} + a_n \mathbf{M}_{e1n}^{(3)}) \quad (2.39)$$

where the super index (3) refers the Hankel function,  $h_n^{(1)}$ , used for the calculus of the vector spherical harmonics and  $a_n$  and  $b_n$  are the important Mie scattering coefficients, representing respectively the electric and magnetic contribution to the scattered field. Although the summary is infinite, the number of terms that its necessary to consider gets reduced to a few in most practical problems. Because  $n$  represents the order of the field mode (dipole, quadrupole, etc.) values of  $n = 1$  and  $n = 2$  account for most of the small-particle scattering. If we assume that the magnetic permeability of the particle is equal to that of the medium, the coefficients can be expressed as a function of the Ricatti-Bessel functions  $\psi(\rho)$  and  $\zeta(\rho)$ :

$$a_n = \frac{m\psi_n(mx)\psi'_n(x) - \psi_n(x)\psi'_n(mx)}{m\psi_n(mx)\zeta'_n(x) - \zeta_n(x)\psi'_n(mx)} \quad (2.40)$$

$$b_n = \frac{\psi_n(mx)\psi'_n(x) - m\psi_n(x)\psi'_n(mx)}{\psi_n(mx)\zeta'_n(x) - m\zeta_n(x)\psi'_n(mx)} \quad (2.41)$$

where  $x$  is the size parameter ( $x = \frac{2\pi a}{\lambda}$ ) and  $m = \frac{n_{sphere}}{n_{medium}}$  is the relative refractive index.

From the scattering coefficients, the scattering and extinction cross-sections can be calculated:

$$Q_{ext} = \frac{2}{x^2} \sum_{n=1}^{\infty} (2n+1) \operatorname{Re}(a_n + b_n) \quad (2.42)$$

$$Q_{sca} = \frac{2}{x^2} \sum_{n=1}^{\infty} (2n+1) (|a_n|^2 + |b_n|^2) \quad (2.43)$$

$$Q_{abs} = Q_{ext} - Q_{sca} \quad (2.44)$$

In practice, there exist free software such as *MatScat* [33] (for its use in *Matlab*®) that allows to calculate the scattered field, coefficients, scattering matrix, etc. of an isolated sphere or coated sphere of the selected radius or refractive index.

## 2.5 Speckle and biospeckle

When highly coherent light, such as a laser, illuminates an inhomogeneous medium (i.e. a rough surface), the scattered light shows a peculiar intensity distribution with a granular random structure formed by bright and dark spots of variable shape. This pattern (see Figure 2.4), commonly known as speckle [34], is the result of temporally stationary interference of many waves of the same frequency but different amplitude and phase produced by the optical inhomogeneities randomly distributed over the illuminated region. Because of each scattering element contributes to every observation point  $P$ , the resulting pattern is extremely sensitive to any variation produced in the scattering elements.

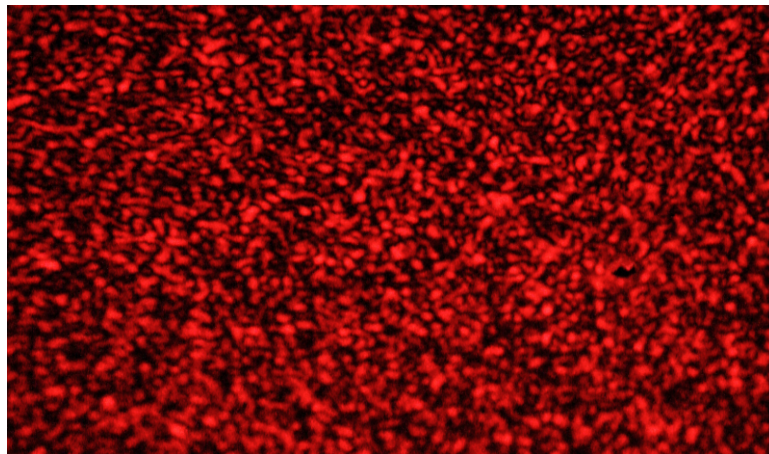


*Figure 2.4 - A laser speckle pattern obtained from the light scattered by a metallic rough surface illuminated with a He-Ne laser ( $\lambda = 633 \text{ nm}$ ).*

Although speckle was considered (and often still is) an undesirable effect, a noise to get rid of, it constitutes today a sensitive tool used in many applications, in a variety of fields. For example, one of the most consolidated applications is the measurement of surface roughness [35, 36] because some speckle parameters such as the contrast, spot size or binary image analysis [37, 38] can account for the roughness of a surface. Also it has applications in metrology, holography and in image processing [39] and it

is used to study object displacements and distortions (speckle interferometry) [40]. Moreover, analysis of the speckle size can be employed to determine the focusing of a laser system [41, 42]. In other field such as astronomy, speckle helps to overcome the limitation of terrestrial telescopes, allowing to obtain images of astronomical objects with higher resolution [43].

If a collimated coherent field of wavelength  $\lambda$  illuminates an optical rough surface with roughness larger than  $\lambda$ , the scattering phenomena can be understood as a series of spherical wavelets reflected by each point of the surface that will interfere at a certain point in space  $P(x, y, z)$ . Such wavelets will show a random distribution of phases and the resulting field at the point  $P$  will be the sum of all the contributions from each point  $j$  of the scattering surface. The complex amplitude in point  $P$  is [44, 45]:

$$A(P) = \frac{1}{\sqrt{N}} \sum_{j=1}^N a_j(P) = \sum_{j=1}^N |a_j| e^{i\phi_j} = \sum_{j=1}^N |a_j| e^{ikr_j} \quad (2.45)$$

where  $a_j(P)$  is the contribution to the field in  $P$  produced by the surface element  $j$ ,  $r_j$  is the distance from the  $j$  surface element to point  $P$  and  $\phi_j = kr_j$  is the phase of the  $j^{th}$  contribution.

If we assume that: i) the amplitude  $a_j$  and the phase  $\phi_j$  of each field are statistically independent; ii) they are also independent of the amplitude and phase of all the other field components; iii) the phases are distributed in the interval  $[-\pi, \pi]$ ; and iv) the number  $N$  of scattering centers is large, then the joint probability density function of the real and imaginary parts of the resultant field is:

$$p_{r,i}(A(r), A(i)) = \frac{1}{2\pi\sigma^2} \exp \left[ -\frac{(A(r))^2 + (A(i))^2}{2\sigma^2} \right] \quad (2.46)$$

where  $\sigma^2$  is a density function known as a circular Gaussian

$$\sigma^2 = \lim_{N \rightarrow \infty} \frac{1}{N} \sum_{k=1}^N \frac{\langle |a_k|^2 \rangle}{2} \quad (2.47)$$

From Equation 2.47 the probability density of the intensity  $p(I)$  and of the phase  $p(\Phi)$  are given by:

$$p(I) = \frac{1}{\langle I \rangle} e^{-\frac{I}{\langle I \rangle}} \quad \text{for } I \geq 0 \quad (2.48)$$

$$p(\Phi) = \frac{1}{2\pi} \quad -\pi \leq \Phi \leq \pi \quad (2.49)$$

where  $\langle I \rangle$  is the mean value of the intensity.

Finally, when the speckle is fully developed [46], its contrast (given by Equation 2.50) is equal to unity.

$$C = \frac{\sigma_I}{\langle I \rangle} \quad (2.50)$$

with  $\sigma_I = \langle I \rangle$  being the second moment (standard deviation) of the intensity distribution. This shows that the contrast of a fully developed speckle pattern is always unity.

When instead of having a coherent beam of light scattered by a static surface or material, we have an object with some kind of time variation, the resultant speckle pattern will appear as "boiling", with the bright and dark spots shifting and changing constantly. This is known as dynamic speckle. It is very common in samples such as paint drying, a surface expanding or contracting, and, of course, liquids, biological samples, small particles in suspension, or systems like foams (that expands) or metals (that suffer thermal expansion) for example.

There are two types of dynamic speckle:

- ▷ *Translational speckle*: the pattern does not change severely its overall distribution and suffers a translation when the scattering system is moved smoothly.
- ▷ *Boiling speckle*: the speckle patterns change completely when the internal relative positions in the scattering systems change (i.e. deformations). A new speckle pattern is formed in a very short time.

The term biospeckle [44] is referred to the dynamic speckle produced by biological samples. It carries information about the time associated to the changes in the biological sample. Studying the time evolution of the speckle pattern can be a very useful tool in knowing the speed of the processes that take place inside.

A possible way to proceed is to represent the time evolution of the correlation function between speckle images. Taking two images  $A$  and  $B$  separated in time, the correlation function can be defined as:

$$r = \frac{\sum_m \sum_n (A_{mn} - \bar{A})(B_{mn} - \bar{B})}{\sqrt{(\sum_m \sum_n (A_{mn} - \bar{A})^2 \sum_m \sum_n (B_{mn} - \bar{B})^2)}} \quad (2.51)$$

where  $\bar{A}$  is the mean value of the matrix  $A$  (an image of  $m \times n$  pixels) and  $\bar{B}$  is the mean value of the matrix  $B$  (an image  $m \times n$  pixels). For a dynamic system,  $r$  will decay with the interval of time  $\Delta t$  separating both images ( $\Delta t = 0 \rightarrow r = 1$ ). In this way  $A$  becomes the reference state and the shape of  $r(t)$  informs on the "decay" speed of the speckle pattern. If the state of the system is stationary, this decay curve can be averaged for many reference images  $A$  to obtain less noisy decay curves.

Biospeckle applications in biology and medicine have been increasing in recent years. For example it is used for medical imaging [47] mainly for the study of tumor microvasculature and to observe changes in blood flow [48]. Also, it has shown to be useful in the study of tumor tissue [49] and in skin cancer detection, where statistics moments of the polarization speckle patterns can account for different types of skin lesions such as melanoma [50]. Dynamic laser speckle can serve also to monitor the reaction of cancer cells (melanoma) to drugs [51]. Regarding the biological field, some studies report that the statistical analysis of the speckle pattern can be employed for the measurement of parasite and bacteria motility [52–54] and to study the viability of seeds [55].

# Chapter 3

## Polarization and Polarimetry

Polarimetry studies the polarization of electromagnetic waves and the changes induced in it when interacting with a material. For this purpose an appropriate formalism to describe the state of polarization of light is introduced.

### 3.1 Polarization of light

Polarization [1, 32] is an inherent property of transverse waves and, in particular, of every electromagnetic wave such as light. It can be defined as the specific evolution of the electric field  $\mathbf{E}$  associated to an electromagnetic wave.

Typically, the time evolution of the electric field is chosen to define the polarization of a wave. From it, the time evolution of  $\mathbf{D}$ ,  $\mathbf{H}$  and  $\mathbf{B}$  can be determined through Maxwell's equations and constitutive relations of the medium (Equations 2.1 to 2.9), so that the electromagnetic wave is fully described.

Polarized light can be expressed as the superposition of two plane waves propagating in an homogeneous and isotropic medium in the same direction ( $z$ ) with their electric vectors  $\mathbf{E}_x$  and  $\mathbf{E}_y$  perpendicular to each other. These waves can be represented as:

$$E_x(t) = A_1 \cos(\omega t - kz) \quad (3.1)$$

$$E_y(t) = A_2 \cos(\omega t - kz + \delta) \quad (3.2)$$

Where  $k = 2\pi/\lambda$  (being  $\lambda$  the wavelength),  $A_1$ ,  $A_2$  are the respective amplitudes and  $\delta$  is the phase shift between the two waves.

In each point of the space both vectors superpose giving a resulting vector  $\mathbf{E}$  (whose cartesian components are  $E_x$  and  $E_y$ , see Figure 3.2a) variable in time, in module and direction. If the orientation of the electric field varies randomly in the space then the light is said to be unpolarized or natural, as that coming from the sun or a light bulb. However, if the vector  $\mathbf{E}$  follows a predictable trajectory then the light is said to be polarized. If the projection of the field vector on the transverse plane describes a straight line, the light is said to be linearly polarized. If it describes a circumference then it is said to be circularly polarized and if it describes an ellipse it is elliptically polarized. Actually, linear and circular polarizations are particular cases

of the general elliptical polarization, described by the polarization ellipse (Equation 3.3) which fully describes a totally polarized state:

$$\left(\frac{E_x}{A_1}\right)^2 + \left(\frac{E_y}{A_2}\right)^2 - 2\left(\frac{E_x E_y}{A_1 A_2}\right) \cos \delta = \sin^2 \delta \quad (3.3)$$

The value of the phase shift  $\delta$  determines the type of polarization (Figure 3.1):

- ▷  $0 < \delta < \pi$ : right-handed elliptic polarization.
- ▷  $\pi < \delta < 2\pi$ : left-handed elliptic polarization.
- ▷  $\delta = 0, \pi, 2\pi$ : lineal polarization.
- ▷  $\delta = \pi/2 (A_1 = A_2)$ : right-handed circular polarization.
- ▷  $\delta = 3\pi/2 (A_1 = A_2)$ : left-handed circular polarization.

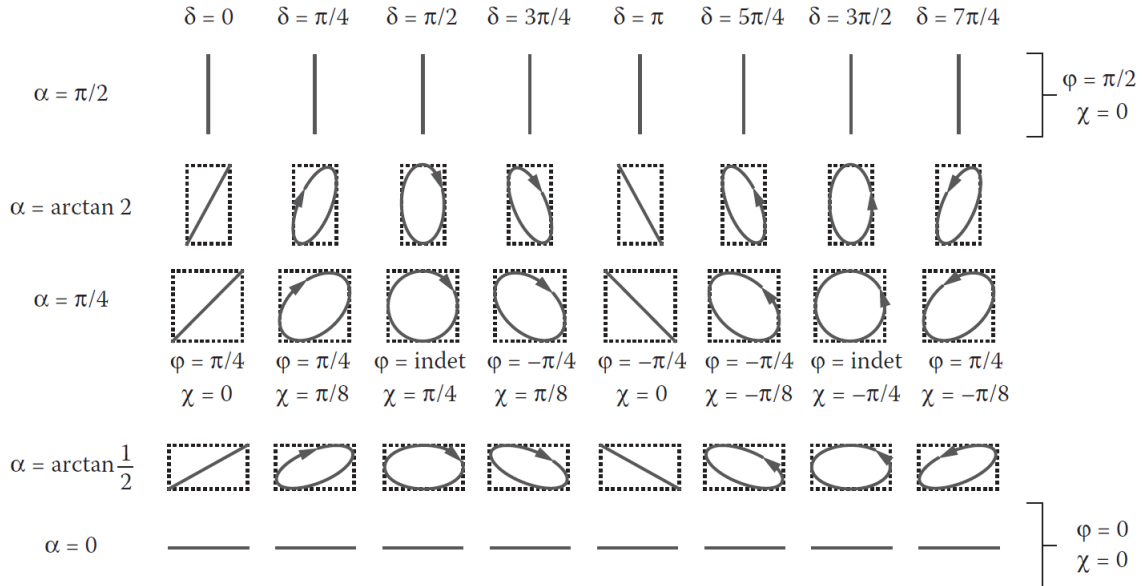


Figure 3.1 - Polarization ellipse for different values of the phase shift  $\delta$ .  $\varphi$  is the azimuth and  $\chi$  is the ellipticity angle. Image taken from [1].

The polarization ellipse is represented in Figure 3.2a. In the reference frame in which  $\mathbf{E}$  is defined, the ellipse is characterised with the angle  $\alpha$ , given by  $\alpha = \text{atan}(A_2/A_1)$ . A change of coordinates from x-y to X-Y can be done so that the ellipse is centered with semi-major and semi-minor axes  $a$  and  $b$  respectively and ellipticity  $e = (a-b)/a$ . Now, this ellipse is characterized by the azimuth  $\varphi (0 \leq \varphi \leq \pi) = \text{atan}(b/a)$  and the ellipticity angle  $\chi (-\pi/4 \leq \chi \leq \pi/4)$  which can be expressed as a function of  $\alpha$  and  $\delta$  with the equation:

$$\tan(2\varphi) = \tan(2\alpha) \cos(\delta) \quad (3.4)$$

Finally, the intensity  $I$  of the polarized light can be defined as:

$$I = \frac{nc}{8\pi}(A_1^2 + A_2^2) = \frac{nc}{8\pi}(a^2 + b^2) \quad (3.5)$$

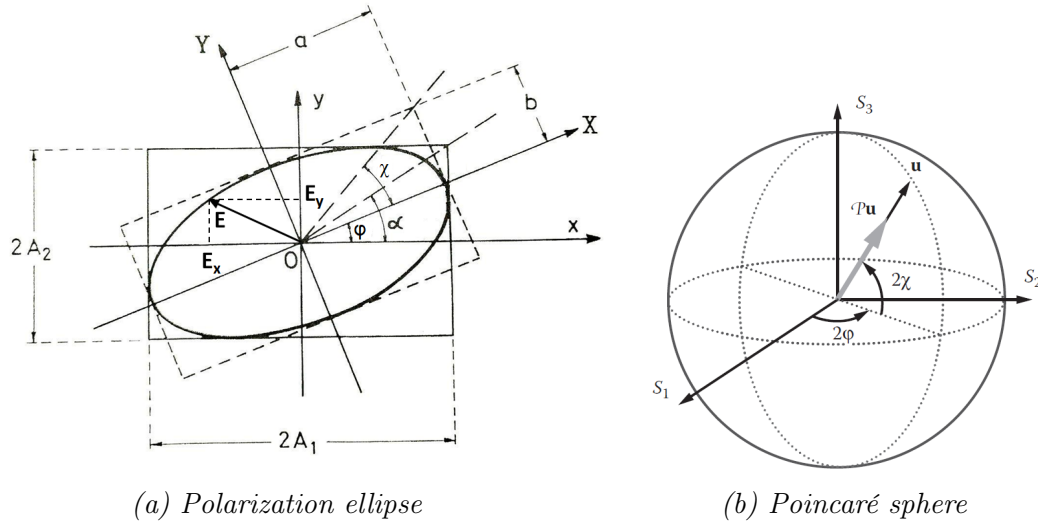


Figure 3.2 - Two different ways of representing the polarization of light.  
a) Polarization ellipse, modified from [1] and b) Poincaré sphere, taken from [1].

Another way of representing polarization is by means of the Poincaré sphere [1] (shown in Figure 3.2b). In this representation different values along the axis  $S_1$ ,  $S_2$  and  $S_3$  will define a certain polarization (linear, circular...) and a polarization state will be represented by the unitary polarization vector  $\mathbf{u}$ :

$$\mathbf{u} = \begin{bmatrix} u_1 \\ u_2 \\ u_3 \end{bmatrix} = \begin{bmatrix} \cos(2\varphi) \cos(2\chi) \\ \sin(2\varphi) \cos(2\chi) \\ \sin(2\chi) \end{bmatrix} \quad (3.6)$$

In this representation, points on the surface of the sphere ( $\mathcal{P} = 1$ ) are totally polarized states and points inside the sphere ( $\mathcal{P} < 1$ ) represent partially polarized states, being  $\mathcal{P}$  defined as the degree of polarization ( $0 < \mathcal{P} < 1$ ).

## 3.2 Stokes vector and Mueller matrix formalism

One way of describing polarized light is by means of the Jones parameters. Coming back to Equations 3.2, the components of the field  $\mathbf{E}$  can be expressed in its general form:

$$E_x = A_1 \exp(i\omega t - ikz) \quad (3.7)$$

$$E_y = A_2 \exp(i\omega t - ikz + \delta) \quad (3.8)$$

or:

$$E_x = A_1 \exp[i(\omega t - kz)] \quad (3.9)$$

$$E_y = A_2 \exp(i\delta) \exp[i(\omega t - kz)] \quad (3.10)$$

With these parameters the Jones vector  $\mathbf{J}$  is constructed:

$$\mathbf{J} = \begin{bmatrix} E_x \\ E_y \end{bmatrix} = \begin{bmatrix} A_1 \\ A_2 e^{i\delta} \end{bmatrix} \quad (3.11)$$

The effect of a non-depolarizing system element over the polarization state of a light beam will be represented by a 2x2 matrix, called the Jones matrix  $\mathbf{T}$ , which relates the input and output Jones vector of a system:

$$\mathbf{J}' = \mathbf{T}\mathbf{J} \quad (3.12)$$

$$\mathbf{J}' = \begin{bmatrix} j_{11} & j_{12} \\ j_{21} & j_{22} \end{bmatrix} \mathbf{J} \quad (3.13)$$

where  $j_{ij}$  are the elements of the Jones matrix.

However, this representation is only valid for totally polarized states of light. In order to represent all the possibilities we need a more complex and extended formalism: the Mueller matrix formalism.

A more general way to represent polarized light is by means of the Stokes parameters (Equations 3.14 - 3.17). While Jones vector can be only employed for totally polarized light, Stokes vector can represent every partially polarized state, from totally polarized to completely unpolarized.

$$s_1' = A_1^2 + A_2^2 \quad (3.14)$$

$$s_2' = A_1^2 - A_2^2 \quad (3.15)$$

$$s_3' = 2A_1A_2 \cos \delta \quad (3.16)$$

$$s_4' = 2A_1A_2 \sin \delta \quad (3.17)$$

The four parameters are related by:

$$s_1' = \sqrt{s_2'^2 + s_3'^2 + s_4'^2} \quad (3.18)$$

Parameter  $s_1'$  represents the intensity so the rest can be normalized to it. In this way, the four parameters conform the Stokes vector  $\mathbf{S}$  which fully characterizes a polarized light beam:

$$\mathbf{S} = \begin{bmatrix} s_1 \\ s_2 \\ s_3 \\ s_4 \end{bmatrix} = \begin{bmatrix} 1 \\ (A_1^2 - A_2^2)/s_1' \\ 2A_1A_2 \cos \delta / s_1' \\ 2A_1A_2 \sin \delta / s_1' \end{bmatrix} \quad (3.19)$$

Parameters  $s_2'$  and  $s_3'$  represent the balance between horizontal and vertical polarization and between  $+45^\circ$  and  $-45^\circ$  respectively while parameter  $s_4'$  is related to right handed or left handed circular polarization.

Stokes vector can also be expressed as a function of the ellipticity angle  $\chi$  and azimuth  $\varphi$  or as a function of  $\alpha$  and the phase shift  $\delta$ :

$$\mathbf{S} = \begin{bmatrix} 1 \\ \cos(2\varphi) \cos(2\chi) \\ \sin(2\varphi) \cos(2\chi) \\ \sin(2\chi) \end{bmatrix} = \begin{bmatrix} 1 \\ \cos(2\alpha) \\ \sin(2\alpha) \cos(\delta) \\ \sin(2\alpha) \sin(\delta) \end{bmatrix} \quad (3.20)$$

With Equation 3.6, the Stokes vector can also be written as:

$$\mathbf{S} = I \begin{bmatrix} 1 \\ \mathcal{P}\mathbf{u} \end{bmatrix} = I \begin{bmatrix} 1 \\ \mathbf{p} \end{bmatrix} \quad (3.21)$$

where  $\mathcal{P}$  is the degree of polarization and  $\mathbf{p}$  is the polarization vector.

$$\mathcal{P} = \sqrt{s_2^2 + s_3^2 + s_4^2} \quad (3.22)$$

In a similar way to the Jones vector description, the output and input Stokes vectors are related by the equation  $\mathbf{S}' = \mathbf{M}\mathbf{S}$ , where  $\mathbf{M}$  is the 4x4 Mueller matrix [6]:

$$\mathbf{M} = \begin{bmatrix} m_{11} & m_{12} & m_{13} & m_{14} \\ m_{21} & m_{22} & m_{23} & m_{24} \\ m_{31} & m_{32} & m_{33} & m_{34} \\ m_{41} & m_{42} & m_{43} & m_{44} \end{bmatrix} \quad (3.23)$$

where  $m_{ij}$  are the Mueller matrix elements that are given by [56]:

$$\begin{aligned}
m_{11} &= 1/2(j_{11}^2 + j_{22}^2 + j_{21}^2 + j_{12}^2) & m_{31} &= \text{Re}(j_{21}j_{11}^* + j_{22}j_{12}^*) \\
m_{12} &= 1/2(j_{11}^2 - j_{22}^2 + j_{21}^2 - j_{12}^2) & m_{32} &= \text{Re}(j_{21}j_{11}^* - j_{22}j_{12}^*) \\
m_{13} &= \text{Re}(j_{12}j_{11}^* + j_{22}j_{21}^*) & m_{33} &= \text{Re}(j_{22}j_{11}^* + j_{21}j_{12}^*) \\
m_{14} &= -\text{Im}(j_{12}j_{11}^* + j_{22}j_{21}^*) & m_{34} &= \text{Im}(-j_{22}j_{11}^* + j_{21}j_{12}^*) \\
m_{21} &= 1/2(j_{11}^2 - j_{22}^2 - j_{21}^2 + j_{12}^2) & m_{41} &= \text{Im}(j_{21}j_{11}^* + j_{22}j_{12}^*) \\
m_{22} &= 1/2(j_{11}^2 + j_{22}^2 - j_{21}^2 - j_{12}^2) & m_{42} &= \text{Im}(j_{21}j_{11}^* - j_{22}j_{12}^*) \\
m_{23} &= \text{Re}(j_{12}j_{11}^* - j_{22}j_{21}^*) & m_{43} &= \text{Im}(j_{22}j_{11}^* + j_{21}j_{12}^*) \\
m_{24} &= \text{Im}(-j_{12}j_{11}^* + j_{22}j_{21}^*) & m_{44} &= \text{Re}(j_{22}j_{11}^* - j_{21}j_{12}^*)
\end{aligned} \tag{3.24}$$

The Mueller matrix [1] is a 4x4 matrix,  $\mathbf{M}$ , whose 16 elements fully characterize the optical response of a given medium under some given illumination and observation geometry, for a certain wavelength ( $\lambda$ ) and for a certain region of the system on which the information is averaged. Element  $m_{11}$ , represents the total intensity (in polarimetric imaging it would be similar to the conventional optical image observed under the microscope) and it is customary to normalize all fifteen elements to the value of  $m_{11}$ , as we will do in each matrix presented in this dissertation.

### 3.3 Polarimetric properties of any system

Although the Mueller matrix is sensitive to small changes in the conditions of the system, its physical interpretation is not a straightforward task. For this reason it is very common to mathematically decompose it introducing some physical parameters.

The Mueller matrix of any physical system can be expressed in a compacted or block form in the way [28]:

$$\mathbf{M} = \begin{bmatrix} 1 & \mathbf{D}^T \\ \mathbf{P} & \mathbf{m}_{3 \times 3} \end{bmatrix} \tag{3.25}$$

where  $\mathbf{P}$  and  $\mathbf{D}$  are the polarizance and diattenuation vector respectively and  $m_{3 \times 3}$  is the remaining  $3 \times 3$  matrix. For homogeneous systems, the diattenuation and polarizance vectors are equal ( $\mathbf{P} = \mathbf{D}$ ).

The polarizance vector is responsible for the emerging polarization state after a depolarized beam enters the system. It is defined from the elements of the first column of the Mueller matrix as:

$$\mathbf{P} = \begin{bmatrix} m_{21} \\ m_{31} \\ m_{41} \end{bmatrix} \tag{3.26}$$

From this, polarizance  $P$ , can be defined as the property of a medium that increases the degree of polarization:

$$P = \sqrt{m_{21}^2 + m_{31}^2 + m_{41}^2} \quad (3.27)$$

The polarimetric response of any given system can be summarized in three fundamentals properties [56]: diattenuation, retardance and depolarization. Next, we provide a description of each one of these properties together with a representation of the corresponding Mueller matrix. Table 3.1 presents the Mueller matrix of some particular interesting optical systems.

### 3.3.1 Diattenuation

Diattenuation,  $D$ , is the property whereby the output intensity depends on the polarization of the incident light. Diattenuation is defined as follows:

$$D = \frac{I_{max} - I_{min}}{I_{max} + I_{min}} \quad (3.28)$$

where  $I_{max}$  and  $I_{min}$  are the maximum and minimum output intensities observed for two orthogonal incident polarizations of the input beam.

Diattenuation is the intrinsic property of diattenuators or polarizers, a medium that display anisotropic intensity attenuation, that is, the transmittance of the medium depends on the input state of polarization. For an ideal polarizer  $D = 1$ . A diattenuation vector  $\mathbf{D}$  [28] can be described, whose components are the elements of the first row of the Mueller matrix:

$$\mathbf{D} = \begin{bmatrix} m_{12} \\ m_{13} \\ m_{14} \end{bmatrix} \begin{bmatrix} D_H \\ D_{45^\circ} \\ D_C \end{bmatrix} \quad (3.29)$$

where  $D_H$ ,  $D_{45^\circ}$  and  $D_C$  give, respectively, the horizontal,  $45^\circ$  linear and circular diattenuation (depending on the orthogonal axes of our choice).

The linear diattenuation is defined as:

$$D_L = \sqrt{D_H^2 + D_{45}^2} \quad (3.30)$$

While the total diattenuation can be expressed also as:

$$D = \sqrt{D_H^2 + D_{45}^2 + D_C^2} \quad (3.31)$$

### 3.3.2 Retardance

Retardance,  $R$ , is the phase difference introduced between two orthogonal incident polarizations. It is the property characteristic of retarders, an element designed to

introduce a specific phase difference between the exiting beams for two orthogonal incident polarization states. An ideal retarder has  $D = 0$  (constant transmittance independent of the incident polarization) and  $R = 1$ .

The retardance can be defined from the matrix  $\mathbf{M}_R$  of a retarder:

$$R = \cos^{-1} \left( \frac{\text{Tr}(\mathbf{M}_R)}{2} - 1 \right) \quad (3.32)$$

where  $\text{Tr}$  means the trace.

Similar to the diattenuation, a retardance vector is defined as:

$$\mathbf{R} = \begin{bmatrix} R_H \\ R_{45^\circ} \\ R_C \end{bmatrix} \quad (3.33)$$

where  $R_H$ ,  $R_{45^\circ}$  and  $R_C$  are, respectively, the horizontal,  $45^\circ$  and circular retardation.

From this vector, the linear retardance can be calculated as:

$$R_L = \sqrt{R_H^2 + R_{45}^2} \quad (3.34)$$

While the retardance can be expressed also as:

$$R = \sqrt{R_H^2 + R_{45}^2 + R_C^2} \quad (3.35)$$

### 3.3.3 Depolarization

Depolarization,  $\Delta$ , is the property whereby the degree of polarization of an emerging light beam is reduced with respect to the incident beam. The Mueller matrix of a pure depolarizer with zero diattenuation and zero retardance is:

$$\mathbf{M} = \begin{bmatrix} 1 & \mathbf{0}^T \\ \mathbf{0} & \mathbf{m}_\delta \end{bmatrix} = \begin{bmatrix} 1 & 0 & 0 & 0 \\ 0 & a & 0 & 0 \\ 0 & 0 & b & 0 \\ 0 & 0 & 0 & c \end{bmatrix} \quad (3.36)$$

where  $\mathbf{m}_\delta$  is a  $3 \times 3$  matrix. The depolarization  $\Delta$  is given by:

$$\Delta = 1 - \frac{1}{3}(|a| + |b| + |c|) \quad (3.37)$$

where  $a$ ,  $b$  and  $c$  are real numbers ( $-1 \leq a, b, c \leq 1$ ) and  $0 \leq \Delta \leq 1$ .

Based on whether the medium has depolarization or not, Mueller matrices can be described as depolarizing or non-depolarizing. A Mueller matrix  $\mathbf{M}$  is non-depolarizing, or pure, if it does not depolarize light entering a medium, maintaining

the degree of polarization. On the other hand, a depolarizing  $\mathbf{M}$  transforms totally polarized light in partially polarized. The depolarization index,  $D_I$ , (Equation 3.38) [57] is a way to quantify how much a  $\mathbf{M}$  depolarizes an incident polarized beam. Pure matrices have  $D_I = 0$  while fully depolarizing ones present  $D_I = 1$ .

$$D_I = 1 - \sqrt{\frac{\text{Tr}(\mathbf{M}^T \mathbf{M}) - m_{11}^2}{3m_{11}^2}} \quad (3.38)$$

where superindex  $T$  is the transpose.

The concept of purity  $Pu$  is introduced to identify if a Mueller matrix introduces or not depolarization: [58]

$$Pu = \sqrt{\frac{\text{Tr}(\mathbf{M}^T \mathbf{M}) - m_{11}^2}{3m_{11}^2}} \quad (3.39)$$

with  $0 \leq Pu \leq 1$ . A non-depolarizing Mueller matrix will have  $Pu = 1$  (pure matrix) while a system that fully depolarizes an incident polarized beam will have a Mueller matrix with  $Pu = 0$ . The intermediate cases correspond to systems that introduce a partial depolarization in the light.

### 3.4 Mueller matrix analysis and decomposition

The raw polarimetric data, given by the Mueller matrix  $\mathbf{M}$ , contains the optical information of the system, i.e., its polarimetric response, for the actual configuration of the experiment. However, quite often the elements of  $\mathbf{M}$  are not directly connected with the physical parameters of interest. Then, it is convenient to introduce a step in which physically interpretable parameters are defined. This is commonly done through matrix transformation operations. In other words, by means of a proper decomposition or transformation, the optical properties of each part of the system can be described in terms of parameters that may have a physical interpretation.

We have to take into account that not every experimental Mueller matrix is physically realizable, this is, represents a real system. An obvious necessary condition is that any acceptable Stokes vector must be transformed by  $\mathbf{M}$  into another acceptable Stokes vector. This is, its degree of polarization (3.22) must be between 0 and 1. However, this condition is not sufficient. A necessary and sufficient condition for a Mueller matrix to represent a real system is the so called Coherence condition or Cloude's criterion [59]. This condition establishes that the matrix  $\mathbf{N}$ , called the coherence matrix, given by Equation 3.40, is an Hermitian positive definite matrix (all eigenvalues are non-negative, and at least one is strictly positive).

$$\mathbf{N} = \begin{bmatrix} m_{11} + m_{22}+ & m_{13} + m_{23}+ & m_{31} + m_{32}- & m_{33} + m_{44}+ \\ m_{12} + m_{21} & i(m_{14} + m_{24}) & i(m_{41} + m_{42}) & i(m_{34} - m_{43}) \\ m_{13} + m_{23}- & m_{11} - m_{22}- & m_{33} - m_{44}- & m_{31} - m_{32}- \\ i(m_{14} + m_{24}) & m_{12} + m_{21} & i(m_{34} + m_{43}) & i(m_{41} - m_{42}) \\ m_{31} + m_{32}+ & m_{33} - m_{44}+ & m_{11} - m_{22}+ & m_{13} - m_{23}+ \\ i(m_{41} + m_{42}) & i(m_{34} + m_{43}) & m_{12} - m_{21} & i(m_{14} - m_{24}) \\ m_{33} + m_{44}- & m_{31} - m_{32}+ & m_{13} - m_{23}- & m_{11} + m_{22}- \\ i(m_{34} - m_{43}) & i(m_{41} - m_{42}) & i(m_{14} - m_{24}) & m_{12} - m_{21} \end{bmatrix} \quad (3.40)$$

Another widely used, though more permissive, condition for a matrix to be considered a valid Mueller matrix of an optical system is [60]:

$$\text{Tr}(\mathbf{M}^T \mathbf{M}) \leq 4m_{11} \quad (3.41)$$

When some of these conditions are not satisfied, the matrix is said to be not physically realizable or non-physical. Sometimes, an experimentally measured Mueller matrix may not satisfy these conditions and, therefore result as non-physical due to experimental errors. In this case, it would be necessary to filter [59] the matrix in order to eliminate these errors and to make it physical.

Once the realizability of the matrix is assured, there are a set of different decompositions that can be applied to the Mueller matrix in order to phenomenologically interpret it. Basically, these decomposition methods can be classified mainly into two groups [56]:

- ▷ *Sum decompositions*: such as Cloude Decomposition [61] and Le Roy-Bréhonnet Decomposition [62]. These decompositions expand a depolarizing Mueller matrix in an incoherent addition of non-depolarizing matrices and are usually used to assess its physical realizability.
- ▷ *Product decomposition*: such as the Polar Decomposition [28] (Forward and Reverse Decompositions), the Symmetric Decomposition [63, 64] and the Logarithmic (or Differential) Decomposition [65, 30]. These decompositions describe the sample as a stack of elementary samples traversed sequentially by the light beam and are mostly used to evaluate the diattenuation, retardation, depolarization and polarizance of a Muller matrix.

In this work we have focused in three of the most common use: Mueller Matrix Polar Decomposition, Mueller Matrix Differential Decomposition and Mueller Matrix Transformation, that will be described in what follows.

## Mueller Matrix Polar Decomposition (MMPD)

In its forward or reverse decomposition, this method is one of the most widely used to interpret the polarimetric properties of a sample [9, 66–68].

Polar decomposition [28] is supported by the fact that a system represented by a matrix  $\mathbf{V}$  can be decomposed as  $\mathbf{V} = \mathbf{UH}$  where  $\mathbf{U}$  is a unitary matrix and  $\mathbf{H}$  is an hermitian matrix. The unitary matrix will not affect the degree of polarization of

the system while the hermitian matrix may present diattenuation so that they can be related to different optical elements. In this way the Mueller matrix of a system with no depolarization can be decomposed as the product of two, in the form:

$$\mathbf{M} = \mathbf{M}_R \mathbf{M}_D \quad (3.42)$$

where  $\mathbf{M}_D$  is the diattenuation matrix,  $\mathbf{M}_R$  is the retardation matrix.

In the case of having a system that presents depolarization, it is necessary to include the action of another matrix,  $\mathbf{M}_\Delta$  that will account for this effect. In a general case, the Mueller matrix can be expressed as the product of three matrices representing independent physical actions of the system on the polarimetric properties of the scattered light.

$$\mathbf{M} = \mathbf{M}_\Delta \mathbf{M}_R \mathbf{M}_D \quad (3.43)$$

This decomposition represents the action of each one of the properties, the light passing through each one of them, in the inverse order displayed by the equation. In total, there are 6 possible combinations of the three matrices that represent different order of performance of each element. Equation 3.43 is the most common forward decomposition. Equally, a reverse decomposition is possible:

$$\mathbf{M} = \mathbf{M}_D \mathbf{M}_R \mathbf{M}_\Delta \quad (3.44)$$

This decomposition allows to separate the response of the system in the basic polarimetric properties addressed in Section 3.3. Now, from the elements of these three matrices it is possible to calculate the different parameters, given by the following equations [69, 70]:

▷ Total diattenuation:

$$D_T = \frac{\sqrt{(m_{D12})^2 + (m_{D13})^2 + (m_{D14})^2}}{m_{D11}} \quad (3.45)$$

▷ Linear diattenuation:

$$D_L = \frac{\sqrt{(m_{D12})^2 + (m_{D13})^2}}{m_{D11}} \quad (3.46)$$

▷ Depolarization coefficient:

$$\Delta = 1 - \frac{|tr(\mathbf{M}_\Delta - 1)|}{3} \quad (3.47)$$

▷ Linear retardance:

$$\delta = \arccos(\sqrt{(m_{R22} + m_{R33})^2 + (m_{R32} - m_{R23})^2} - 1) \quad (3.48)$$

▷ Optical rotation (optical activity):

$$\psi = \arctan \left( \frac{m_{R32} - m_{R23}}{m_{R22} + m_{R33}} \right) \quad (3.49)$$

### Mueller Matrix Differential Decomposition (MMDD)

We describe here the logarithmic decomposition, based on the differential formulation according to which, the Stokes vector is given by [65]:

$$dS/dz = \mathbf{m}'S \quad (3.50)$$

where  $\mathbf{m}'$  is the 4x4 differential Mueller matrix and  $z$  is the distance travelled along the direction of propagation in the medium in which the polarization is susceptible to change.

The differential decomposition of the Mueller matrix is obtained from the matrix logarithm of the macroscopic Mueller matrix:

$$\mathbf{m}' = \ln(\mathbf{M}) \quad (3.51)$$

The matrix  $\mathbf{m}'$  can be expressed as the sum of two matrices, one containing the non depolarizing effects and another one that is just depolarizing:  $\mathbf{m}_m$  and  $\mathbf{m}_u$  respectively. These two matrices are given by the equations:

$$\mathbf{m}_m = 1/2(\mathbf{m}' - \mathbf{G}\mathbf{m}'^T\mathbf{G}) \quad (3.52)$$

$$\mathbf{m}_u = 1/2(\mathbf{m}' + \mathbf{G}\mathbf{m}'^T\mathbf{G}) \quad (3.53)$$

where  $\mathbf{G}$  is the diagonal matrix  $\mathbf{G} = \text{diag}(1, -1, -1, -1)$  and  $T$  means transpose.

The most general form of the differential Mueller matrix for a non-depolarizing medium ( $\mathbf{m}_u = 0$ ) is [71]:

$$\mathbf{m}' = \mathbf{m}_m + \mathbf{m}_u = \begin{bmatrix} \alpha & LD & LD' & CD \\ LD & \alpha & CB & -LB' \\ LD' & -CB & \alpha & LB \\ CD & LB' & -LB & \alpha \end{bmatrix} \quad (3.54)$$

where  $LD$ ,  $LD'$  and  $CD$  are linear dichroism in the xy axes, linear dichroism, in the 45-145° and circular dichroism.  $LB$ ,  $LB'$  and  $CB$  stand for linear birefringence in the xy and 45-135° axes and circular birefringence, respectively. The value  $\alpha$  is the absorption coefficient.

From this decomposition, total diattenuation and total birefringence are calculated as follows:

$$TD = \sqrt{LD^2 + LD'^2 + CD^2} \quad (3.55)$$

$$TB = \sqrt{LB^2 + LB'^2 + CB^2} \quad (3.56)$$

In the same way, total linear diattenuation and birefringence are calculated with the expressions:

$$TLD = \sqrt{LD^2 + LD'^2} \quad (3.57)$$

$$TLB = \sqrt{LB^2 + LB'^2} \quad (3.58)$$

### Mueller Matrix Transformation (MMT)

Despite not having been mentioned in the previous classification, there is another method proposed by Honghui He et al. [29, 72] for quantitatively characterize the properties of anisotropic scattering media. This method allows to obtain a new set of transformation parameters by fitting the Mueller matrix elements to trigonometric curves in polar coordinates. These parameters, which can be expressed as analytical functions of 16 Mueller matrix elements, are related to anisotropy degree ( $A$ ), depolarization power ( $b$ ) associated to structure, size or density of the scatters, and alignment direction of the sample ( $x$ ). Moreover, the amplitude parameters ( $t_1$ ,  $t_2$  and  $t_3$ ) would show how the medium respond to different incident polarizations.

$$A = \frac{2bt_1}{b^2 + t_1^2} \quad (3.59)$$

$$t_1 = \frac{\sqrt{(m_{22} - m_{33})^2 + (m_{23} + m_{32})^2}}{2} \quad (3.60)$$

$$t_2 = \sqrt{m_{21}^2 + m_{31}^2} \quad (3.61)$$

$$t_3 = \sqrt{m_{42}^2 + m_{43}^2} \quad (3.62)$$

$$b = \frac{m_{22} + m_{33}}{2} \quad (3.63)$$

$$x = \tan\left(\frac{m_{23} + m_{32}}{m_{22} - m_{33}}\right) \quad (3.64)$$

This set of parameters seem to be of special interest in biological research [73, 74]. Moreover, one of the main advantages of this method is that calculation of MMT parameters is faster and more straightforward than, for example, those from MMPD and it has been found that they provide similar information about a sample:  $b$  and  $\Delta$  are both related to the depolarization property,  $A$  is sensitive to retardance and diattenuation and  $t_3$  is an indicator of birefringence.

ELEMENT	MUELLER MATRIX
Vacuum	$\begin{bmatrix} 1 & 0 & 0 & 0 \\ 0 & 1 & 0 & 0 \\ 0 & 0 & 1 & 0 \\ 0 & 0 & 0 & 1 \end{bmatrix}$
Linear polarizer (H/V)	$\begin{bmatrix} 1 & 1 & 0 & 0 \\ 1 & 1 & 0 & 0 \\ 0 & 0 & 0 & 0 \\ 0 & 0 & 0 & 0 \end{bmatrix} / \begin{bmatrix} 1 & -1 & 0 & 0 \\ -1 & 1 & 0 & 0 \\ 0 & 0 & 0 & 0 \\ 0 & 0 & 0 & 0 \end{bmatrix}$
Linear polarizer ( $45^\circ / -45^\circ$ )	$\begin{bmatrix} 1 & 0 & 1 & 0 \\ 0 & 0 & 0 & 0 \\ 1 & 0 & 1 & 0 \\ 0 & 0 & 0 & 0 \end{bmatrix} / \begin{bmatrix} 1 & 0 & -1 & 0 \\ 0 & 0 & 0 & 0 \\ -1 & 0 & 1 & 0 \\ 0 & 0 & 0 & 0 \end{bmatrix}$
General diattenuator (azimuth $\alpha$ )	$\begin{bmatrix} 1 & \cos(2\alpha) & \sin(2\alpha) & 0 \\ \cos(2\alpha) & \cos^2(2\alpha) & \sin(2\alpha)\cos(2\alpha) & 0 \\ \sin(2\alpha) & \sin(2\alpha)\cos(2\alpha) & \sin^2(2\alpha) & 0 \\ 0 & 0 & 0 & 0 \end{bmatrix}$
Quarter-wave plate (H/V)	$\begin{bmatrix} 1 & 0 & 1 & 0 \\ 0 & 1 & 0 & 0 \\ 0 & 0 & 0 & 1 \\ 0 & 0 & -1 & 0 \end{bmatrix} / \begin{bmatrix} 1 & 0 & 0 & 0 \\ 0 & 1 & 0 & 0 \\ 0 & 0 & 0 & -1 \\ 0 & 0 & 1 & 0 \end{bmatrix}$
Mirror (also half-wave plate)	$\begin{bmatrix} 1 & 0 & 0 & 0 \\ 0 & 1 & 0 & 0 \\ 0 & 0 & -1 & 0 \\ 0 & 0 & 0 & -1 \end{bmatrix}$
General retarder (retardance $\delta$ )	$\begin{bmatrix} 1 & 0 & 0 & 0 \\ 0 & 1 & 0 & 0 \\ 0 & 0 & \cos(\delta) & \sin(\delta) \\ 0 & 0 & -\sin(\delta) & \cos(\delta) \end{bmatrix}$
Pure depolarizer	$\begin{bmatrix} 1 & 0 & 0 & 0 \\ 0 & a & 0 & 0 \\ 0 & 0 & b & 0 \\ 0 & 0 & 0 & c \end{bmatrix}$

Table 3.1 - Mueller matrix of common optical systems.  $\alpha$  is the azimuth of a diattenuator and  $\delta$  is the retardance of a retarder.

# Chapter 4

## Fundamentals of cell biology and their optical response

Throughout this brief chapter we will give a global vision about the most remarkable characteristics of cells, its structure, the cell cycle and the main functions that can be of interest for understanding this thesis [75].

### 4.1 Introduction to cells

Cells are the basic morphological and functional unit of all living organisms. It is the minimum unit of life. Cells are divided into two large groups based on their structure: prokaryotic and eukaryotic cells.

- ▷ Prokaryotic cells are organisms without a nucleus or structures defined by membranes. They are surrounded by a cellular wall which provides protection from the outside.
- ▷ Eukaryotic cells, those that form animals, plants and fungi, are more complex. They possess a nucleus isolated from the cytoplasm by a nuclear membrane and have a compartmentalized cytoplasm with membrane-bounded specialized organelles that serve different functions.

#### 4.1.1 Cell structure

Here, we focus on the structure of an eukaryotic cell, which is the type of cell we are going to work with. Figure 4.1 shows the internal components of a typical eukaryotic cell. Then, some of the main parts are described in what follows:

- ▷ **Nucleus:** the nucleus is where the genetic information (DNA) is stored, more precisely, in the chromosomes. The largest structure inside the nucleus is the nucleolus, where the ribosomes are assembled. The nucleus is separated from the cytoplasm by a double membrane with nuclear pores that allows the exchange of RNA and proteins with the cytoplasm.
- ▷ **Ribosomes:** responsible for protein synthesis.

- ▷ **Lysosomes:** they are in charge of cellular digestion.
- ▷ **Endoplasmic reticulum:** is a complex system of membranes distributed all over the cytoplasm and arranged in the form of flattened sacs and tubules that conform different domains (rough endoplasmic reticulum and smooth endoplasmic reticulum). It participates in processes like transport of synthesized proteins, intracellular transport and lipid metabolism.
- ▷ **Golgi apparatus:** process the sugar side of some proteins and sort them to send it to other parts of the cell.
- ▷ **Plasma membrane:** it is a lipid bilayer that surrounds cells and provides protection from the exterior. It is hydrophobic in its interior. The plasma membrane is the interface of the cell with its environment and it has channels, carriers and pumps which provide the cell with nutrients and ions.
- ▷ **Mitochondria:** basically, they are an energy factory. They provide the energy necessary for cellular activity by converting most of the energy released from the breakdown of nutrients into the synthesis of ATP (adenosine triphosphate), the basic currency for most energy requiring reactions in cells.
- ▷ **Peroxisomes:** Peroxisomes are membrane-bound organelles containing enzymes that participate in oxidative reactions of fatty acids to produce energy.
- ▷ **Cytoskeleton and Motility Apparatus:** it is a complex network of three proteins whose function is to maintain the shape of the cell and organize the internal structure and intervene in processes such as transport of organelles through the cytoplasm, traffic and cellular division. It is a dynamic structure which can contract and deform, allowing cell movements and locomotion, migration, and mitosis.

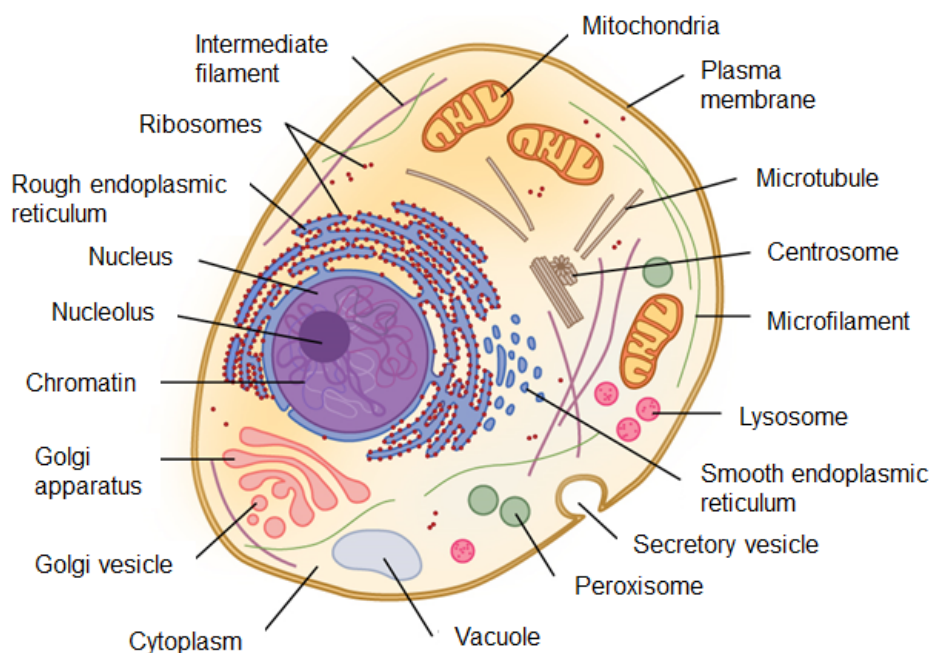


Figure 4.1 - Eukaryotic cell components<sup>1</sup>.

This description serves us to make a better idea that, although a cell is mainly water, it has a very complex structure that allows it to do all the processes that are necessary to survive and reproduce if the medium conditions are adequate.

### 4.1.2 The cell cycle

The cell cycle, Figure 4.2, is a series of events where cells duplicate their DNA and divide into two identical daughters. The cycle consists of four stages that take, in cultured cells, approximately 22 hours: in the  $G_1$  phase, the cell grows in size, during the  $S$  phase, the cell duplicates the DNA. During the  $G_2$  phase, the cell prepares for replication and finally, in the  $M$  phase or mitosis, the cell duplicates.  $G_1$ ,  $G_2$  and  $S$  phases can all be englobed in the interphase or resting stage, where the cell is apparently not "active".

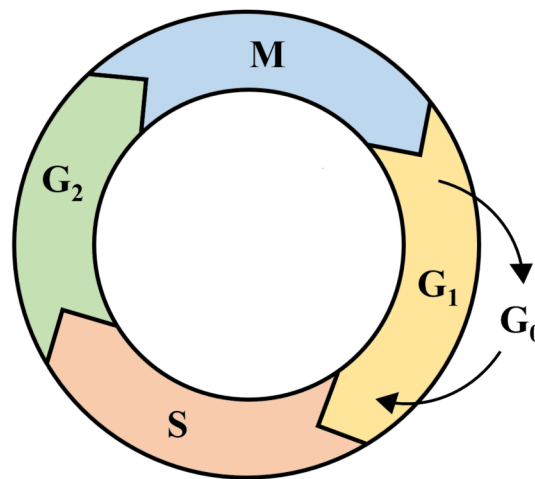


Figure 4.2 - Diagram of the cell cycle

The cell cycle integrates a continuous growth cycle that involves the increase in cell mass, combined with a discontinuous division or chromosome cycle in which the genome is replicated and partitioned creating two daughter cells. The chromosome cycle is driven by a sequence of enzymatic cascades that produce a sequence of discrete biochemical states of the cytoplasm.

Next, each phase is explained in more detail.

1.  **$G_1$  phase** (first gap): This can be considered the initial point of the cell cycle and it begins after mitosis. Since after mitosis cells reduce their size to one half, the cell has to grow to its optimal size during this stage. At this point, a cell can "decide" to complete the cycle in order to divide again or to exit the cycle (differentiate) and to remain in a non-dividing or pause stage either temporarily or permanently ( $G_0$  phase).

---

<sup>1</sup>Image from <https://cnx.org/contents/FPtK1z mh@8.25:fEI3C8Ot@10/Preface> under the Creative Commons Attribution 4.0 International license.

2. **G<sub>0</sub> phase**: when a cell is at this phase, it means that it left the cell cycle. Most cells of multicellular organisms differentiate to achieve specialized functions and do not re-enter the cycle never again. However, this does not mean that this is always a permanent stage. For example, if the medium conditions are not favourable (lack of nutrients) cells will enter this pause stage and, when the conditions change, re-enter the cycle and divide again.
3. **S phase** (synthetic): during this phase, the cell duplicates its DNA in order to have enough material to produce two daughter cells.
4. **G<sub>2</sub> phase** (second gap): at this point the DNA replication is completed and the cell checks for unreplicated or damaged DNA. If this happens, a triggered mechanism delays the entry of the cell into mitosis.
5. **M phase** (mitotic): during mitosis a parent cell divides into two daughters cells. Chromosomes and cytoplasm split in two. Mitosis is divided into six phases:
  - *prophase*: the chromosomes condense inside the nucleus. The duplicated centrosomes separate and form the two poles of the mitotic spindle. The nucleolus disappears.
  - *prometaphase*: the nuclear envelope breaks and chromosomes start to attach randomly to microtubules emanating from the two poles of the forming mitotic spindle.
  - *metaphase*: all the chromosomes are attached.
  - *anaphase*: the sister chromatids separate and move towards the two spindle poles.
  - *telophase*: the cell is almost divided. The mitotic spindle breaks down, two nucleus with its membrane are formed and the chromosomes begin to uncondense. Finally a contractile ring that constricts the cell around the center assembles.
  - *cytokinesis*: it is the final part of the mitosis phase, where the two daughter cells separate from one another.

Cells exhibit an extraordinary diversity in their patterns of growth, proliferation, and death. Cells possess some biochemical circuits (called checkpoints) that regulate the cell cycle depending on the physiological conditions of the cell and the environment, detecting if there has been some problem or damage of the DNA during replication. Perturbation on the cell cycle can lead to diseases such as cancer, where an uncontrolled growth of cells produce tumors.

### 4.1.3 Cellular adhesion and cellular motility

#### Cell culture

Cell culture<sup>2</sup> is the process by which cells grow under controlled conditions. First, the cells are isolated from a living organism and placed in a liquid medium that provides the necessary nutrients and conditions for the cells to grow. These conditions vary depending on the type of cell but typically, cells are cultured in an artificial environment containing:

- ▷ A carbonate-buffered culture medium that supplies the essential nutrients,
- ▷ Growth factors (proteins or hormones that stimulate cellular growth),
- ▷ Gases (5 % CO<sub>2</sub>),
- ▷ And controlled conditions of pH, osmotic pressure, relative humidity (95%) and temperature (37 °C).

Moreover, some cells are adherent and need a solid substrate to attach to in order to grow while others do not attach and grow in suspension.

While they are under these controlled conditions, cells undergo the cell cycle and divide increasing the population. After growing, cells are diluted and transferred to another flask with fresh medium so they can continue proliferating. Normal cells usually divide only a limited number of times before losing their ability to proliferate (senescence). However, tumor cells, due to mutations in genes controlling proliferation, may keep undergoing unlimited divisions (cell line). This process will produce continuous cell lines which are very important for research in cellular and molecular biology.

Cells cultures can be classified in three main categories based on their appearance: fibroblast-like (they grow adhered to a substrate and have elongated shapes), epithelial (they are adherent also and their shape is polygonal, growing in discrete patches) and leukocyte-like (they grow in suspension and have a spherical shape).

Cell culture is the way we have to produce a certain kind of cells under controlled conditions in order to use it for researching purposes. The major advantage of using cell cultures is the consistency and reproducibility of results.

#### Cellular adhesion

It has been mentioned, some cells are adherent, meaning that they need to attach to a surface in order to grow. Besides that, all cells interact with molecules in their environment, in many cases relying on cell surface adhesion proteins to bind these molecules. Multicellular organisms are particularly dependent on adhesion of cells to each other and the extracellular matrix (ECM). During development, carefully regulated genetic programs specify cell-cell and cell-matrix interactions that

---

<sup>2</sup><https://www.thermofisher.com/es/es/home/references/gibco-cell-culture-basics/introduction-to-cell-culture.html>

determine the architecture of each tissue and organ.

Cell adhesion [27] attracts a lot of research interest for being essential in cell communication and regulation, but also for other more specific aspects, like the different adhesion properties of normal and cancer cells [76]. Optically, adhesion of a cell affects the surface shape and therefore the way in which it transmits and scatters light. The shape of a cell can be approximated to that of an spheroid that can vary between some extreme cases, depending on the cell condition and cell-surface interaction. However, the actual state of the partially adhered cell is not easy to identify. Cell adhesion is a biological process that includes cell-cell and cell-substrate interactions which enable cells to stay within a tissue or migrate out of it. In cancer, this is exemplified by the epithelial to mesenchymal transition [77], [78]. Epithelial cancer cells are adhered to the surrounding cells and the extracellular matrix forming the tumor tissue. When an epithelial cancer cell acquires a mesenchymal phenotype, it loses the adhesion properties and migrates to a secondary place to form a metastatic tumor. Thus, *in vitro* characterization of the adhesion capacity of living tumor cells by imaging polarimetry might give key information on the presence of cells with the ability to migrate and invade other tissues without the need to use time-consuming and observer-dependent labelling method. For these reasons, polarimetry could be a good option as a label-free method to characterize the adhesion process.

### **Cellular motility**

Cell motility is the ability of cells to move independently using its own energy. Cell motility is presented in different ways: cells can move along a substrate crawling or, like epithelial cells, detach from their surrounding cells and migrate. Also, certain type of cells can swim thanks to cilia and flagella.

Cells move at very different rates (from 0.01 to more than 100  $\mu\text{m/s}$  [75]) depending on the mechanism they used to produce the movement. Fastest cells like sperm, ciliates and bacteria are able to swim very quick thanks to their appendices. At the other extreme, cells with rigid cell walls such as fungal, algae and plant cell are immobile. Other mechanism to produce mobility include the use of actin filaments, and microtubules that conform the cytoskeleton of the cell.

This capacity give cells the opportunity to move to a region with better conditions for living and proliferation. It also plays an important role in the spreading of diseases like cancer since cells from a primary tumor can move to other nearby tissues or pass to the bloodstream conquering new parts of a body and causing the metastasis.

## **4.2 Cell death**

Programmed cell death is a built-in capacity in virtually all cells of multicellular organism and it is necessary in order to maintain the correct functioning of a living organism. Cell death is an important process, key to control the population of cells and ensure the correct growth of a tissue, embryonic development, regulation of cell viability, etc. Abnormalities of the programmed cell death contribute to a number of

diseases, including cancer, neurodegenerative diseases such as Alzheimer's disease and Huntington disease, acquired immune deficiency syndrome (AIDS), myocardial infarction and stroke.

### 4.2.1 Apoptosis and necrosis

Although a cell can die in many ways, we focus our attention in two of them: apoptosis and necrosis. Apoptosis corresponds to a programmed cell death, this is, like a natural way of death programmed in the cells, which commit suicide. On the other hand, necrosis or accidental cell death, occurs when cells receive a structural or chemical attack that kills them.

#### Apoptosis

It is the most common way of programmed cell death, this is, an active cellular process that culminates in cell death. This may occur in response to developmental or environmental cues or as a response to physiological damage detected by the cell. For example, it is well known that chemotherapy induces apoptosis in tumor cells.

Apoptotic cell death occurs in two phases: the latent phase and the execution phase. In the latent phase, although the death process has already begun, it is not possible to see any physical or morphological change in the cell and it looks just normal and healthy. During the execution phase several structural and biochemical changes occur. This is in agreement with the fact that plasma membranes suffer major changes during the apoptosis process including loss of phospholipid asymmetry. This phospholipid redistribution between inner and outlet leaflets of the membrane provokes interfacial forces able to modify the structure of transmembrane proteins. Also, alterations in membrane tension result from the modification of membrane-associated molecules and the intracellular and extracellular mechanical stimuli, producing morphological distortions and changes in the membrane curvature [79]. As a result, the cell shrinks and apoptotic cell blebs appear. Finally the cell collapses and fragments into membrane enclosed apoptotic bodies, maintaining the integrity of its plasma membrane.

Classes of cells that undergo apoptosis are: developmentally defective cells, cells whose cell cycle is perturbed, virus-infected cells and chemotherapy-treated cells. This last kind is the one that we focus in this work, since we will treat cancer cells with a chemotherapy in order to induce apoptosis. This reaction has motivated researchers to look for new and effective drugs that generate this response in cells.

#### Necrosis

Necrosis occurs when a cell is damaged in a non-reversible way. This kind of accidental cell death is characterized by the swell of the cell membrane, which becomes permeable. Water rushes into the cell so that it inflates and finally the cytoplasm bursts. The cell undergoes a generalized process of autodigestion and destruction of the cellular structures and all the content of the cell flows to the

exterior causing an inflammatory response. Necrosis often involves large groups of neighbouring cells.

### 4.2.2 Protocols to quantify cell death

Cell health can be monitored by numerous methods. We will focus on two of the most commonly used tests:

#### **Alamar Blue<sup>®</sup> [80] cell viability assay protocol**

This assay evaluates the cell viability based on fluorescence measurements. It is based on the active compound resazurin, a cell permeable, non-toxic weakly fluorescent blue indicator dye. This component penetrates inside the live cells where it suffers a redox reaction transforming into resorufin that is highly fluorescent.

With Alamar Blue the cells remain fully functional, viable and healthy, unaffected by the presence of the indicator, which is a property unique of this technique.

#### **Trypan blue exclusion test of cell viability [81]**

This test is used to determine the number of viable cells present in a cell suspension. Living cells have their cell membranes intact so that the dye used can not penetrate inside them. This is not the case of death cell, in which the dye can penetrate and colour the cytoplasm. As a result, dead cells will appear dark (stained) while the living ones will be seen clear under the microscope.

The protocol consists in mixing a cell suspension with the dye, then place a drop in a hemacytometer (a especial slide with a grid) and finally count the unstained (viable) and stained (nonviable) cells.

## 4.3 Optical properties of cells

Optical phenomena such as absorption, light scattering, refraction and reflection, among others, determine the interaction of light with any system and its propagation through it. Therefore, optical parameters that are affected by such phenomena like transmission, extinction, depolarization, etc., are strongly related to the constituents and structure of the system in which the light propagates. This is what happens with cells; its optical response can be related, for instance, to its intracellular mass and concentration [82]. Cell refractive index, in particular, is of relevant importance because it can provide a lot of information about the structure of a cell or about metabolic processes such as mitosis, infection, etc., and it can be related to other biophysical properties such as mass or protein concentration, elasticity, conductivity, malignancy, etc.

From the measurement of the average refractive index of cell population in suspension by means of polarized light [83], to obtaining an effective refractive index of a single cell, over the years, several techniques have been developed in order to achieve the

measurement of the cell refractive index. Nowadays, new techniques such as full-field optical coherence microscopy [19], confocal microscopy, phase amplitude microscopy and more complex optical systems like graphene based optical sensors [84] could allow very soon to map the refractive index of a single cell with great detail and to obtain 2D and 3D images with high resolution. The information provided by these new methods will be used in a variety of applications in fields like cell biology, hematology and pathology.

One of the most interesting applications is the differentiation of normal and cancer cells. Normal, healthy cells have an average refractive index of around 1.353 while cancer cells have a higher value ranging from 1.370 and 1.400 [19]. Since cancer cells present an abnormal cell cycle with high proliferation rate, the increasing of the refractive index is believed to be related with higher concentration of biomolecules and with the increase in cell proliferation. Several studies also show that the nuclear refractive index is higher for malignant cells. This significant difference between refractive indices can also be useful to detect circulant tumor cells (CTCs) in blood. These cells are the cause of metastasis and are present in very low concentration. The abnormal proliferation of tumor cells may be detected and an early diagnosis of the disease could be possible. Other applications include the detection of unhealthy or infected cells, and the diagnosis of certain diseases such as anemia and malaria. Also, variation on the refractive index can be used for cell growth monitoring, for studying the morphology of cells and the refractive index of different organelles and for measuring the hemoglobin concentration in red blood cells which can be an indicator of infection [84].

### 4.3.1 Cell Imaging

Typically, cell size is in the range on microns (1-100  $\mu\text{m}$ ). This means that, in order to image them with certain degree of resolution, we need to use some kind of microscopy, optical microscopy most often, since we are restricted to the visible spectrum, where the possible damage produced on cells is greatly avoided.

There are several techniques that are being used to do this. Cells are mainly transparent and water is a major component. This means that the contrast of images taken by classic techniques such as bright field microscopy is quite low. To overcome this problem, techniques based on interferometry, such as phase contrast or differential interference contrast (DIC), use interferometry to improve contrast and enhance the visibility. Also, very thin samples can be imaged by dark field microscopy, where only scattered light is collected. Confocal microscopy helps to increase both resolution and contrast, although it is quite a demanding technique in terms of equipment. Another option to produce contrast is to stain the samples with a fluorescent dye.

Finally, we have another source of optical information from the cell: polarimetry. This is the technique we will use in this work. For instance, it has proved its usefulness to identify and discriminate cancer cells [21]. We suggest that polarimetry could also be useful for the identification of processes that take place inside a cell, like the phase in the cell cycle (mitosis), or to distinguish some changes in its state (apoptosis) or

shape (migration). In this way it can be useful, as it is intended to show in this work, in the process of measuring the efficiency of chemotherapy treatments applied to different cancer cell lines.

Part II  
RESULTS



# Chapter 5

## Polarimetry of cancerous cells

### 5.1 Introduction

This chapter is focused on the analysis of cancer cells with polarimetry. In particular, several cell lines are treated with chemotherapy drugs that can induce cell death and the process is monitored by observing the changes in the polarimetric response of the samples.

The first part of the chapter is dedicated to describe the experimental setup employed to perform the experiments and the initial test done in order to check its correct functioning. Then, the different cell deposition methods are described. The main part of the chapter is dedicated to the detection of samples in which cell death has been chemically induced. We performed imaging polarimetry over samples of different cells lines, all treated with a chemotherapy drug. Mueller matrices of control (non-treated) and treated samples are measured, and different methods of analysis of the matrices are applied, in order to find polarimetric parameters that are sensitive to the process. This would allow to asses the efficiency of a chemotherapy drug on a certain cell line or to monitor different processes that take place in cells. It could eventually be a tool to check the cell viability and the cell state.

Along this chapter, experiments on several cell lines will be presented:

- ▷ MCF7: breast cancer cell line. It is an epithelial and adherent cell line.
- ▷ U937: a human monocytic cell line from lymphoma. These cells grow in suspension.
- ▷ HT29: human colon cancer cell line. They are epithelial and adherent.
- ▷ THP1: a human monocytic cell line from peripheral blood (leukemia). They grow in suspension.

## 5.2 Experimental setup

### 5.2.1 Dual Rotating Compensator Polarimeter (UC)

The experimental setup can be described as an imaging dynamic polarimeter microscope which allows to measure the experimental Mueller matrix at different wavelengths within the visible spectrum.

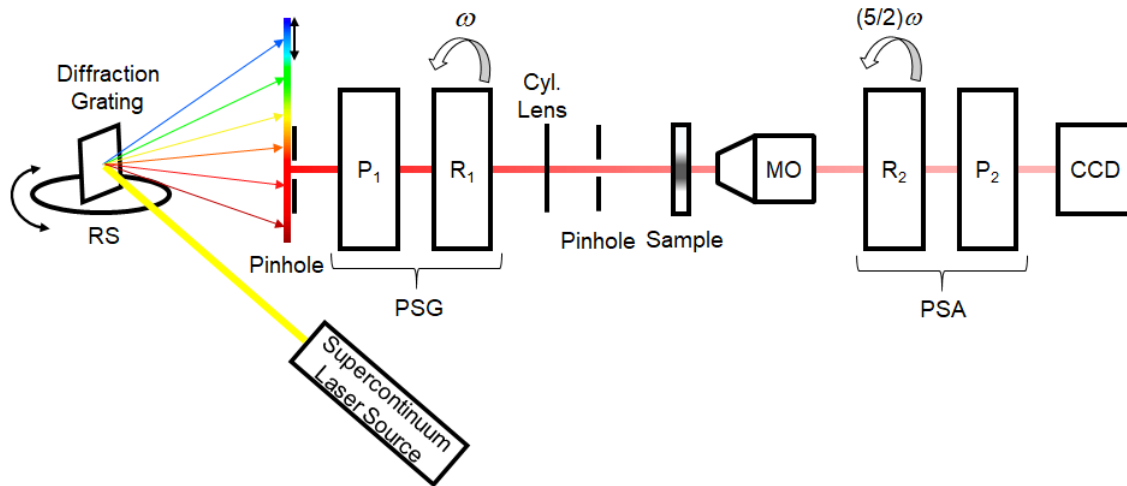


Figure 5.1 - Schematic of the imaging dual rotating compensator polarimeter. The light source is a supercontinuum laser. A diffraction grating placed on a rotary stage (RS) together with a pinhole allow to select the desired wavelength. P1 and P2 are polarizers, R1 and R2 are retarders (quarter waveplate) and MO is the microscope objective. PSG and PSA stand for Polarization State Generator and Analyser respectively.

Figure 5.1 describes how the instrument works. Being an Imaging Dual Rotating Compensator Polarimeter Microscope, it works under a dynamic regime registering a long number of polarization combinations. It consists of a polarization state generator (PSG) composed of a polarizer (P1) and a retarder (R1), a sample holder, a 5x microscope objective (MO) which allows to study the sample in the microscopic range and a polarizer state analyzer (PSA) which in turn is composed of another retarder (R2) and an analyser (P2). A cylindrical lens is necessary in order to correct the longitudinal elongation of the beam selected by the pinhole due to the splinting of the main beam in the diffraction grating. The calibration and use are fully described in several works [67, 85–87]. The microscope objective is interchangeable to select the magnification. Finally the images are captured with a 12 bit camera. Both retarders rotate synchronously with a speed ratio of 5/2 completing a full measurement cycle of 200 images of  $640 \times 640$  pixels ( $180 \times 180 \mu\text{m}$  approximately). The Mueller matrix is calculated for each pixel, from its corresponding cycle, by means of a Fourier Transformation algorithm [88]. The light source is a supercontinuum laser (FemtoPower 1060 made by Fianium) which allows to perform measurements in the visible spectrum, from 480 to 680 nm. A diffraction grating placed on a rotary stage (RS) together with a pinhole allow to select the desired region of the spectrum. All the measurement presented in this chapter were performed with objective TU Plan

Fluor, 5x,  $N.A = 0.14$  from Nikon and at a center wavelength  $\lambda = 634$  nm. The value of 634 nm seemed a good option since it is adequate for keeping the source working in long periods of time, and it can be replaced by a He-Ne in case of failure. From the biological point of view, our main observations seem to be almost invariant with respect to wavelength changes.

Figure 5.2 a) and b) are actual pictures of the setup in the laboratory, showing the two main arms of the polarimeter.

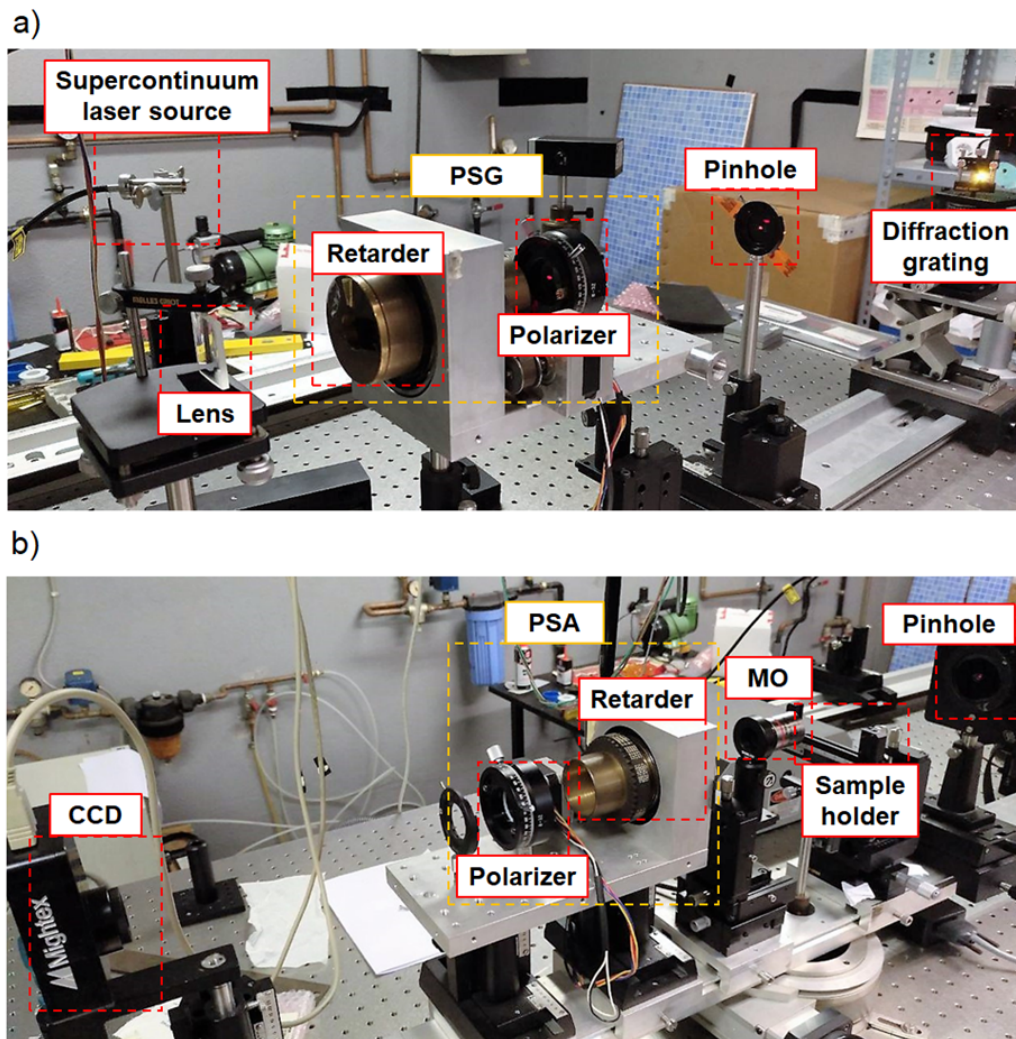


Figure 5.2 - Pictures of the two arms of the polarimeter: a) supercontinuum source and polarizer state generator (PSG) and b) Sample holder, microscope objective (MO), polarizer state analyser (PSA) and camera (CCD).

### Calibration process

Previously to any sample measurement it is necessary to perform a calibration cycle on a target free configuration in order to characterize the performance of the measuring instrument. Some of the working parameters of the polarimeter are obtained during this process such as the polarizers and retarders azimuth angles and the

retardance of the two waveplates.

Figure 5.3b shows the calibration Mueller matrix which has to be ideally the 4x4 identity matrix, that is, the Mueller matrix of the vacuum, except for the element  $m_{11}$  which represents the intensity distribution of the illumination.

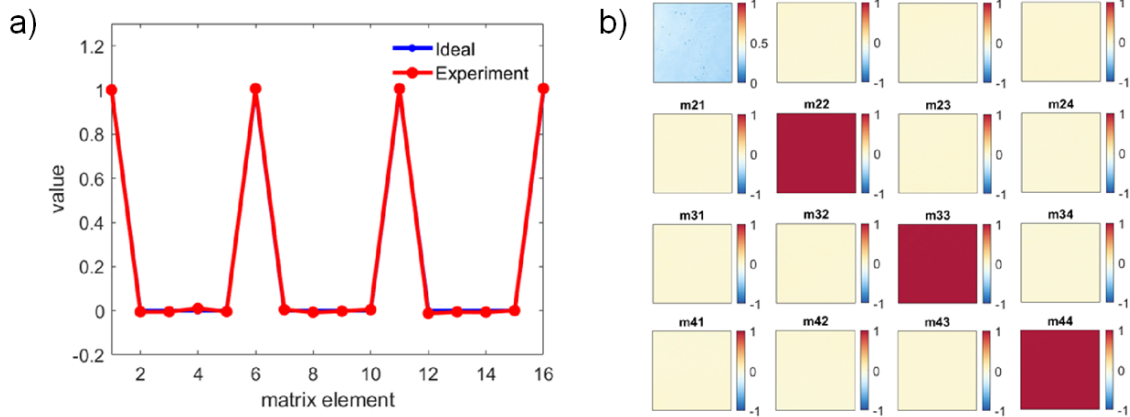


Figure 5.3 - a) Mean values of the elements of the experimental calibration matrix (red) compared with the ideal one (4x4 identity matrix in blue) and b) image Mueller matrix of a calibration cycle.

A very homogeneous calibration is achieved, with a highest relative error of  $1.6 \times 10^{-3}$  this is, the largest deviation from 0 or 1 of all 15 elements of the normalized  $\mathbf{M}$ . From a calibration measurement, we can obtain the mean values of the polarimetric parameters employed along this work (Figure 5.4). They can be used as a reference for sensitivity in the actual measurement of samples. Ideally, this values are supposed to be zero.

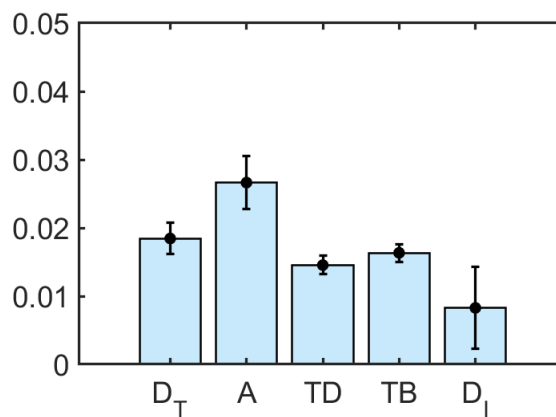


Figure 5.4 - Diattenuation ( $D_T$ ), anisotropy ( $A$ ), total dichroism ( $TD$ ), total birefringence ( $TB$ ) and depolarization index ( $D_I$ ) obtained from a calibration measurement. Error bar is the standard deviation of 5 calibration cycles.

## 5.3 Initial tests

Experimental setup was tested satisfactory with some optical elements of known behaviour such as polarizers or  $\lambda/4$  retarders. In addition to this, another more demanding tests will be added in order to get closer to the final use that will be given to the experimental setup.

### 5.3.1 Operating the setup with a birefringent media

Once we checked that the calibration process works correctly, we measured the Mueller matrix of some well-known samples in order to verify the proper functioning of the setup and the decomposition algorithms used to analyse the measured matrices.

As a reference sample, we used a film of Scotch<sup>TM</sup> tape. We chose this material because it shows an important birefringence but also because it has very standard properties. It is easy to find, easy to manipulate and really affordable. In addition, its geometrical axis is well specified by its winding direction and its rough surface produces an important depolarization that must be accounted for when analysing the measured  $\mathbf{M}$  associated to it. Interestingly, it is possible to play with the orientation and to stack several films to obtain cumulative values of some of the properties. We took as a reference the work done with these systems by Sang Hyuk Yoo et al. in [89] and focused on the parameters associated to birefringence ( $LB$  and  $LB'$ ).

We fabricated four different samples (Figure 5.5) oriented in several positions. Then, we stacked several film layers in each of the orientations and measured the transmission Mueller matrix of the sample each time a layer was added. Values of linear birefringence ( $LB$  and  $LB'$  given by Equations 3.54) were calculated after applying the Differential Decomposition.

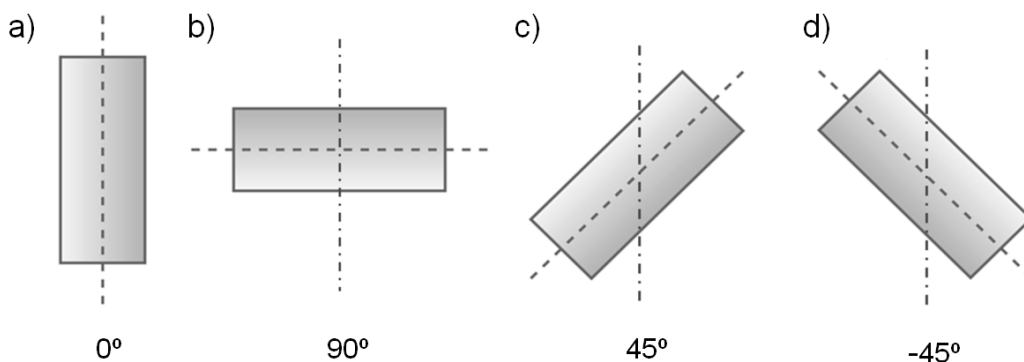


Figure 5.5 - Units of the four samples of Scotch<sup>TM</sup> tape oriented in different directions used to perform the experimental test. Dashed lines represent the geometrical axis of the samples.

Figure 5.6 shows the values of the linear birefringence as a function of the number of layers of tape stacked in vertical and horizontal position. In the same way, values of  $LB$  for sample oriented at  $45^\circ$  and  $-45^\circ$  are shown in Figure 5.7.

Samples in vertical and horizontal position (Figure 5.5a and b) present retardance mostly along the  $xy$  axis ( $LB$ ), this is, its geometrical axis, with almost null values of  $LB'$  and  $CB$ . On the other hand, the samples oriented at  $45^\circ$  and  $-45^\circ$  present significant values of  $LB'$  but null values of  $LB$  and  $CB$  which is in agreement with the new direction of the optical axis. In all the configurations of the samples, the retardance (or birefringence) seems to increase linearly with the number of layers approximately at  $0.18 \pm 0.01$  rad/layer with opposite sign for orthogonal orientations. Slight variations in the circular birefringence might be due to imperfections in the alignment between layers as they are manually stacked.

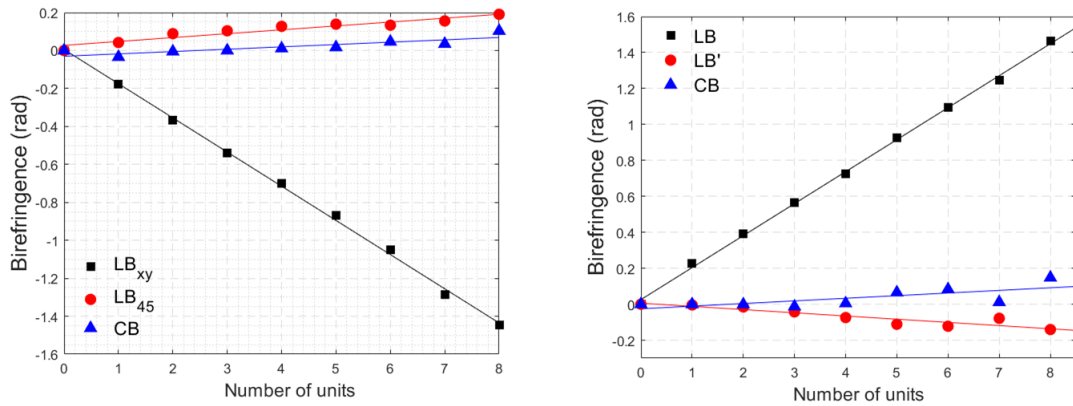


Figure 5.6 - Linear and circular birefringence of several units of an anisotropic sample stacked on vertical position (left) and horizontal position (right).

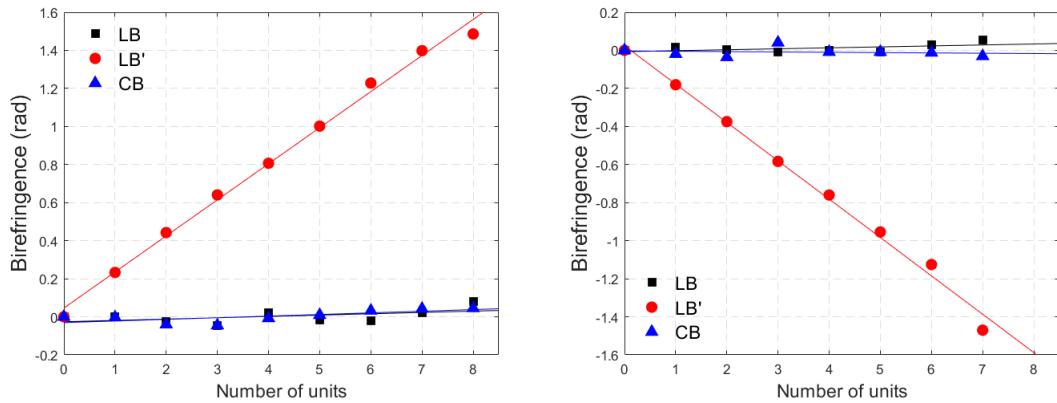


Figure 5.7 - Linear and circular birefringence of several units of an anisotropic sample stacked at  $45^\circ$  position (left) and  $-45^\circ$  position (right).

With this initial test we verify that both the setup and the programs used to analyse the matrices work properly, since we obtain consistent values of the birefringence for samples in several orientations.

## 5.4 Cell samples

Samples made of cells are a peculiar target since they need very specific conditions to stay alive and stable. For this reason, the present section is dedicated to the

description of the steps followed to prepare and experimental analyse this kind of samples.

### 5.4.1 Cell deposition methods

Preserving the cells in good conditions for the experiment was difficult because the time require by the measurements demanded a high stability of the samples. We tried several sample preparation protocols to keep the cells alive. Different procedures for the deposition of cells imply different media for the cells and different ways to get fixed to the surface. It also produces images with different contrast and stability.

Before describing the different deposition methods attempted, it is necessary to describe a common method used to fix cells onto a microscope slide: the cytopspin technique, described in detail in [90]. Basically, this technique consist in harvesting the cells from a culture, count the viable ones, resuspend them in PBS (phosphate buffered saline employed in cell biology to dilute, suspend or clean cells) and then place 100-200  $\mu\text{ml}$  in a funnel that will be put, mounted together in a holder with a filter and the microscope slide, in a cytopspin centrifuge. Sample is centrifuged during a 5 minutes at 600 r.p.m (times and velocity can be variable depending on the cell line) so that cells remain immobilize in an area of 6 mm in diameter forming a layer. Finally, cells can be let air exposed or covered with a cover slide or agarose (a transparent polysaccharide which is liquid when is warm but that gelifies at room temperature even at low concentrations).

Next, the different methods attempted are described. In all methods described here cells are on a glass slide:

- ▷ *Method 1*: Cytopspin with air exposed cells (without cover glass).
- ▷ *Method 2*: Cytopspin plus a drop of PBS and covered with a cover glass.
- ▷ *Method 3*: Cells suspended in a PBS drop on a microscope slide and covered with a cover glass.
- ▷ *Method 4*: Cells adhered to a cover slide and fixed to a microscope slide (method only valid for adherent cells).
- ▷ *Method 5*: Cytopspin plus agarose covering the cells.

Basically, the main problems found were related to the drying of the cells, and the PBS crystal formation because they produce artefacts (errors introduced by the technique) that affect the polarimetric measurements in a significant way.

The first proofs were made by leaving the cells uncovered on the microscope slide (*Method 1*). Cells will dried completely in a short time changing their shape due to dehydration. Also, and because of the remains of the saline buffer used in the sample preparation, some little crystals appeared, something really undesired for

polarimetric measurements (see Figure 5.8a).

As a result of covering the samples (*Methods 2, 3 and 4*) to prevent drying, we ended with images that did not show crystals but, had low contrast and also small bubbles that produce a characteristic polarimetric signal. *Methods 2 and 3* included either adding a drop or generating a suspension of cells in PBS. This did not work either because the cells will not be still and the contrast will be reduced to a minimum (Figure 5.8b). *Method 4* offered a good contrast but unfortunately, it still dries very fast and, since it requires cells growing adhered to a cover slid, it is only adequate for adherent cell lines (Figure 5.8c).

Finally, we found that the best way to preserve sample from drying and avoid crystal formation is to cover the cells with a thin layer of agarose at low concentration (0.3 %). This will keep the sample humid and still at place without affecting the optical properties of the samples. However, after trying with different concentrations of agarose, we concluded that it is necessary to use low concentrations since at high concentrations some inhomogeneities appear (Figure 5.8d).

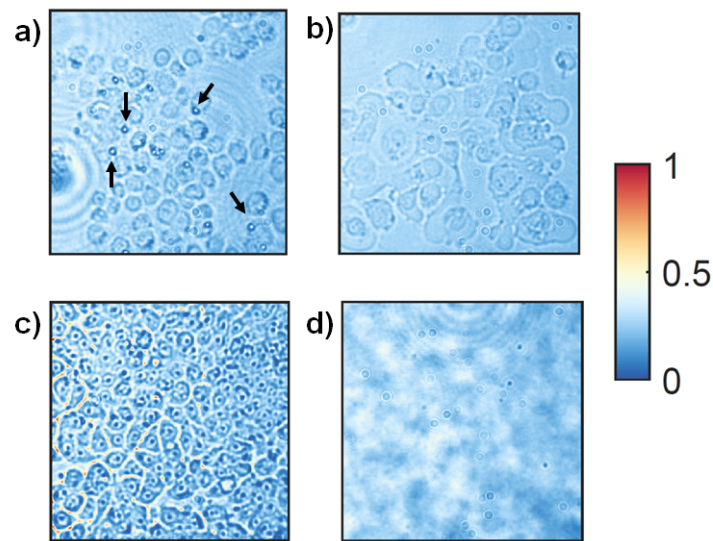


*Figure 5.8 - Images of different situations encountered when testing several cell deposition methods. a) Method 1: drying and crystal formation (black arrows), b) Method 3: low contrast, c) Method 4: cells adhered to a cover showing a good contrast and d) inhomogeneities due to high concentration of agarose.*

Finally, for the sake of the repeatability of the experiments we also decided to use enough cells to cover the whole surface of the image in order to get signal mainly from the cells and reduce the weight of the light coming from the surface of the slide and from regions containing just agarose.

#### 5.4.2 Measurement of the Mueller matrices of cells

With the experimental setup described in Section 5.2.1 we started our first measurements of living biological cells. The first question to be answered is if this kind

of sample shows enough polarimetric response as to be reflected in the Mueller matrix. To illustrate this stage of the research we have measured the Mueller matrix of different cell lines in the visible spectrum. These samples have been prepared according to *Method 1* described in the former section. Figure 5.9 shows the Mueller matrix image of the HT29 cell line, measured at a wavelength of  $\lambda = 634$  nm with a 5x microscope objective.

Cells have an approximate diameter of  $10 \mu\text{m}$  and have been deposited on a microscope slide by citospin technique. The element  $m_{11}$  of the Mueller matrix represent the intensity (an image of the cells plane) where the locations of individual cells and their membranes are clearly visible.

Once we have the experimental matrix (where all elements are normalized to the  $m_{11}$  values), we have analysed it with the MMPD, MMT and MMDD methods so that we can compare the parameters given by each of them.

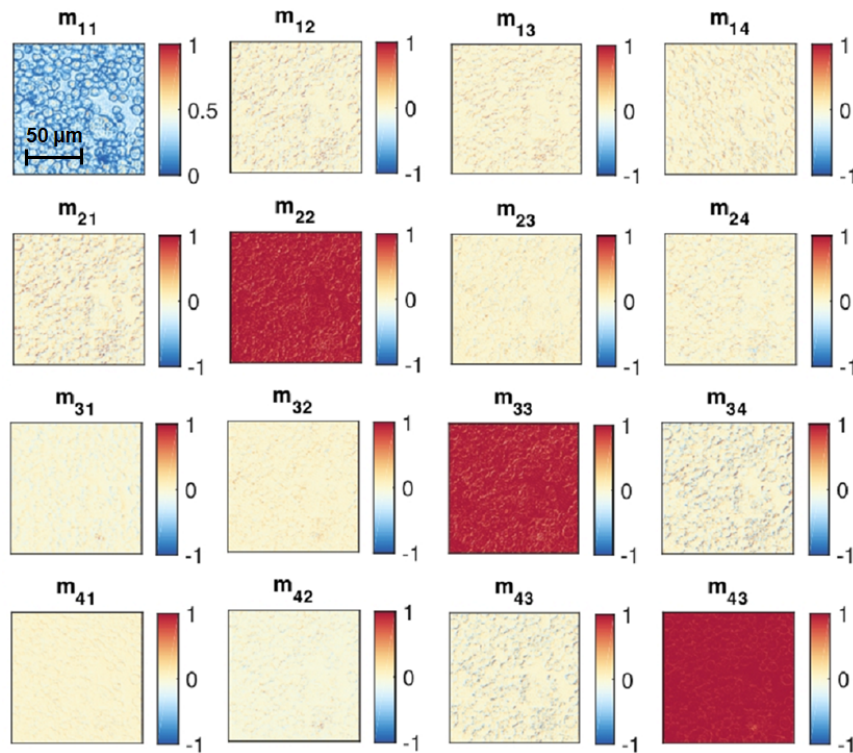


Figure 5.9 - Experimental Mueller matrix image of a HT29 cell line performed at  $\lambda = 634$  nm with a 5x microscope objective.

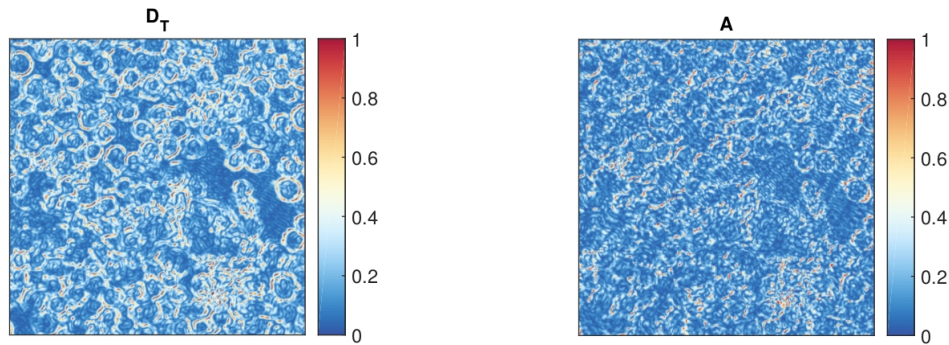


Figure 5.10 - Total diattenuation ( $D_T$ ) and anisotropy ( $A$ ) for a sample of HT29 cell line.

At a first glance, the Mueller matrices obtained from cells and working in transmission configuration are variations from the general shape of the unitary matrix, showing that the response of these samples in these conditions is very small. The different decompositions show that samples introduce a small amount of diattenuation, retardance, optical rotation or depolarization. Likewise we observe that the samples are mainly isotropic since the value of the anisotropy  $A$  is close to zero for most parts of the samples. However, some activity can be found, apparently, in the boundary of the cells. Among all the polarimetric parameters that these decompositions offer, both diattenuation and anisotropy (see Figure 5.10) seem to show the best contrast and maybe be suitable for the analysis.

### 5.4.3 Detections of PBS crystals

PBS (phosphate buffered saline) is one of the most common buffers used in biology to handle the cells. It is an aqueous and saline solution that contains sodium chloride, sodium phosphate, potassium chloride and potassium phosphate. This buffer maintain and adequate pH for the cells and replicate the osmolarity and ion concentrations of the human body.

As a result of using this kind of buffer, rich in salts, crystals of PBS form when the samples dry. This can affect the polarimetric measurements, producing an unwanted –but easy to recognize– signal in the surroundings of cells. The growing process and shape of these crystals are well know [91–94].

We observed two kind of crystal formation, both of them affecting the values of the Mueller matrix and the polarimetric parameters.

When we tried to add PBS solution and cover the samples with a glass slide, in an attempt to keep sample humid and prevent cell from drying, we observed rapid growing of big crystals with a characteristic branched or dendritic arms, as shown in Figure 5.11 left. On the other hand, when PBS was not added, still little crystals appear with time, as the sample dries out (marked with black arrows in Figures 5.8a 5.11 right), probably due to remains of the buffer solution.

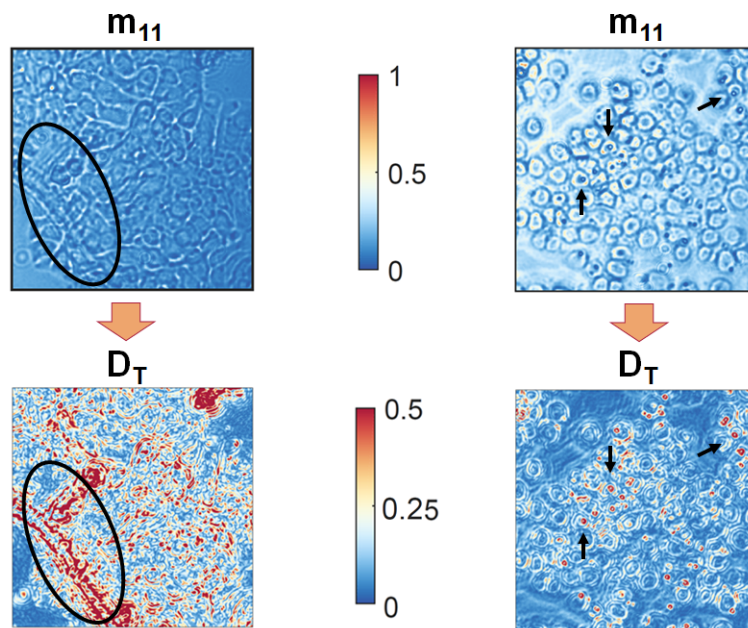


Figure 5.11 - Intensity images ( $m_{11}$ ) and total diattenuation parameter (TD) of some PBS crystals formed during measurements of cells using deposition Methods 1 (right) and 2 (left). Big crystals are marked with a black ellipse and small ones with black arrows.

Both kind of crystals are difficult to identify in a normal intensity image (element  $m_{11}$  of the Mueller matrix) but are highlighted when the matrix is processed. Diattenuation seems to be specially sensitive to the presence of this type of artefacts.

In the final improved protocol used to prepare the samples (employing *Method 5*), PBS crystals were no longer detected.

## 5.5 Cell state assessment: apoptosis detection

When a population of cells is treated with a chemotherapy medication, they become apoptotic (see Section 4.2), this is, they begin a non-reversible process that ends with the cell death. Throughout the experiments, we used 3 types of medications: cisplatin, etoposide and doxorubicin. Depending on the kind of drug, the concentration used and the time of treatment, the effectiveness on a certain cell line is variable. An equal treatment applied in two different cell lines could affect them on very different ways producing a higher rate of cell death in a certain cell line when concentration is increased. This is illustrated in Figure 5.12. In the same way, different chemotherapy drugs applied on the same cell line, also produce differences in cell viability (see Figure 5.13). Finally, lower concentrations of a chemotherapy drug applied for the same time to a cell population does not produce the same results that at higher concentration, being the higher concentration more effective, as it is shown in Figure 5.14. Because of these, it is very important to design a correct treatment depending on the kind of cell we are working with.

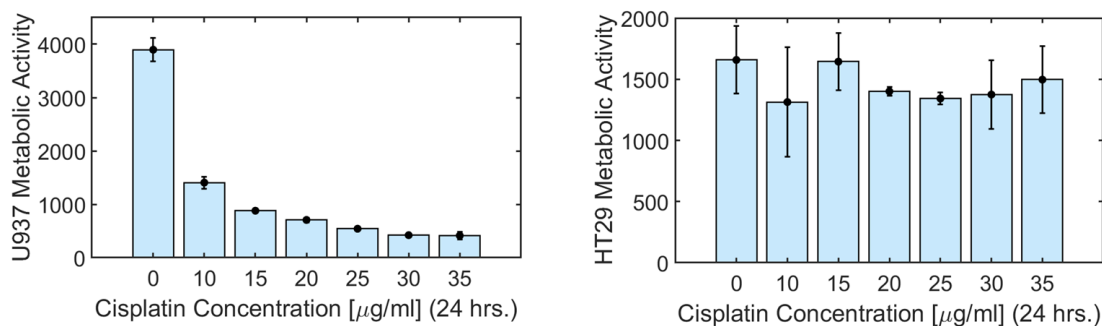


Figure 5.12 - Metabolic activity of U937 and HT29 cells obtained by Alamar Blue test when treated with increasingly higher concentrations of cisplatin for 24 hrs. Error bars are the standard deviation of three measurements. Measurements were done at Unity of Genetics (Hospital Universitario Marqués de Valdecilla)

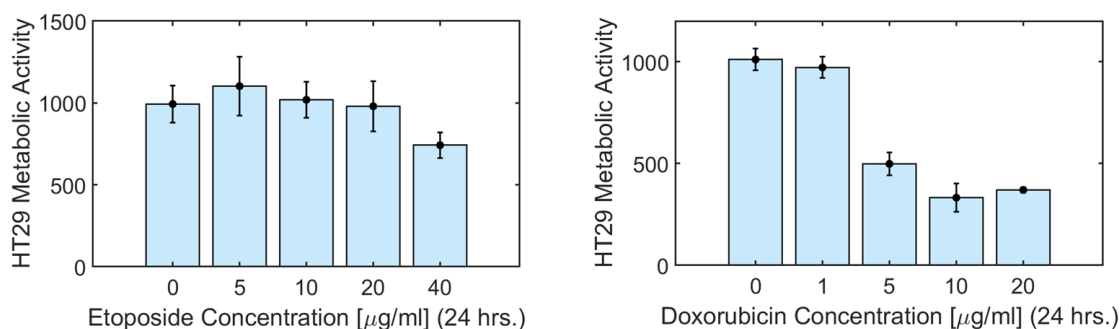


Figure 5.13 - Metabolic activity of HT29 cells obtained by Alamar Blue test when treated with increasingly higher concentrations of etoposide and doxorubicin for 24 hrs. Error bars are the standard deviation of three measurements. Measurements were done at Unity of Genetics (Hospital Universitario Marqués de Valdecilla)

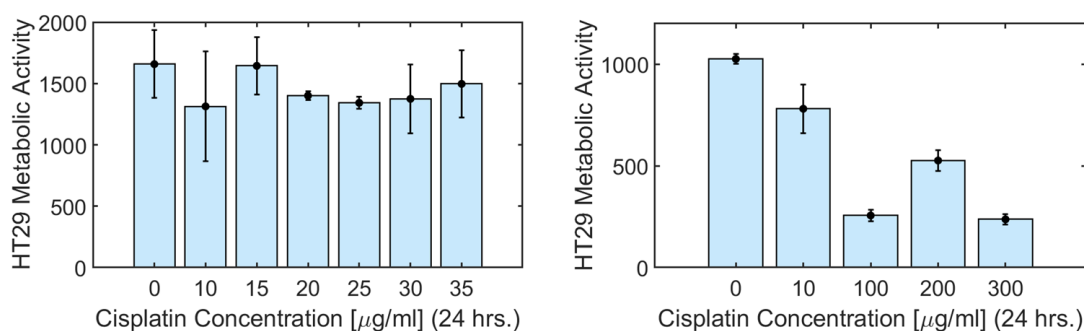


Figure 5.14 - Metabolic activity of HT29 cells obtained by Alamar Blue test when treated with increasingly higher concentrations of cisplatin for 24 hrs. Error bars are the standard deviation of three measurements. Measurements were done at Unity of Genetics (Hospital Universitario Marqués de Valdecilla)

Our aim is to assess if polarimetry can be a tool to detect changes occurring in cells, such as cell death (apoptosis), mitosis, or shape and geometrical changes in their

structure. In order to check this, at first place, we performed a set of experiments on several cell lines and with different chemotherapy medications dedicated to explore the capability of polarization to detect changes in cells and to evaluate the sensitivity of the method to changes produced by the chemotherapy agent. Next, a more systematic study in two cell lines will be shown, with the objective of evaluating the cell death, checking the results offered by polarimetry with those provided by two consolidated methods used in biological cell research.

### 5.5.1 Polarimetric sensitivity to cell death: initial experiments

After the positive results regarding the detection of cells or crystals (Section 5.4), the first point to be addressed if we want to use polarimetry to investigate the processes and changes occurring in cells, is to find out the actual sensitivity of our polarimetric matrix to changes in the biological cells.

#### Tests on different cell lines

In the initial experiments with cell lines, we worked with HT29 and MCF7 cells, and treated them with cisplatin during different times in order to compare the effects of the treatment on both cells lines. Cells were deposited (employing *Method 1*) on a microscope slide and then the Mueller matrix was measured.

Figure 5.15 shows the mean value of diattenuation images after performing MMPD in control (non-treated) and treated samples of HT29 and MCF7 cell lines. The error bars represent the standard deviation of the mean values obtained from all the images, four in the case of HT29 cells and eight images for MCF7 cells.

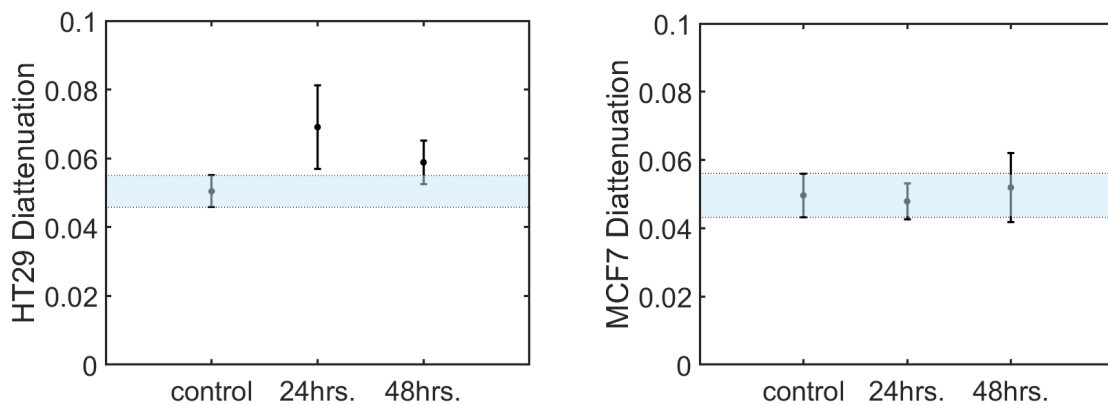
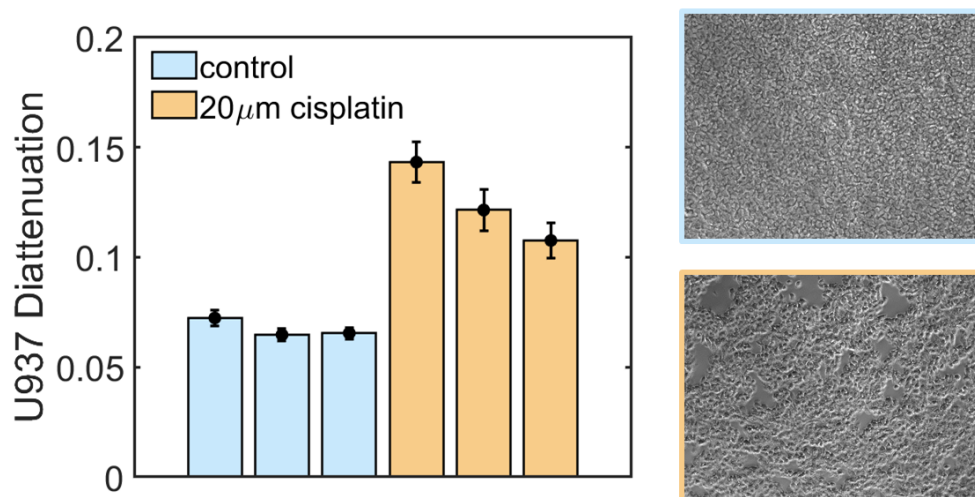


Figure 5.15 - Mean values of diattenuation in HT29 and MCF7 control samples and treated samples at 24hrs. and 48 hrs. after the treatment with cisplatin. Error bars represent the standard deviation of the mean values of the images taken in each case.

In the HT29 cells, difference between control samples and treated ones is clearly visible. Treated samples present a value of diattenuation that is higher than the control one, clearly indicating that some process is occurring in the cell. Otherwise, cisplatin seems to affect differently each of the cell lines. While HT29 cells show higher values of diattenuation, it changes very slightly for MCF7 cell line. This is

consistent with the fact that MCF7 cells tends to be more resistant to cisplatin [95, 96] while it induces apoptosis to HT29 [97].

Other experiments performed with cell line U937 treated with  $20 \mu\text{g}/\text{ml}$  of cisplatin for 24 hrs. (Figure 5.16), also show positive results, confirming that diattenuation seems to be sensitive to the effects produced by chemotherapy.



*Figure 5.16 - Mean values of diattenuation for three images of control samples and treated U937 cells sample ( $20 \mu\text{g}/\text{ml}$  of cisplatin). Error bars represent the standard deviation of the mean values of the images taken in each case. On the right side images taken with the microscope are shown.*

From this point, we focused our attention in finding a proper method to fix the cells to the microscope slide in order to work with the samples always in the same conditions and to design a measurement and analysis protocol that allows us to explore the role and information that polarimetry could provide regarding this kind of samples.

### **Effect of other chemotherapy drugs**

Apart from working with several cell lines, we also carried out some trials employing different chemotherapy medications to see which one worked better for our purpose. For example, a treatment of 24 and 48 hrs. of HT29 cells with etoposide (see Figure 5.17) did not produce such clear effect in the diattenuation parameter.

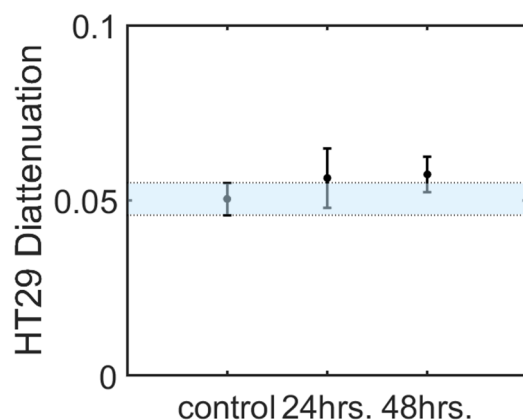


Figure 5.17 - Mean values of diattenuation for two images of control samples and treated HT29 cells with etoposide for 24 and 48 hrs. Error bars represent the standard deviation of the mean values of the images taken in each case.

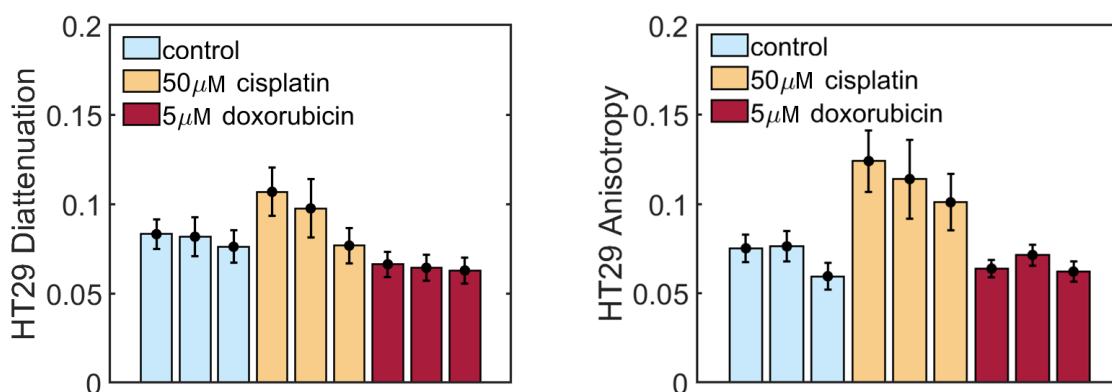


Figure 5.18 - Mean values of diattenuation and anisotropy for three images of control samples and treated HT29 cells with two different chemotherapy medications for 24 hrs. Error bars represent the standard deviation of the mean values of the images taken in each case.

Results from another experiments are shown in Figure 5.18. On this occasion, two sets of HT29 cells were treated with  $50 \mu\text{g}/\text{ml}$  of cisplatin and  $5 \mu\text{g}/\text{ml}$  of doxorubicin respectively for 24 hrs. In view of the results, we can conclude that the effects of cisplatin on both cell lines seem to have a more clear impact on the diattenuation than doxorubicin. From this point, we have focused on the effect of cisplatin.

### 5.5.2 Sample preparation and treatment: final protocol

After several tests we ended up developing a protocol to prepare samples in a way that cells keep in good conditions for enough time to perform the polarimetric measurements. This includes:

- ▷ to maintain the humidity of the cells,

- ▷ to prevent for drying,
- ▷ to and avoid crystal formation,
- ▷ to fix the cells so they do not move during a measurement cycle.

This process is key to ensure reproducibility and repeatability.

Moreover, since our main goal was to evaluate the state of the cells and characterize the cell death, we look also for an standard optimized treatment with the chemotherapy medication.

### **Optimization: final protocol**

The samples undergo a treatment with a chemotherapy drug (20  $\mu\text{g}/\text{ml}$  of cisplatin) in order to induce apoptosis and are examined in fixed time laps (24, 48 and 72 hrs.). After the treatment, cells are placed in a microscope slide by applying a cytopspin technique [90] consisting of a high speed centrifugation to remove the liquid and concentrate the cells on a slide in a layer of 6 mm in diameter. Cell were centrifuged at 600 r.p.m for 5 minutes.

Previous to the cytopspin process, the number of deposited cell is chosen so that a uniform layer of cells is achieved, without gaps or piles of cells. In order to keep cells stable in time and prevent crystals formation due to remains of PBS, the cells are covered with 60  $\mu\text{l}$  of 0.3% agarose which maintains the humidity of the sample.

### **5.5.3 Evaluation of cell death**

#### **U937 cell line.**

U937 leukemia cells are used to perform the polarimetric study related to the effect of a chemotherapy treatment. Following the protocols previously described, cells were treated with the cytotoxic drug cisplatin. Viability tests are performed at 24, 48 and 72 hrs. after treatment. In addition, polarimetric measurements were carried out. Control (non-treated) and treated cells are compared.

Ordinary microscopic images (Figure 5.19) show differences between untreated (A) and the cisplatin treated cells at 24 (B), 48 (C) and 72 (D) hrs. Cisplatin-treated U937 cells are less confluent, show cell shrinkage and become pyknotic (with cytoplasmic and nuclear condensation) at longer times, mostly 72 hrs. (Figure 5.19D). These morphological features are associated with apoptotic cell death [98] and it is well established that cisplatin induces apoptosis in a number of tumour cells, including U937 cells [99].

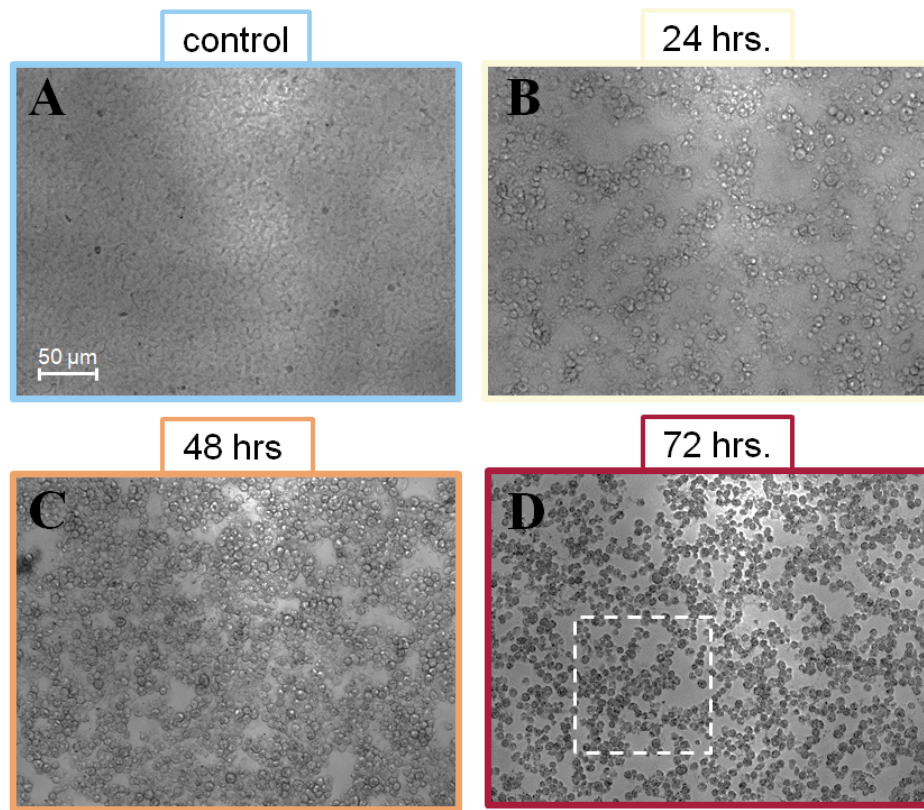


Figure 5.19 - U937 sample images taken by phase contrast microscopy. A) Control sample (non-treated). B), C) and D) 24, 48 and 72 hrs. treatment with  $20 \mu\text{g/ml}$  of cisplatin. White dashed square represent the size of the image taken with the polarimeter ( $640 \times 640$  pixels.)

An important issue concerning the samples is the reduction of the surface covered by cells during the treatment. Because of this, as the treatment progresses, the polarimetric signal comes from both the background (agarose) and the cells, according to the filling factor reached by the cells in the image,  $f_c$ . In order to account for this effect we have introduced a corrected signal  $S_c$  that verifies:

$$S_i = S_c f_c + S_b (1 - f_c) \quad (5.1)$$

where  $S_i$  is the total value of the polarimetric signal obtained in the measured image and  $S_b$  is the polarimetric signal coming from the "empty" background (agarose in our case). The filling factor is calculated for each image by converting them to 8-bit. Then, the image is binarized selecting a threshold that converts pixels occupied by a cell to black and pixels from the background to white (this was done with the free software *ImageJ*<sup>1</sup> and the result was double-checked by eye inspection), see Figure 5.20. In case that the full surface is covered by cells then  $f_c = 1$  and no correction is needed.

<sup>1</sup><https://imagej.nih.gov/ij/>

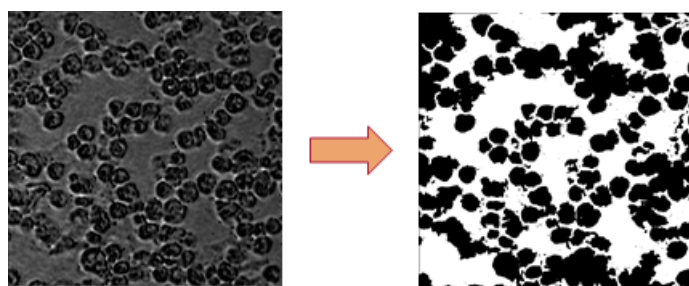


Figure 5.20 - U937 image ( $m_{11}$ ) at 72 hrs. of treatment before and after binarizing.

If we focus on the image of individual cells, Figure 5.21 shows that the treatment also produces a remarkable change in the shape and size of the cells. Afterwards the slide is placed in the sample holder of the polarimeter and the measurement process begins. After each time lapse cell viability is checked through standard methods like assay trypan blue in order to ensure that the treatment is being successful.

The results of the cell viability trypan blue assay at different time points is shown in Figure 5.22. Cell mortality gradually increases over time reaching about 80% cell death by 72 hrs. This result is confirmed by showing that cisplatin reduces the metabolic activity of U937 cells, from 2.4-fold at 24 hrs. to 100-fold at 72 hrs., corresponding to cells undergoing cell death (Figure 5.23).

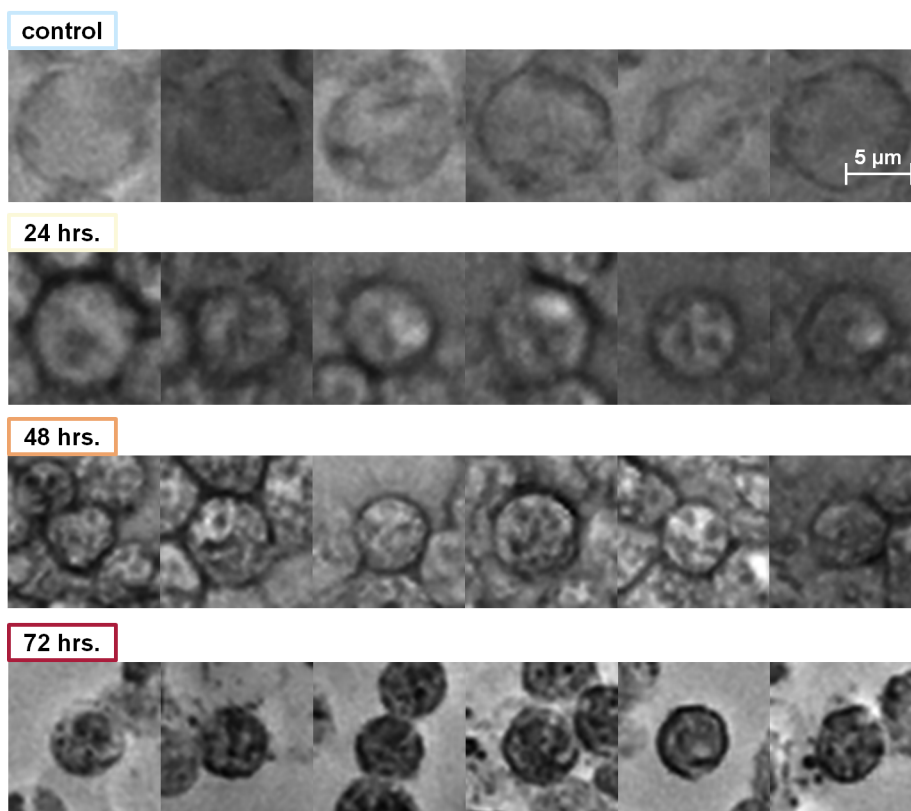


Figure 5.21 - Images of individual cells taken by phase contrast microscopy at different time points of the treatment with cisplatin. The same magnification has been used in the capturing and rendering of these images. Images are  $100 \times 100$  pixels.

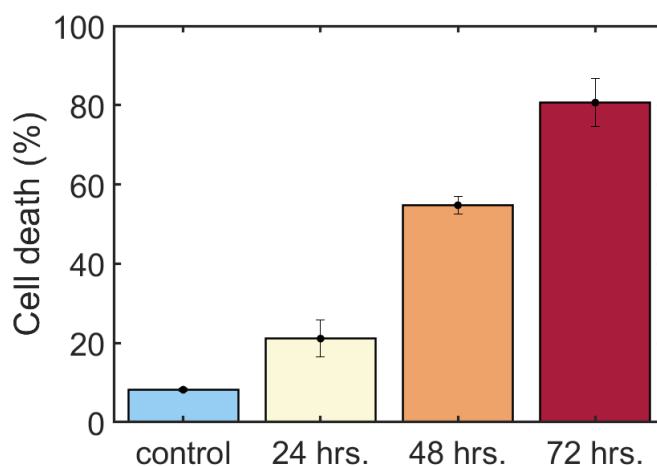


Figure 5.22 - Cell death of U937 cells over time treated with 20  $\mu\text{g}/\text{ml}$  of cisplatin evaluated with trypan blue exclusion test at several time points. Error bar is the standard deviation of three measurements.

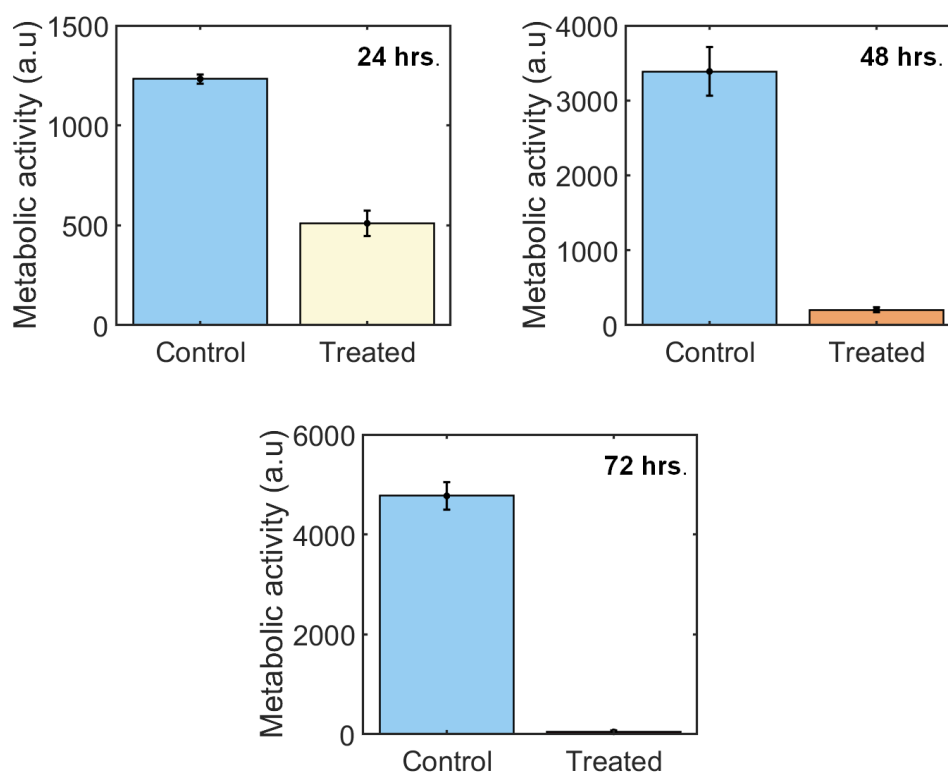


Figure 5.23 - Metabolic activity of U937 cells following a treatment with cisplatin at different time points using the Alamar Blue assay. a.u., arbitrary units. Error bar is the standard deviation of three measurements

After that, 5 Mueller matrix images ( $640 \times 640$  pixels) were measured in 5 different regions for each of the four samples. The regions were randomly selected in the area covered by the cells (circle of 6 mm in diameter). The dashed white square in Figure 5.19D) represents the size of the image taken with the polarimeter ( $180 \times 180 \mu\text{m}$

approximately). These images, as seen in Figure 5.24, constitute the raw data from which several polarimetric parameters can be obtained.

By applying different decomposition methods, these parameters are obtained and finally, in order to condense and quantify the results, mean values of each parameter are calculated averaging over all the pixels. Figure 5.25 shows the mean value of the 5 images of diattenuation for each sample. A slight but significant increase is shown at 24 hrs. ( $p$ -values obtained with both tests was 0.016), when cell death is about 25%. Great differences are observed by 48 hrs. of treatment, when the cell death is above 50%. In addition, the signal at 72 hrs. is more than three times the control signal and variation between images of a set of measurements taken at a given time are always much smaller (around 0.03) than between sets. We found that results are highly dependent of cell confluence, this is, the filling factor  $f_c$  of cells. We used some statistic non parametric test to check if it is possible to tell apart each pair of samples. We apply the Wilcoxon rank test and the Kruskal Wallis tests to our set of data and obtain the corresponding  $p$ -values (see table 5.1).

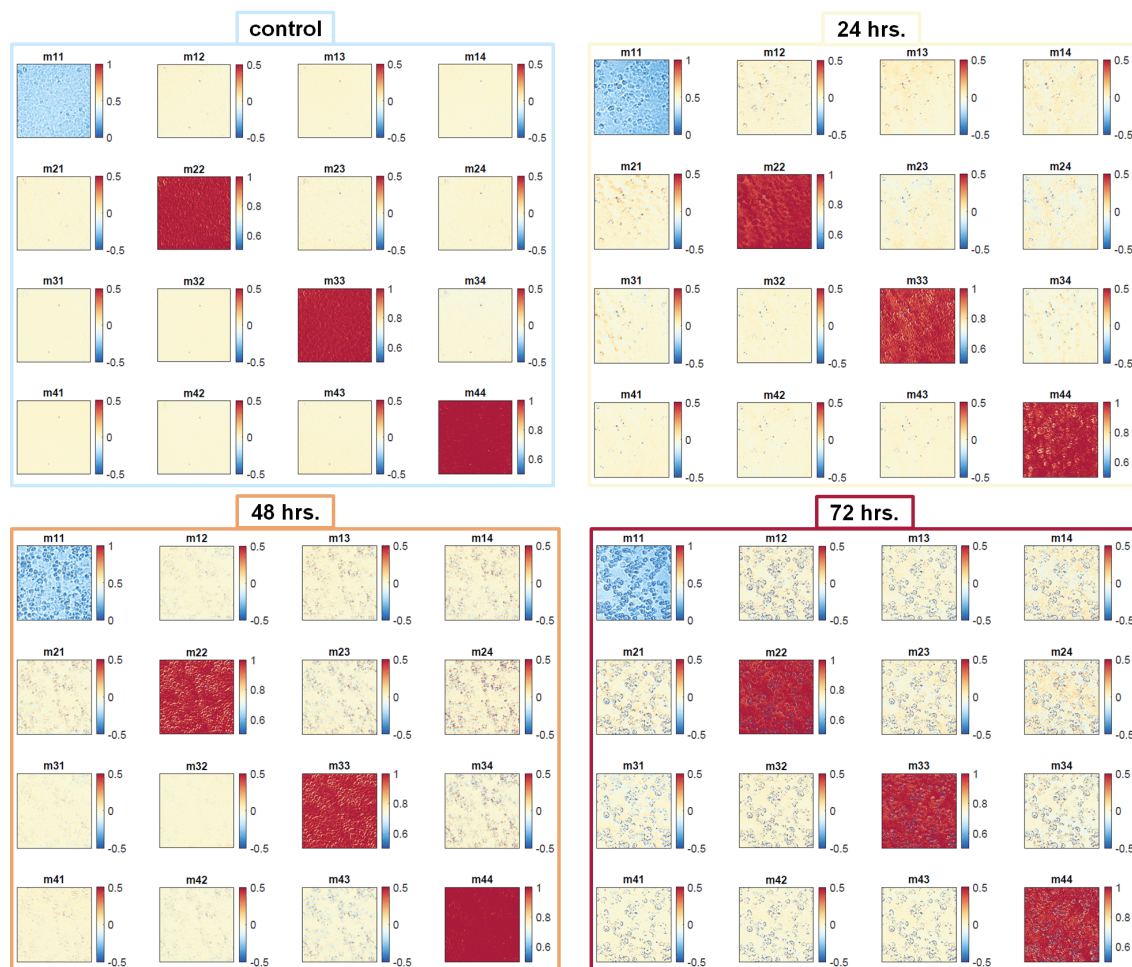


Figure 5.24 - Mueller matrix images of U937 samples at 4 time points during a treatment with 20  $\mu\text{g}/\text{ml}$  of cisplatin.

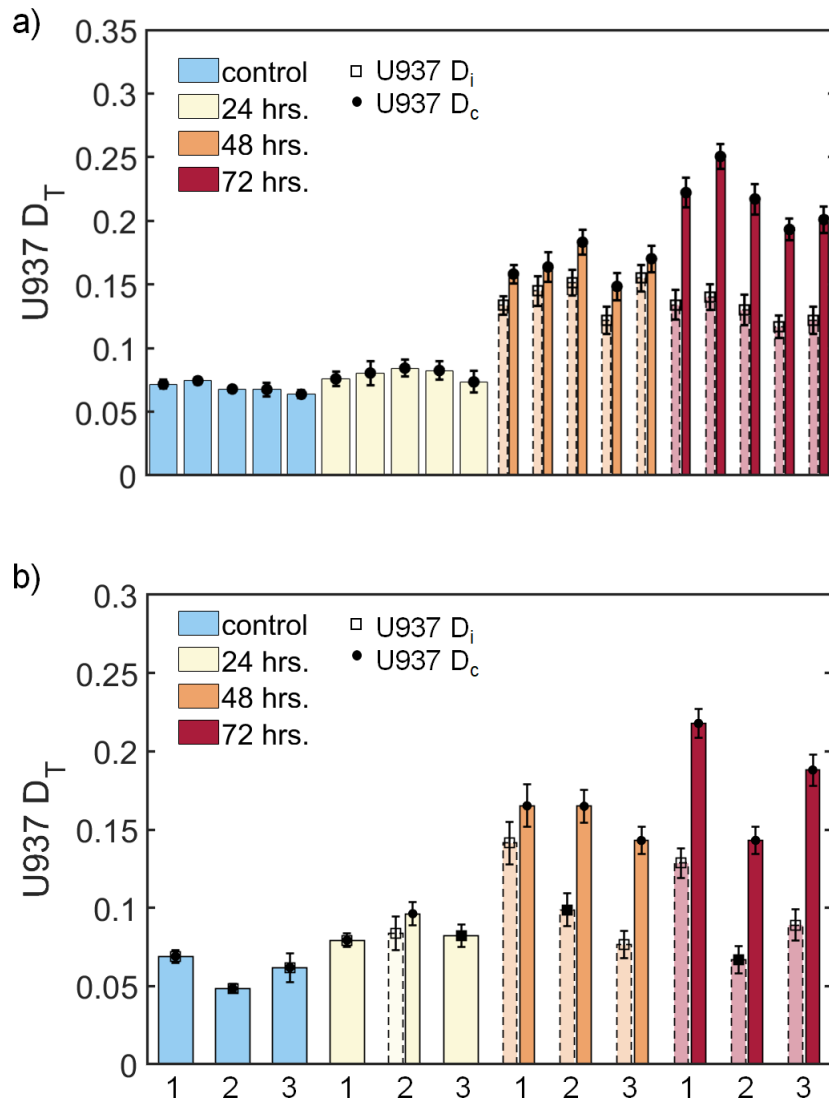


Figure 5.25 - Mean diattenuation ( $D_T$ ) of each of the five images taken from control and cisplatin treated samples of U937 cells. Figure a) shows the 5 measurements taken for each time in the first experiment. Figure b) shows the mean values at each time for the triplicate experiment (numbered as 1, 2 and 3). Data is shown before ( $\square$ , dashed bars) and after ( $\bullet$ , solid line) applying the the correction given by Eq. 5.1. When the bar is not duplicated means that  $f_c = 1$  for the measured image and no filling correction is required. Error bars represent the standard deviation of the image.

TEST	C-24	C-48	C-72	24-72	48-72	24-72
W. rank sum	0.016	0.008	0.008	0.008	0.008	0.008
Kruskal-Wallis	0.016	0.009	0.009	0.009	0.009	0.009

Table 5.1 -  $p$ -values for each possible couple of sets of measurements of the first experiment ( $C$  is control) after the filling factor correction. Values with  $p < 0.01$  mean a high significance, values between  $0.01 < p < 0.05$  mean significant and values of  $p > 0.1$  are not significant.

Statistical analysis tells us that there is a significant difference between the population of untreated (control) and treated cells ( $p$ -values  $< 0.05$ ). This confirms that we are able to detect even low percentages of cell death. At longer times the correlation between cell death and diattenuation becomes stronger with  $p$ -values smaller than 0.01.

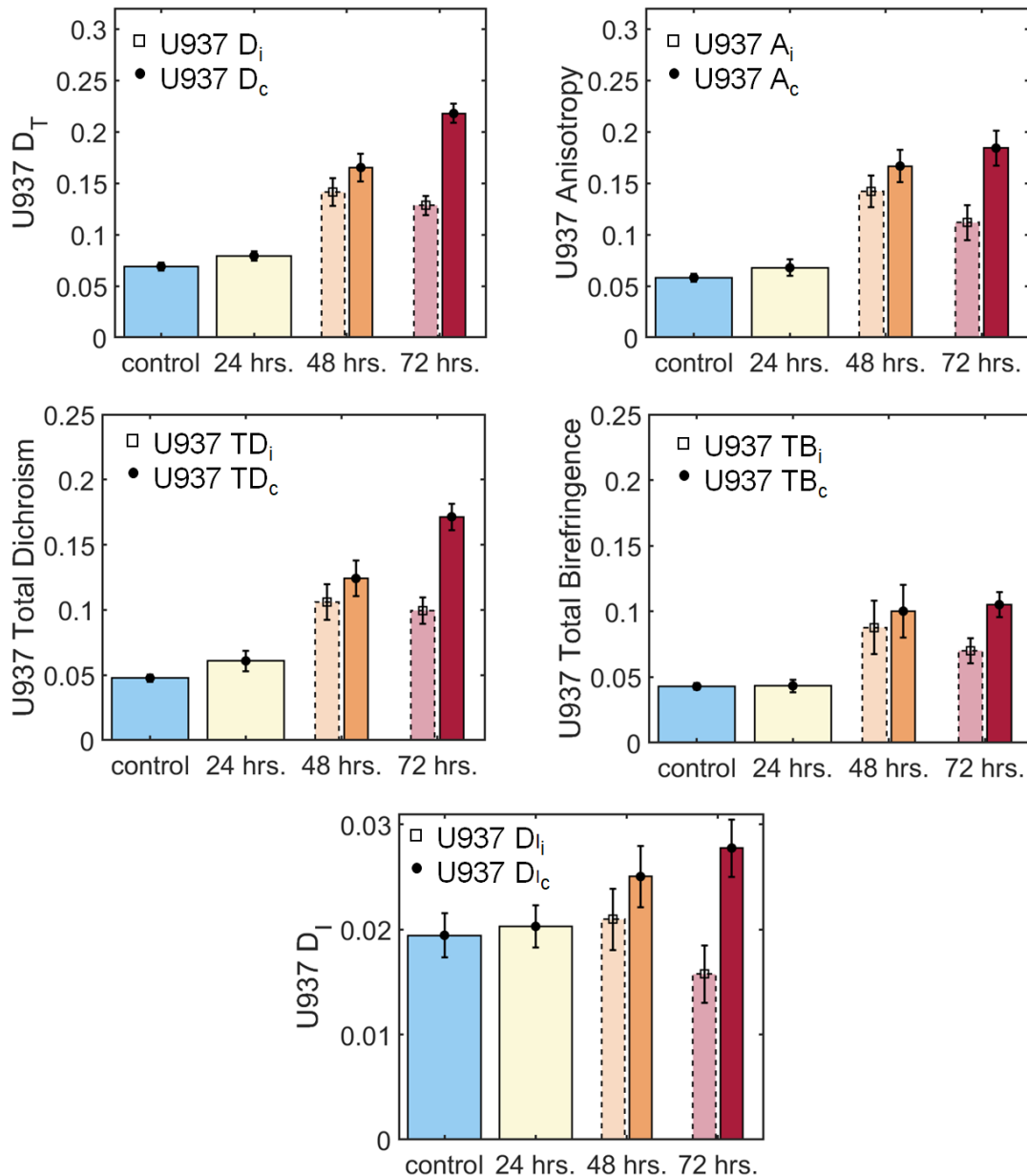


Figure 5.26 - Mean total diattenuation, anisotropy, total birefringence, total dichroism and depolarization index of the 5 measurements made at each time in the first experiment. Data is shown before ( $\square$ , dashed bars) and after ( $\bullet$ , solid line) applying the correction given by Eq. 5.1. When the bar is not duplicated means that  $f_c = 1$  for the measured image. Error bars represent the mean standard deviation of the 5 images of each parameter.

Other polarimetric parameters obtained from different decomposition methods show a similar variation over time. In the case of depolarization index we consider that the changes are relatively smaller and, therefore, less significant. Figure 5.26 shows the sequence corresponding to 5 polarimetric parameters (total diattenuation, anisotropy, total birefringence, total dichroism and depolarization index). Bars represent the mean values of all the pixels of the 5 images taken in each sample and error bars represent the deviation obtained from all pixels in all 5 images. All five parameters seem to be sensitive to the cell death and present a similar trend over time. We decided to focus on with diattenuation because it presents the lowest standard deviation. Once focused on diattenuation, we have done our experiment in triplicate. Results are shown in Figure 5.26b where mean values of diattenuation are presented for each experiment and for each time point.

In Figure 5.27 we represent the the mean values of diattenuation as a function of the mean value of the percentage of dead cells obtained from the triplicate experiment with U937 cells, since both increase over time. At 24 hrs., there is a slight increase in diattenuation that becomes very significant at 48 hrs. of treatment. By 72 hrs., the diattenuation slightly decreases with respect to the previous time point if data is not corrected by the filling factor, likely due to the loss of cell confluency as shown in Figure 5.19D which would decrease the mean value of the parameter measured. After correction we see that the diattenuation increases with the cell death quite linearly during the period analysed.

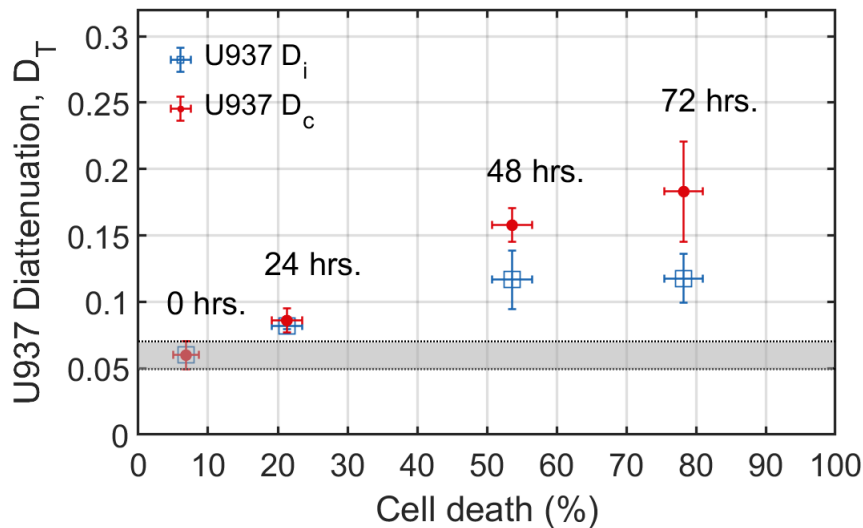


Figure 5.27 - Mean values of the diattenuation ( $D_T$ ) obtained from the triplicate experiment with U937 cells as a function of cell death. Values of the diattenuation directly obtained from the image ( $D_i$ ) and diattenuation from cells corrected by Equation 5.1 ( $D_c$ ) are represented with  $\square$  and  $\bullet$  respectively. Error bars represent the mean standard deviation of the 3 experiments.

This increase in  $D_T$  deserves special attention. In the first place, if linear and circular diattenuation are analysed separately, the same tendency is found, being linear slightly higher than circular. Attending to the spatial distribution of  $D_T$  in the image (see

Figure 5.28), it seems that the diattenuation enhancement associated with cell death and observed in U937 cells, is most likely the consequence of changes in the plasma membrane. The increase of  $D_T$  is observed at the edges of the cells, clearly outlining their contour. This is in agreement with the fact that plasma membranes suffer major changes during the apoptosis process including loss of phospholipid asymmetry. This phospholipid redistribution between the inner and outlet leaflets of the membrane generates interfacial forces able to modify the structure of transmembrane proteins [100], which could be detected by using circular dichroism, a well-known technique that has been employed for studying the structure, dynamics and interactions of proteins [101] in the UV domain. Another effect that may modify the value of diattenuation during cell death results from alterations in membrane tension due to modification of membrane-associated molecules and the intracellular and extracellular mechanical stimuli that change the membrane curvature [79]. Thus, we suggest that the increase of diattenuation signal could be related to changes in transmembrane protein structure and membrane geometry as cells undergo apoptosis.

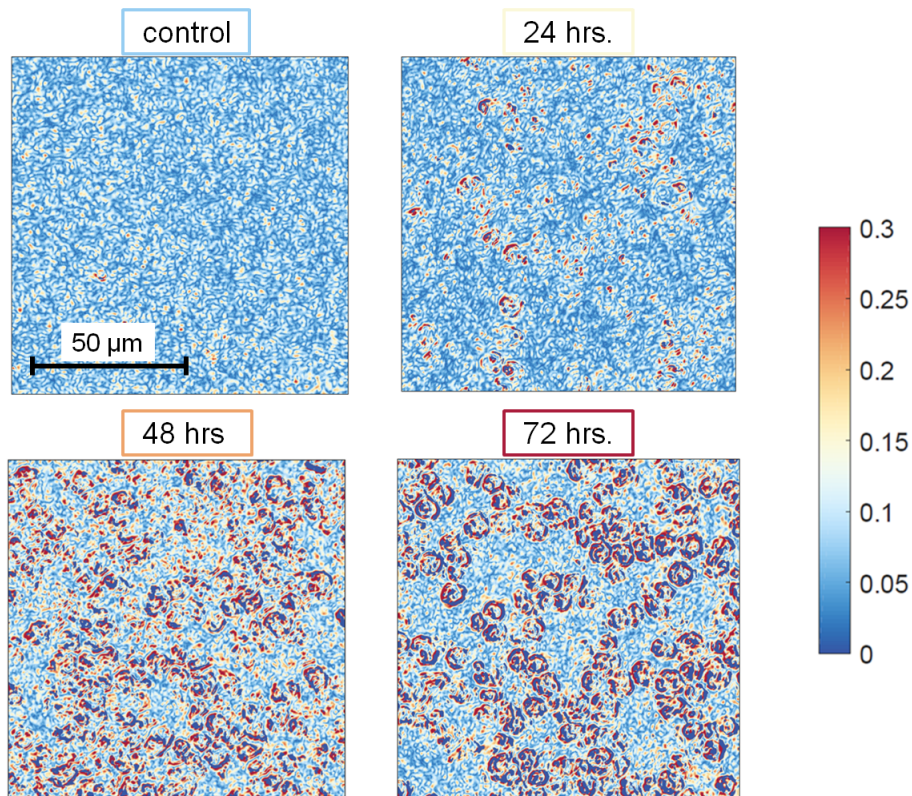


Figure 5.28 - Total diattenuation images ( $D_T$ ) of U937 cells at different times of the treatment with 20  $\mu\text{g/ml}$  of cisplatin.

### THP1 cell line

A similar result was obtained when another leukemia cell line, THP1, was treated with cisplatin. By 24 hrs. of treatment there is over 2-fold increase of cell death by trypan blue (Figure 5.29 left) that is confirmed by a reduction of metabolic activity (Figure 5.29 right). With the polarimetric analysis (Figure 5.30) we see a similar behaviour. As in the case of the U937 cell line, all parameters slightly (but

significantly) increase at 24 hrs. being an indication of cell death detection. The most significant increase occurs again in the diattenuation parameter.

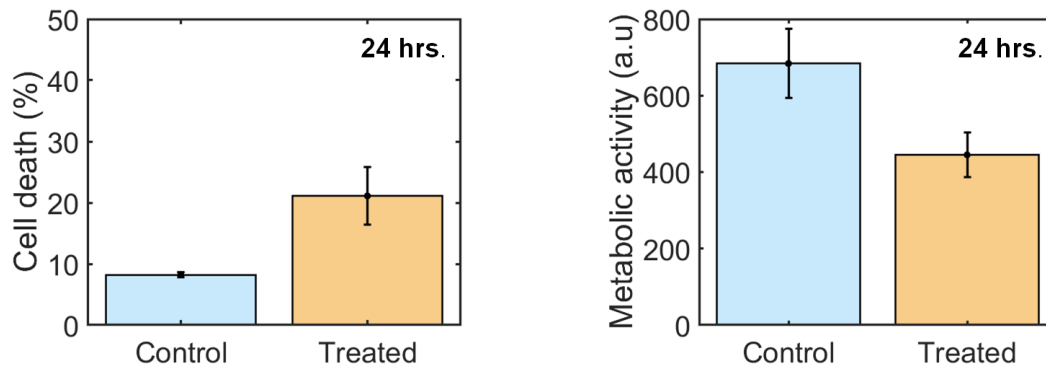


Figure 5.29 - Death of THP1 cells over time treated with 20  $\mu\text{g}/\text{ml}$  of cisplatin evaluated with trypan blue exclusion test (left). Metabolic activity of THP1 cells under the same treatment using the Alamar Blue assay. a.u., arbitrary units (right).

Again, the experiment has been done in triplicate. Results for diattenuation parameter as a function of cell death are shown in Figure 5.31. Trypan blue test shows a high dispersion in these results of cell death and the diattenuation increase is accordingly noisy.

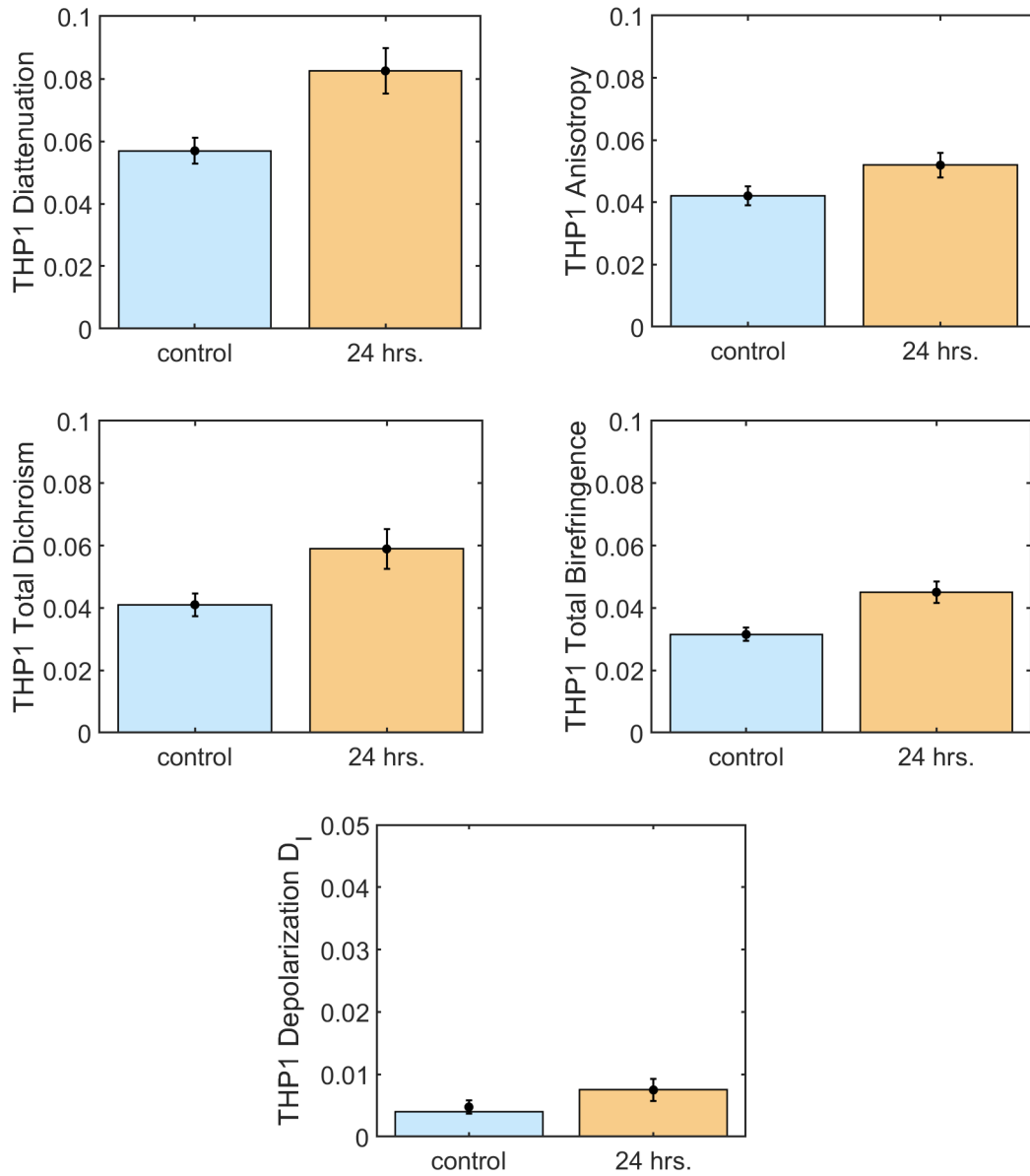


Figure 5.30 - Mean total diattenuation ( $D_T$ ), anisotropy ( $A$ ), total birefringence ( $TB$ ), total dichroism ( $TD$ ), depolarization index ( $D_I$ ) of the 5 measurements made for each sample of THP1. Error bars represent the mean standard deviation of the 5 images of each parameter.

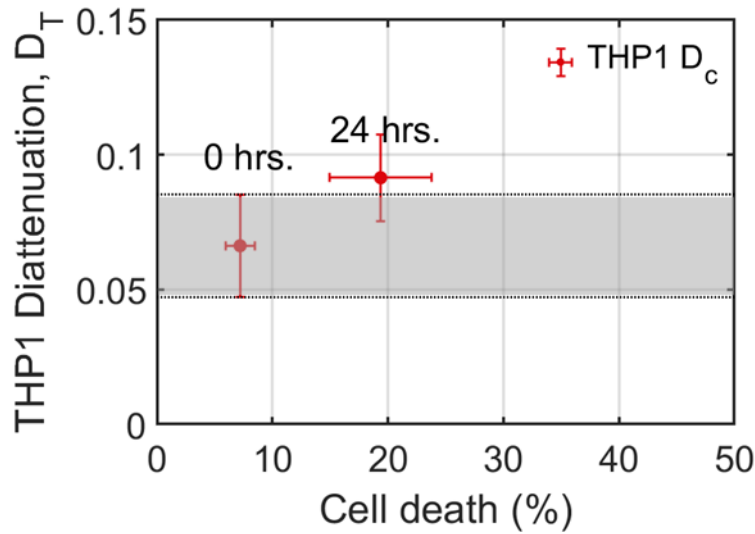


Figure 5.31 - Mean values of the diattenuation ( $D_T$ ) obtained from the triplicate experiment with THP1 cells as a function of the cell death. Error bar is the mean standard deviation of the diattenuation images over the three experiments.

## 5.6 Conclusions

We have worked with several cancer cell lines such as colorectal adenocarcinoma HT29 cell line, breast cancer MCF7 cell line and leukemia cell lines U937 and THP1. We have measured the image Mueller matrix, in transmission configuration, of samples of these cell lines and performed Polar Decomposition, Mueller Matrix Transformation and Differential Decomposition in order to reach some polarimetric parameters that could give us more insight into the role played by the cell, or by some cell components, in changing the polarization of the light that goes through it either in the living state or when it undergoes under apoptosis. We carried out several experiments that involves treating cells with various chemotherapy drugs at different concentrations and evaluate the results over time.

As expected, since living cells are mainly transparent with an index of refraction close to water [19], the resulting matrix is quite close to unity. The main deviations from the trivial values after a  $\mathbf{M}$  analysis, are found in the diattenuation  $D_T$  (after MMPD), anisotropy  $A$ , (MMT), total dichroism  $TD$  and total birefringence  $TB$  (MMDD).

A study of cell death has been performed, combining a traditional method with another one based on the measurement and analysis of the above mentioned polarimetric parameters. U937 and THP1 leukemia cells have been treated with a chemotherapy drug ( $20 \mu\text{g/ml}$  of cisplatin) in order to induce cell death. Observation under the microscope shows evidence of cell degradation, but its quantification is not a straightforward process. When performing the polarimetric analysis on U937 cells, a strong correlation between diattenuation and cell death is clearly observed, even at early times after treatment. In addition, we suggest that, since the diattenuation

signal is located in the edges of cells, the increasing of diattenuation could be related with changes in the plasma membrane geometry and in its protein structure as cells undergo apoptosis. Similar results are obtained for the THP1 cell line and other polarimetric parameters mentioned above.

It is worth mentioning that non-polarimetric images (element  $m_{11}$ ) also would allow to see differences, but this will require software of image analysis and data recognition such as deep-learning. This path could be very promising of course, but polarimetry offers a direct and robust way to parametrize and analyse the images.

We conclude that diattenuation could be an objective tool to detect cell death, and useful for assessing in vitro killing efficacy of drugs under development and the follow-up of leukemia patients undergoing therapy with cytotoxic agents. Although the type of cell death detected is likely to be apoptotic because cisplatin treatment induces apoptosis, further studies will reveal whether diattenuation is able to discriminate between the different types of cell death. Moreover, since this method can be easily implemented in a microscope, although further work is necessary, it could result in an objective (i.e. independent of the observer) polarimetric method of analysis, complementary to the traditional techniques used for cell death quantification.

# Chapter 6

## Droplet-particle on a substrate: Curvature and degree of adherence

### 6.1 Introduction

Cell adhesion [27] is an essential mechanism in cell communication and regulation. It is so closely connected with the normal functioning of a cell that it can be shown that normal and cancerous cells show different adhesion properties [76]. Cell adhesion is a biological process that includes cell-cell and cell-substrate interactions which enable cells to stay within a tissue or migrate out of a tissue. In cancer, this is exemplified by the epithelial to mesenchymal transition [77], [78]. Epithelial cancer cells are adhered to the surrounding cells and the extracellular matrix forming the tumor tissue. When an epithelial cancer cell acquires a mesenchymal phenotype, it loses the adhesion properties and migrates to a secondary place to form a metastatic tumor. Thus, in vitro characterization of the adhesion capacity of living tumor cells by imaging polarimetry may give key information on the presence of cells with the ability to migrate and invade other tissues without the need to use any time consuming and observer-dependent labelling method. The degree of adhesion of a cell affects its surface shape and therefore the way in which it transmits and scatters light. For a suspended isolated cell we can model its shape by considering a spheroid. On the other end, the totally adhered cell can be approximated by a spread layer, with a bump associated to its nucleus. However, the intermediate state of the partially adhered cell is not easy to characterize. In order to model the transition we need a shape that can vary its parameters depending on the degree of adhesion, and which optical response is accessible through calculation.

As we have seen before, working with cells is not so easy. We need some particular conditions of temperature and humidity in order to keep them alive so that experiments are quite limited by time. In the same way, as the cells are living organisms that may respond quite different to medium, repeatability of experiment is always going to be very difficult.

For these reasons, we decided to look for a simpler experimental approach. A system that somehow fits the shape and behaviour of a biological cell but, at the same time, shows enough stability as to work more easily with the samples and perform different

tests. In order to learn about the optical response of a cell we chose to work with a model consisting of spherical particles that progressively adapt their shape to get attached to a flat substrate (see Figure 6.1). The real version of the model is based on latex particles ( $10\ \mu\text{m}$  in size and refractive index of 1.59), whose spherical shape changes when they get heated and partially melted, adhering to a glass substrate. This process mimics, to some extent, the adhesion and further spreading of a cell or a soft spherical particle when it is deposited on a flat substrate. Moreover, the convex bump formed when a spherical particle gets in contact with a flat surface and melts, can be approximately described by a spherical cap of curvature that depends on the degree of adherence. Similar flattening techniques have been already used to create flat surfaces in spheres in a controlled way [102]. Spherical caps modelling has applications in a variety of areas. For example, and in relation with the biomedical field, this kind of geometry is related with the relaxation dynamics of fluid membranes [103], a process essential to cell function. Other applications involve monitoring nanobubbles in minerals [104], studying the migration of small droplets over surfaces [105] or modelling the dynamics of diluted gas bubbles adhered to flat surfaces [106]. Regarding the study of contact angles of drops on surfaces [107],[108], polarimetry combined with the spherical caps modelling could also offer new experimental possibilities.

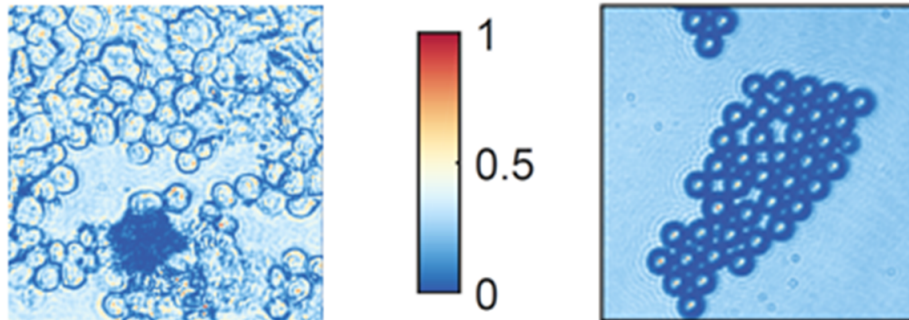


Figure 6.1 - Images of biological cells adhered to a microscope slide (left) and latex spheres of  $10\ \mu\text{m}$  diameter deposited on a glass substrate (right). Scale is the same for both images.

## 6.2 Experimental setup

### 6.2.1 Sample preparation and AFM measurements

The samples used in these experiments are made from latex micro spheres (diameter  $10\ \mu\text{m}$ ) in aqueous suspension (Sigma Aldrich 72986-5ML-F). The suspension is conveniently diluted using distilled water and then a controlled volume is deposited on a clean glass slide and let to dry in a clean atmosphere. In the process the spheres become adhered to the substrate due to electrostatic van der Waals forces. For this relatively large particle size formation of particle aggregates is mostly avoided with this procedure due to their relatively large size. The glass substrate, with the spheres adhered on it, is placed on a temperature controlled hotplate (Digital Hotplate Magnetic Stirrer H3760, Sigma Aldrich) at a temperature  $T = 200^\circ\text{C}$ .

Samples are left in the hotplate during increasingly longer times (from 30 seconds to 2 minutes) so different degrees of melting are achieved (Figure 6.2 above). Figure 6.3 shows the profile of three melted latex spheres, each one at a different stage of melting. Because of the partial melting, particles get flat at the bottom, and tend to keep a spherical curvature at the top, therefore producing something very close to a spherical cap. In this way, the progressive spread of the particle produces an increase of its geometrical cross-section (apparent size, see Figure 6.3). Comparison between a calculated spherical cap and the AFM (Atomic Force Microscopy) measurements of a partially melted sample shows good matching (Figure 6.2 below).

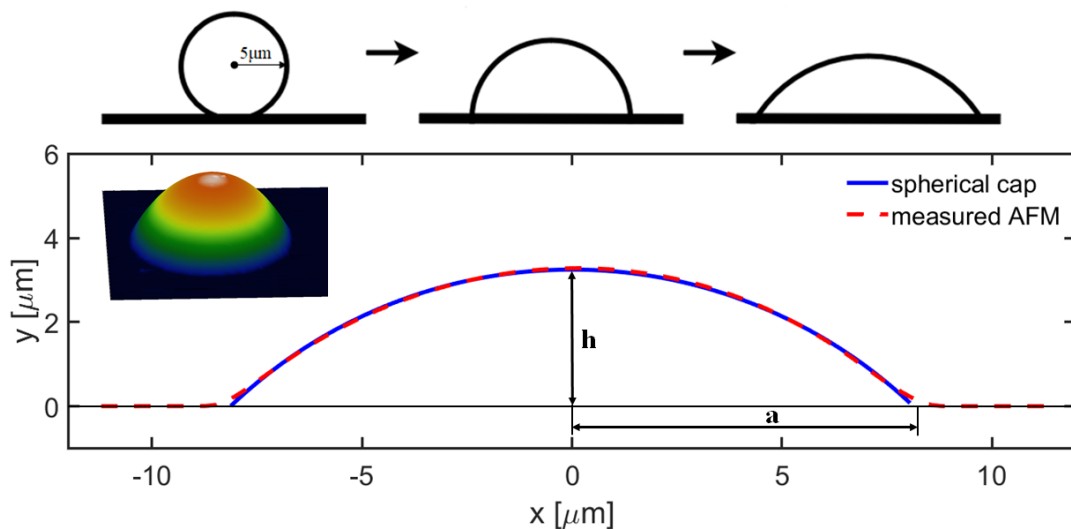


Figure 6.2 - Schematics of the melting process of a latex sphere on a glass substrate (above). Profile of a melted sphere (dashed red line) ( $a_m = 8.6 \mu\text{m}$ ,  $h_m = 3.3 \mu\text{m}$ .) compared to the profile of a spherical cap (blue) that produces the best fit. The inset shows the AFM measurement of a partially melted sphere.

In summary, this type of samples are easy to prepare and handle, and also very stable, which allows measurements to be made over long periods of time. Because of its transparency, size and refractive index, they are quite appropriate to model the behaviour of biological cells. Finally, the geometrical effect produced by the different stages of melting shows a good similarity with that of cell adherence [76].

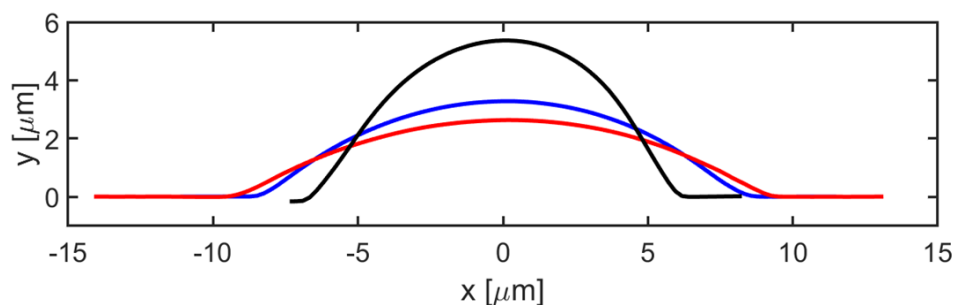


Figure 6.3 - Experimental AFP measurement of the profile of three latex particles corresponding to different melting stages.

## 6.2.2 Polarimetric microscope (LPICM)

In this section we present a polarimetric microscope recently developed and installed at LPICM (Laboratoire de Physique des Interfaces et des Couches Minces), an instrument to characterize the samples discussed in the present chapter. A complete description of the system with some application examples can be found in reference [89]. Figure 6.4 shows a schematic illustration of the polarimetric microscope. The system uses a white LED source emitting light in the 430 to 700 nm wavelength range. The introduction of a spectral filter just after the source allows selecting the working wavelength, 533 nm with a full width half maximum of 30 nm for the measurements discussed here. The microscope is mounted in transmission configuration with the sample being located between two identical microscope objectives (one for detection and another for illumination playing the role of a condenser). In this study two polarization preserving objectives (Nikon MUE1050) with a magnification  $\times 50$  and focal length of 4mm, providing a field of view of  $300 \mu\text{m}$  were used.

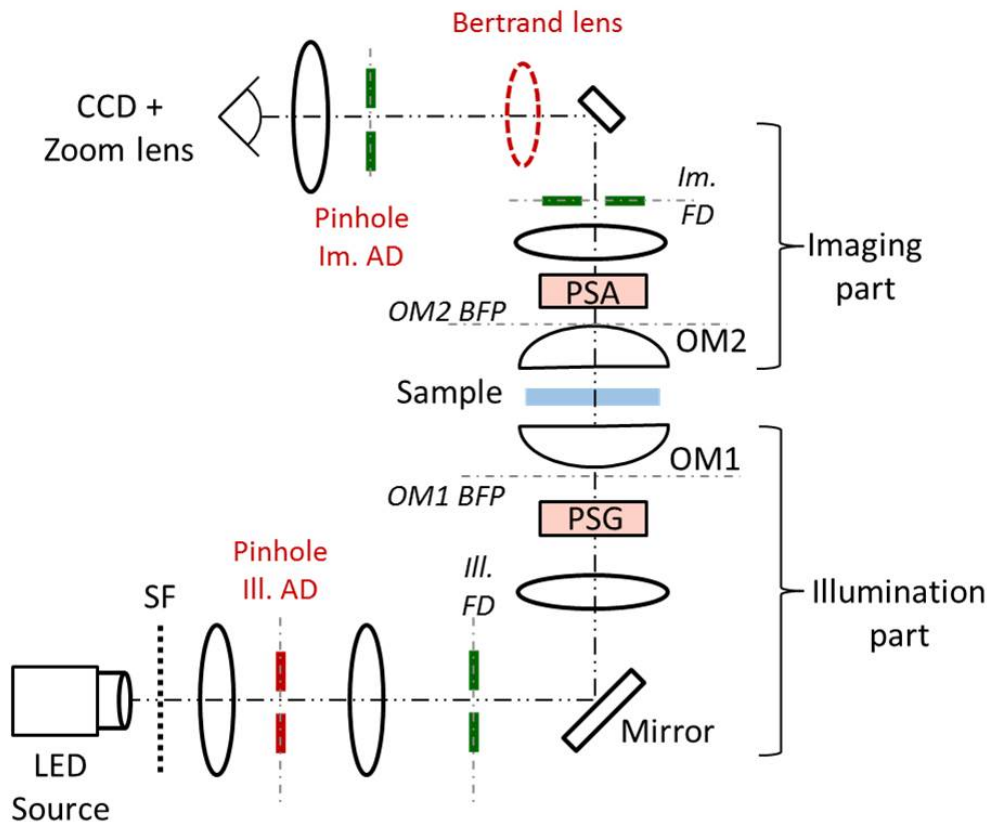


Figure 6.4 - Schematic illustration of the multimodal imaging polarimetric microscope in transmission configuration. The position of the PSG, the PSA, the illumination (OM1) and the imaging (OM2) objectives are shown. The other acronyms refer to the spectral filter (SF), the illumination aperture diaphragm (Ill. AD), the illumination field diaphragm (Ill. FD), the imaging aperture diaphragm (Im. AD), and the imaging field diaphragm (Im. FD). The position of the back focal planes of the illumination (OM1 BFP) and imaging objectives (OM2 BFP) are also shown.

A series of relay lenses, allows for the generation of four conjugate planes. Two of the planes, located in the illumination arm, are conjugated to the back-focal plane of the illumination objective and to the sample (object plane) respectively. In the illumination arm, a pinhole placed in the plane conjugate to the back focal plane of the objective acts as the aperture diaphragm and allows the control of the divergence and the direction of light illuminating the sample. In our case, the use of a pinhole of 500  $\mu\text{m}$  diameter produced a beam with  $7.1^\circ$  divergence with an average angle of incidence of  $0^\circ$  (normal incidence). A pinhole placed in the plane conjugate to the object acts as the field diaphragm, and can be used to define the size of the spot illuminating the sample. For the present study no pinhole was used. The two conjugate planes in the imaging arm are analogous to the ones in the illumination one and they allow placing both an aperture and a field diaphragm to control the aperture of the imaging beam and the size of the observed sample if needed. For the present study no diaphragm has been used in these two planes. A Bertrand lens can be optionally inserted in the optical path. By doing so, the Bertrand lens creates an image of the back focal plane of the imaging microscope objective in the CCD camera. The use of the Bertrand lens allows switching between real and Fourier imaging modes. In real imaging mode, the microscope produces images of the sample, whereas in Fourier mode, the camera registers the angular distribution of light scattered / transmitted by the sample. All images in this study correspond to real space.

The control of polarization is done with a polarization state generator (PSG) and polarization state analyser (PSA), which are respectively placed just before and just after the illumination and imaging microscope objectives. The PSG is composed of a linear polarizer, and two ferroelectric liquid crystal devices providing a quarter-wave and half-wave retardation respectively. The PSA is identical to the PSG but with the optical elements mounted in reverse order. The PSG generates four independent polarization states which correspond to the four possible combinations that can be produced by modifying the orientation of the FLCs. Each polarization state created by the PSG can be represented by a four-dimensional Stokes vector, and in turn, the four vectors corresponding to the four states created by the PSG can be grouped in a  $4 \times 4$  polarization matrix  $\mathbf{W}$ . The PSA analyses the polarization state of the output light from the sample, and in analogy with the PSG, the effect of PSA can be represented as a  $4 \times 4$  analysis matrix  $\mathbf{A}$ . Matrices  $\mathbf{A}$  and  $\mathbf{W}$  are determined during the calibration of the instrument. The CCD camera detects 16 images which correspond, each one, to a particular polarization state generated by the PSG and to a particular analysis projection by the PSA. The 16 images can be grouped in an intensity matrix  $\mathbf{B}$ . The intensity matrix and the Mueller matrix of the sample,  $\mathbf{M}$ , are related to the matrices  $\mathbf{A}$  and  $\mathbf{W}$  by the following expression  $\mathbf{B} = \mathbf{AMW}$ . More details about the use of matrices  $\mathbf{A}$ ,  $\mathbf{W}$  and  $\mathbf{B}$  can be found in the following references [109]. The multimodal imaging Mueller polarimetric microscope is calibrated according to the “eigenvalue calibration method” [110]. The eigenvalue calibration method is a very versatile procedure applicable to a wide range of polarimeters whatever they are imaging or non-imaging.

### 6.3 Polarization model for normal incidence imaging

Simulating ray tracing through spheres is not something new, [111–113], but we propose here a simple, though accurate, description of polarimetric image formation for forward observation (back illumination) at normal incidence.

The initial geometry (Figure 6.5) consists of a sphere of radius  $r$  on a homogeneous substrate illuminated by a homogeneous light beam at normal incidence. This configuration is representative of experiments working at low  $NA$  illumination in transmission microscopy. For spheres on substrates we may have either direct illumination, i.e, first impinging the particle and then the substrate, or reversely, illumination through the substrate. For the sake of consistency with our experiment, the illumination in our analysis is done through the substrate and, for normal incidence, the effect of this substrate on the direction of rays can be initially ignored. (Note that, in the case of melted spheres, for which the particle will be modelled by a spherical cap with the same volume as the original sphere, the first dioptré, the substrate-particle one, will be reached at normal incidence). For each initial incident ray, we follow the trajectory of the refracted, reflected and transmitted rays, applying Fresnel coefficients [114] to each component and keeping track of the optical path.

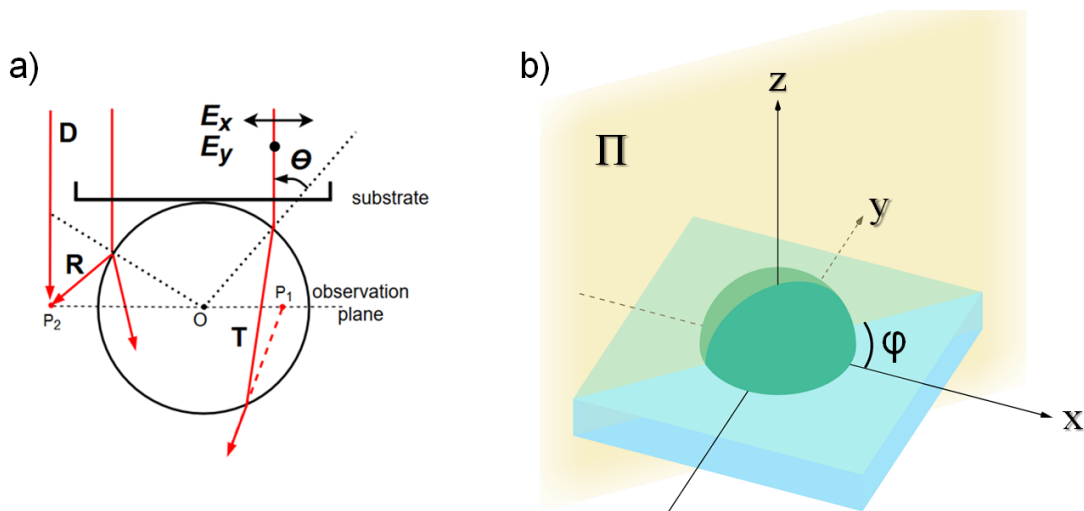


Figure 6.5 - a) Description of rays travelling inside a meridian plane and the cartesian components of the incident electric field.  $R$ : reflected rays will interfere with direct rays ( $D$ ) travelling outside the sphere.  $T$ : transmitted rays (the virtual path required to reach the observation plane is shown as a dashed line). b) Meridian plane  $\Pi$  corresponding to a given azimuth  $\varphi$ .

The image is obtained by coherent addition of rays coming from each point of the observation plane. Only rays with  $NA$  smaller than a certain value (given by the experiment that we want our calculations to be compared to) are considered. Note also the importance of the election of the observation plane on the calculation, a point that will be addressed later on.

For our calculations, we take advantage of the symmetry of the system for normal incidence and operate always in a meridian plane  $\Pi$ , varying the azimuthal angle  $\varphi$  (see Figure 6.5b). (This meridian plane is the local plane of incidence that determines the field components associated to any incident polarization).

The calculation requires the knowledge of the radius  $R$  of the sphere, the refractive index  $n$  of the particle, and also that of the surrounding medium. In what follows, the calculation process is described in more detail.

First, the incident beam is discretized in an homogeneous grid of rays, sampling the XY plane over the particle (though not limited to its cross-section). For every incident ray impinging the particle at the point of coordinates  $(x_0, y_0, z_0)$  there is a local angle of incidence,  $\theta_i$ . After this it will remain in the meridional plane for the rest of the possible trajectories. The program keeps track of each transmitted and reflected ray through the different surfaces, applying the corresponding Fresnel coefficients,  $t_{\perp}, t_{\parallel}, r_{\perp}$  and  $r_{\parallel}$  for the transmitted and reflected beams, respectively, and recording the optical paths. In order to calculate the Mueller matrix of the sample, we need to evaluate just two incident polarizations: a linear polarization arbitrarily oriented and another one orthogonal to the first. (The reason is that there is no depolarization mechanism implicit in our calculation of the matrix. Therefore, the Mueller matrix will be pure, and it can be obtained from a primary Jones matrix). In our case, we have chosen the same  $x$  and  $y$  defined previously. The Jones vectors, that describes the electric field of a polarized beam, are equal to  $E_x = [1 \ 0]$  and  $E_y = [0 \ 1]$  respectively. The Jones matrix, given by Eq. 6.1, describes the characteristic response of a non-depolarizing system.

$$J' = TJ \quad \begin{bmatrix} E'_1 \\ E'_2 \end{bmatrix} = \begin{bmatrix} j_{11} & j_{12} \\ j_{21} & j_{22} \end{bmatrix} \begin{bmatrix} E_1 \\ E_2 \end{bmatrix} \quad (6.1)$$

Also, to work more easily and taking advantage again of the symmetry of the problem, we can change the coordinates system to work in SP coordinates [115]:

$$\begin{bmatrix} E_{\parallel} \\ E_{\perp} \end{bmatrix} = \begin{bmatrix} \cos(\varphi) & \sin(\varphi) \\ -\sin(\varphi) & \cos(\varphi) \end{bmatrix} \begin{bmatrix} E_x \\ E_y \end{bmatrix} \quad (6.2)$$

$$\begin{bmatrix} E_x \\ E_y \end{bmatrix} = \begin{bmatrix} \cos(\varphi) & -\sin(\varphi) \\ \sin(\varphi) & \cos(\varphi) \end{bmatrix} \begin{bmatrix} E_{\parallel} \\ E_{\perp} \end{bmatrix} \quad (6.3)$$

This transformation allows to work with the matrix in a polar representation that is not sensitive to the election of the X and Y axis. Then, we can obtain the M associated to a Jones matrix, by using the set of equations 3.24.

This Mueller matrix has to be of the pure kind [1] and it has only 8 independent coefficients, (the number corresponding to the variable of the complex elements of the 2x2 Jones matrix). Experimental matrices always have some degree of depolarization,

something that we need to remember when making theory-experiment comparisons.

An important point still to be described is the choice of the observation plane. From the experimental point of view, this corresponds to "focusing on the sample", an action that, quite often, is not as simple as expected. For a melted sphere we should use the common reference for focussing: the flat substrate itself, where some submicrometric impurities can be found, that are helpful for the purpose. For the non-melted sphere, however, the natural criterion is based on "sharpness", presuming that it corresponds to the equatorial plane. As for the calculation, however, we can be certain of the correspondence between the image and a given observation plane. Let us remind that the image is reconstructed by coherently adding the rays coming from each point in the observation plane, up to some value of the  $NA$ . By selecting different observation planes we can mimic the experimental action of focusing.

## 6.4 Results

### 6.4.1 Mueller matrix of spheres and spherical caps

For an isolated latex sphere ( $n \approx 1.59$ ,  $r = 5\mu\text{m}$ ) on a flat transparent substrate, the transmission Mueller matrix has been measured and calculated (see Figure 6.6). The chosen focussing plane was the equatorial plane of the sphere and the x-y axes in this representation correspond to the main directions of the PSG and PSA systems. This figure is obtained for collimated illumination at  $\lambda = 533\text{ nm}$  and for a collection aperture of  $37^\circ$  ( $NA = 0.6$ ), which is the strict value for the experiment. Matrix elements are normalized to  $m_{11}$  and two different color scales have been used (diagonal and off-diagonal) for the sake of clarity. An external ring is distinctly observed with values for the sign and number of divisions that vary from one element to another. Black/white dashed lines show the actual size of the sphere, according to the magnification of the system.

As can be seen, all the structures appearing in most of the matrix elements are reproduced. The origin of such rings can be easily identified in the calculation as being produced by the coherent sum of the direct and grazing reflectance in the sphere surface. This interference pattern extends outside the sphere to an extent that depends on the  $NA$  of the observation, so that more intensity oscillations should be expected for higher  $NA$  values.

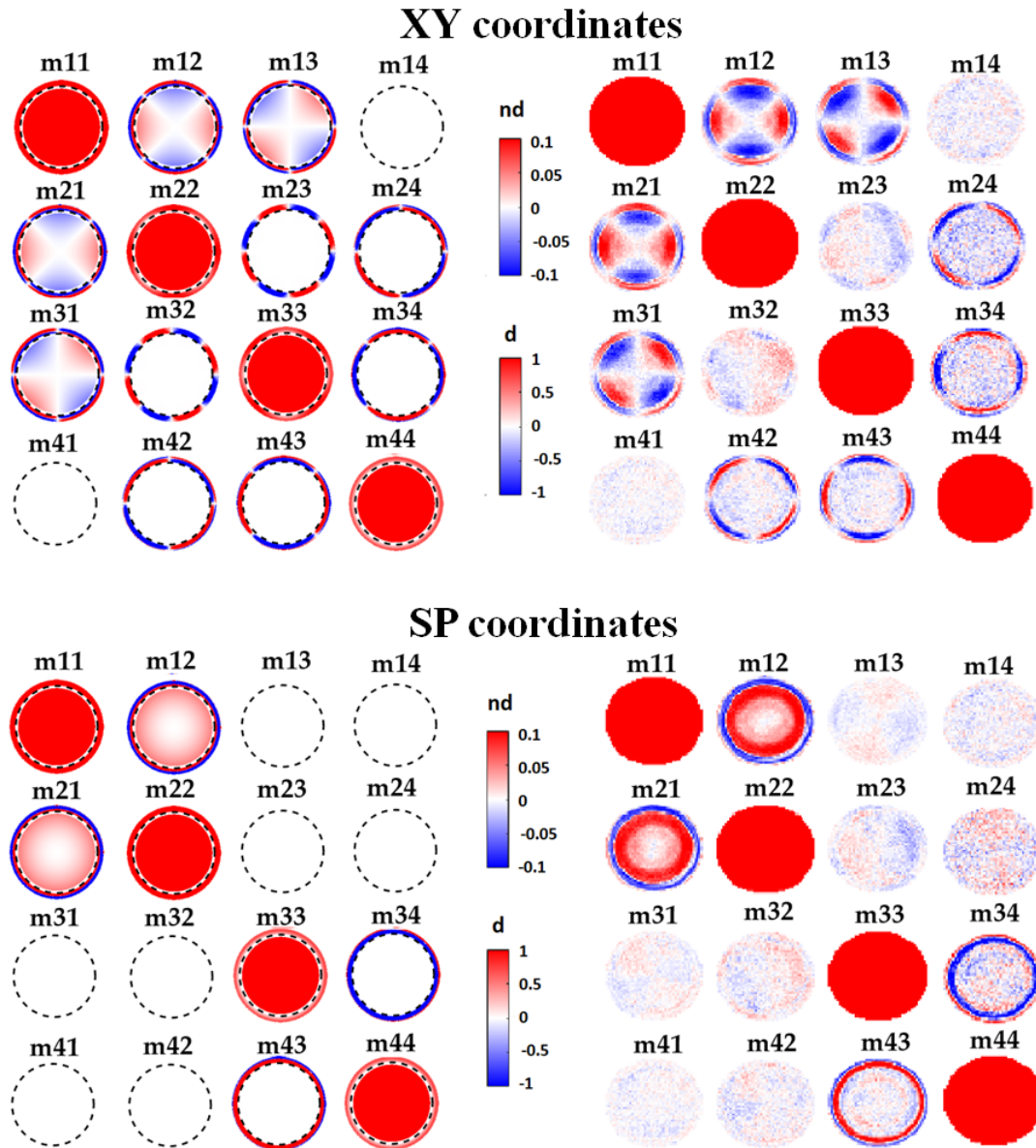


Figure 6.6 - Comparison between experimental (right) and calculated (left) Mueller matrix of a latex sphere of radius  $5 \mu\text{m}$  through coherent polarization-sensitive ray tracing simulation for equatorial focusing in XY (above) and SP coordinates (below). Two color scales are shown for diagonal ( $d$ ) and non-diagonal ( $nd$ ) elements. Black dashed line shows the actual boundary of the sphere ( $r = 5 \mu\text{m}$ ).

Because of the circular symmetry of this system, it is very convenient to change to polar coordinates. In this way, we can avoid the rather complex azimuthal dependence, as observed, for instance, in the crossed patterns in elements  $m_{12}$  and  $m_{21}$  or the rotated cross in elements  $m_{13}$  and  $m_{31}$ . These patterns indicate that the resulting polarization of the light after interaction with the particles is not aligned with the lab axes but rather to the meridian plane. This change to SP coordinates requires just the selection of a centroid and the standard operations described in Section 2. For systems with circular symmetry, 8 elements of the matrix become zero and the information is contained in the  $2 \times 2$  boxes on the main diagonal. In

other words, no cross-polarization mechanism is present when light is described in terms of circular components. Figure 6.6 (below) shows the calculated (left) and experimental (right) Mueller matrices of a sphere in SP coordinates. The values of the off-diagonal elements are close to zero, showing the obvious circular symmetry of the particles and good choice of the centroid. In general, noise can account for the discrepancies observed.

By applying heat we achieved samples with different degrees of melting. As a representative case of a melted sphere, in Figure 6.7 we show the experimental measurement of a melted sphere (right), labelled as *melt1*, and the calculated matrix for a spherical cap of the same volume as the original sphere and curvature radius of  $7.2 \mu\text{m}$ . In these conditions the radius of the contact circle, apparent radius under the microscope, is  $a = 7.0 \mu\text{m}$ . Observation conditions are as in Figure 6.6, except for the observation plane, now fixed at the substrate surface. The spreading of the sphere, as compared to the original radius of  $5 \mu\text{m}$  -indicated by the black/white dashed line- is clearly observed.

Again, the main features of the experimental matrix are reproduced by the calculations, including the presence of a faint ring in some elements. The main differences with respect to a complete sphere are related, obviously, to the apparent size, but also to the reduction of the ring, that becomes invisible for further melting stages, a fact that will be discussed later on.

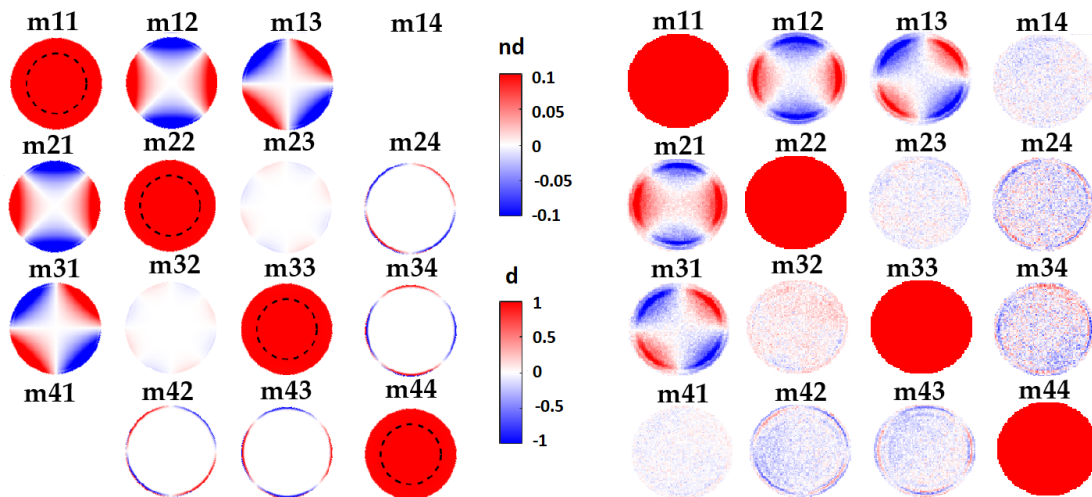


Figure 6.7 - Experimental Mueller matrix of a latex melted sphere in  $x$ - $y$  coordinates (right) and the Mueller matrix obtained through ray tracing simulation for substrate focusing and for the same volume than the sphere shown in the left. Curvature radius  $r = 7.2 \mu\text{m}$  (left) in  $XY$  coordinates. The colorbar scale is shown for diagonal elements ( $d$ ) and for non-diagonal elements ( $nd$ ). For reference, black dashed lines shows the size of the original sphere ( $r = 5 \mu\text{m}$ ).

#### 6.4.2 Adherence and matrix transformation parameters

As described in Chapter 3.4, we have applied the equations for Mueller matrix Differential Decomposition and obtained a set of polarimetric parameters for the

set of samples studied. The subsequent analysis suggests that, for transmission observation, there are two parameters of interest to characterize the adherence of the sphere to the surface (or degree of melting): dichroism and birefringence. In particular, in Figure 6.8 we can observe that the most relevant parameters, sensitive to the geometry are linear dichroism ( $LD$ ) and linear birefringence ( $LB$ ).

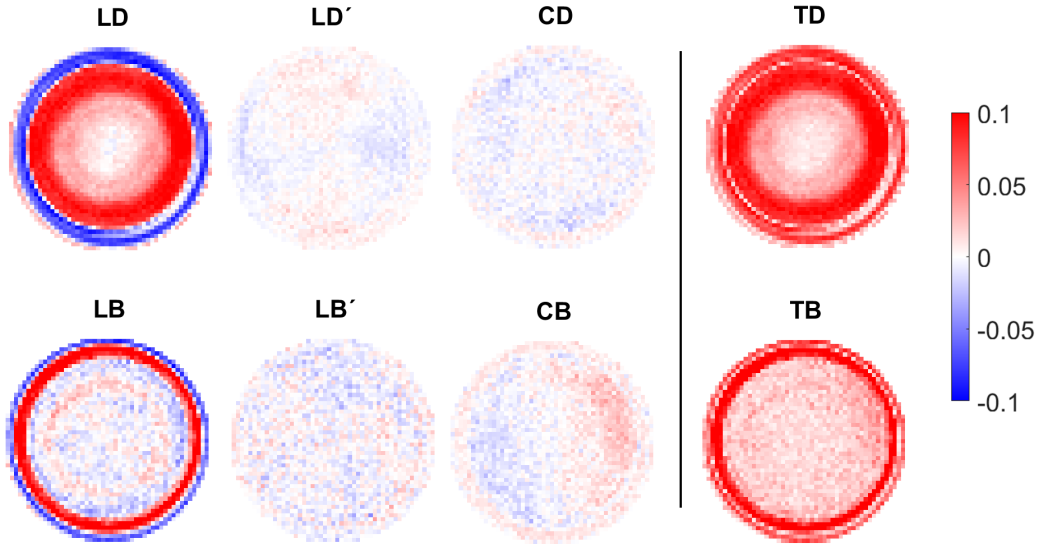


Figure 6.8 - Experimental measurements of dichroism and birefringence in SP coordinates for a latex sphere ( $r = 5 \mu\text{m}$ ).  $LD$  is linear dichroism in  $x$ - $y$  direction,  $LD'$  is linear dichroism in  $45^\circ$  direction,  $CD$  is circular dichroism and  $TD$  is total dichroism. Similar label criterion is used for birefringence.

We prepared 4 different samples by depositing latex spheres on a microscope glass slide. One of the samples was directly measured, acting as a reference case (complete sphere,  $r = 5 \mu\text{m}$ ). The remaining three samples were heated during increasingly longer times, reaching variable melting states, from the shortest heating time (or sample *melt1* whose  $\mathbf{M}$  has been previously shown) to the longest heating time (sample *melt3*).

By applying Eq. 3.51 and 3.54 to the experimental matrices, we obtained the linear dichroism magnitudes  $LD$  and  $LD'$  (referred, respectively, to axis  $XY$  and the  $45^\circ$  rotation ones, that depend on elements of the first row of the differential Mueller matrix  $m'_{12}$  and  $m'_{13}$ ), and the linear birefringence  $LB$  and  $LB'$  (that depend on elements from the fourth column  $m'_{42}$  and  $m'_{43}$ ). A combination of this magnitudes (Equations 3.57 and 3.58) gives, respectively, the total linear dichroism (TLD) and total linear birefringence (TLB), represented in Figure 6.9 for the four cases under study, once the SP transformation has been applied. For each case we present the images of both parameters together with their cross-section (for which an azimuthal average has been performed). Both parameters seem to be quite sensitive to the curvature, although in a different way: while the birefringence peaks seems very sensitive to the early state of adherence, decaying soon to values close to the noise, the peaks of the linear dichroism decay gradually, with the curvature.

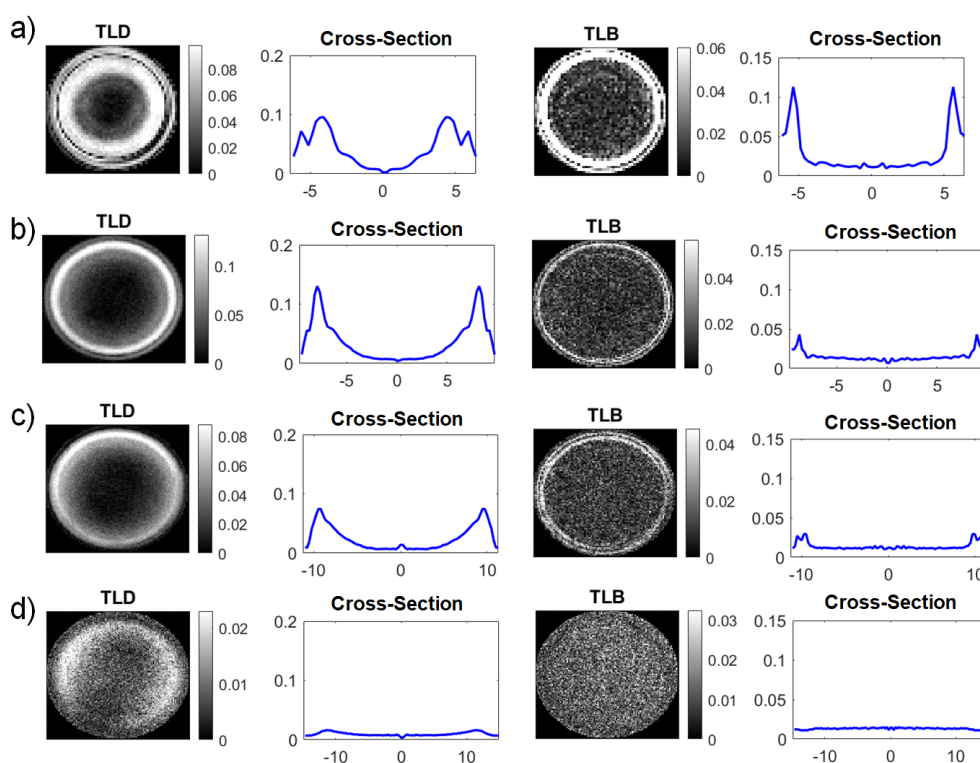


Figure 6.9 - Experimental results in SP coordinates for total linear dichroism (TLD) and total linear birefringence (TLB) of (a) a complete sphere, and (b-d) increasingly melted spheres (melt1, melt2 and melt3). Blue lines represent the azimuthal average of the cross-section.

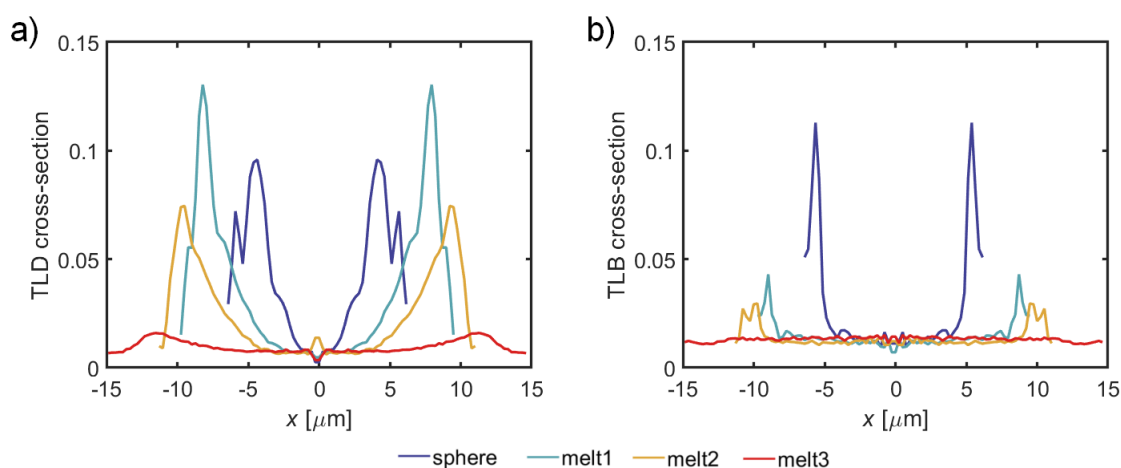


Figure 6.10 - a) Evolution of the azimuthal average of the cross section of total linear dichroism, TLD, with the increase of the melting degree, b) The same for total linear birefringence, TLB.

The presence of a sharp peak in the vicinity of the boundary is a promising feature for the purpose of characterizing the adherence, as seen in Figure 6.10, where cross-sections are represented in the same scale. Although observed in both *TLD* and *TLB*, the peak dependence is more notorious for the dichroism, as shown in Figure

6.11a where the maxima (taking the relative values with respect to the background of the signal) are plot against the apparent size.

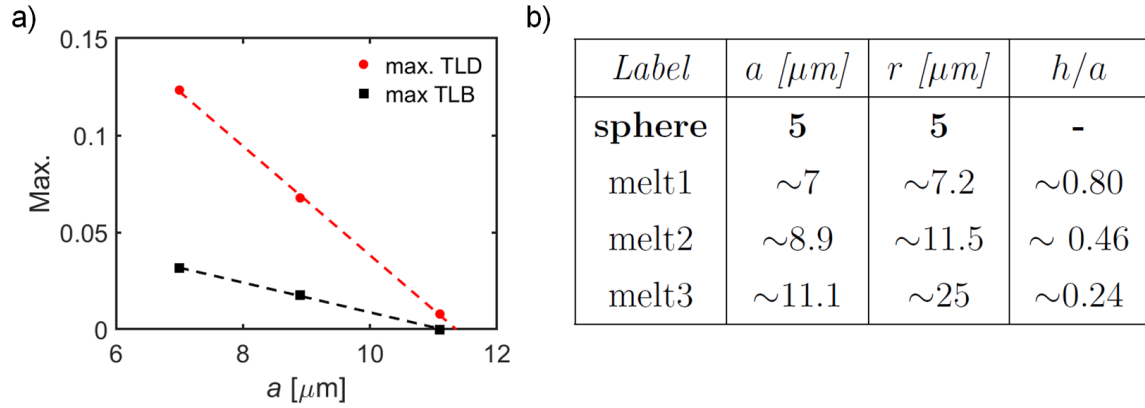


Figure 6.11 - a) Evolution of the maxima of the cross-sections for TLD and TLB with the apparent radius  $a$ . b) Table with the apparent traversal radius,  $a$ , and the associated values for the radius of curvature of the spherical cap,  $r$ , and the relative height of the cap, or aspect ratio,  $h/a$ .

In order to analyse the spreading effect, we have focused on the element  $m_{12}$  (or  $m_{21}$ ), which is related to the linear dichroism. In Figure 6.12, the experimental cross-section of this element is compared to the calculated one for the four samples under analysis. The values of  $a$  that produce the best match are listed in the second column of Figure 6.11b. The rest of the values of such table are obtained accordingly, assuming a constant volume of the melting particle. Although the general profile of  $m_{12}$  is reproduced for each case, and the same sequence of maxima is obtained, the exact values for the peaks differ notably. The reason for this "softening" of the experimental patterns may lay in the fact that illumination is modelled as a perfectly collimated beam, while in the experiment an integration over a few degrees is actually performed. The averaging effect introduced in this way may be responsible for the softening of the patterns.

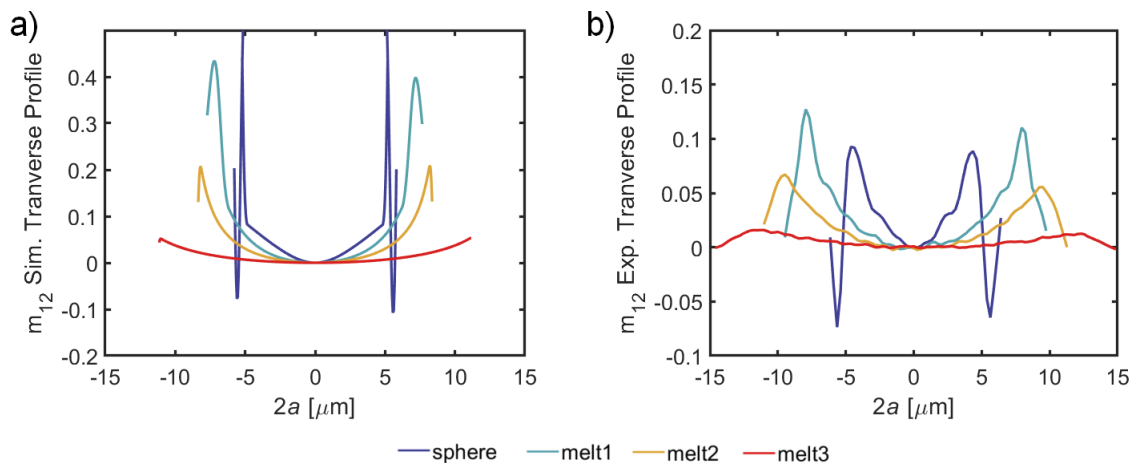
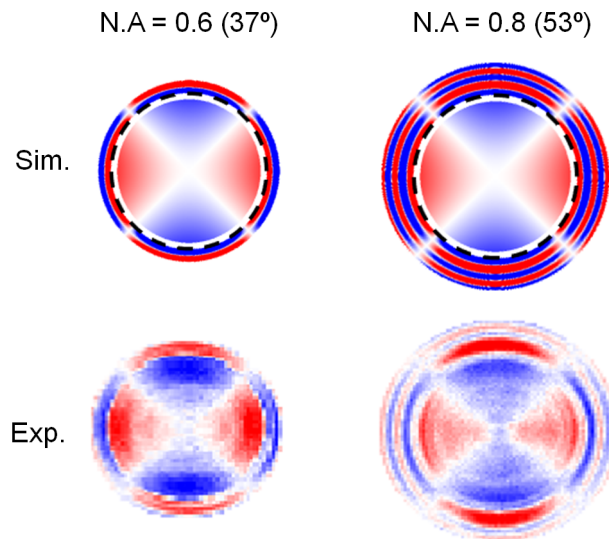


Figure 6.12 - Comparative between experimental cross-sections of element  $m_{12}$  of the four samples (b) and the ones simulated with the radii estimated in Figure 6.11b (a).

### 6.4.3 Influence of the numerical aperture

As it has been already mentioned, an important feature observed in the polarimetric images of these systems is the presence of a ring in the limiting region of the sphere or cap. This ring originates from the coherent interference between direct rays passing through the substrate and rays reflected on the surface of the sphere. There are two factors determining the appearance -and number- of these rings: the shape of the particle and the numerical aperture ( $NA$ ) of the system. As for the shape, if we assume that the spherical profile is preserved, the key magnitude is the angle formed by the particle boundary and the substrate. In other words, it is directly related to the adhesion (i.e. degree of melting in the experiment). As for the  $NA$ , by increasing the collection angle we naturally extend the region around the particle where beam overlapping -and therefore interference- can be detected.

Figure 6.13 shows an example of how the  $NA$  affects the number of visible rings for a sphere. The experimental values of  $NA$  (0.6 and 0.8) have been implemented in the model producing a good match and explaining the increase in the number of rings.



*Figure 6.13 - Influence of the numerical aperture in the number of visible rings. Experimental measurements of element  $m_{12}$  of the Muller matrix of a  $r = 5 \mu\text{m}$  sphere (below) compared to simulation (above) for two values of the  $NA$ .*

This predictable behaviour of the observable rings suggests an interesting procedure in a setup with variable  $NA$ . Figure 6.14 shows the  $NA$  at which, according to the model, the first ring becomes visible when the  $NA$  increases, as a function of the ratio ( $h/a$ ) of the caps. Inversely, for a fixed  $NA$  and increasing value of ( $h/a$ ), like in a detachment process, the ring should appear at some predictable value of the aspect ratio. In this way, this feature can work as an aspect-ratio assessment tool, provided that the assumption of a spherical cap is good enough. This is exemplified in Figure 6.14 with two observations at  $NA = 0.6$  and  $h/a = 0.5$  and  $0.8$ . No ring is observed for the first one, while the second, located on the transition, shows an incipient ring.

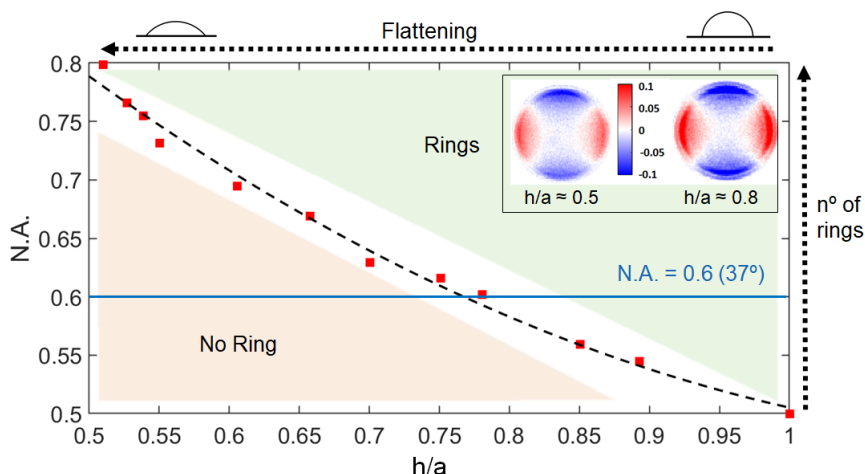


Figure 6.14 - Numerical aperture at which the first interferential ring becomes visible as a function of the melting degree ( $h/a$ ) of the particle. Calculation is made for individual cases of  $h/a$  (red squares), and the black dashed line is a second order polynomial fit. The inset shows two experimental measurements of element  $m_{12}$  for a  $NA = 0.6$  (horizontal blue line) and two different melting degrees of the particles.

## 6.5 Analysis and conclusions

We have developed a simple model to simulate the transmission Mueller matrix of spheres and spherical caps located on a transparent substrate by calculating the image produced after tracing a collimated beam and coherently adding light from each point of the selected observation plane. Independently, we tried to mimic the adhesion process of a cell to a substrate by depositing latex spheres on a glass substrate and then heating and melting them progressively. We measured the Mueller matrix of the resulting samples representing different degrees of adhesion.

Comparing the simulated and experimental results, a good matching is found. This guaranties that the calculation is a good way for explaining the special features found in the experiment, like the size and amount of rings observed in the boundaries, but also allows us to identify the polarimetric parameters of interest in this configuration, like the linear dichroism and birefringence. These seem to be the most sensitive to the adhesion state of a sphere, with a peak in the azimuth value and position that seem to be strongly dependent of the melting state of the samples. This could be used to estimate the apparent and curvature radii,  $a$  and  $r$ , of a particle in a process of adherence.

Another interesting feature that we have found is the dependence of the appearance of an interferential ring on the  $NA$  of the observing system. This transition is directly related to the aspect ratio of the cap formed by the adherent particle.

We conclude that polarimetry, even in the usually less sensitive transmission configuration, produces special features that can be very useful to determine the degree of adhesion of a particle to a surface, something that can be applied, for instance, in the context of biological culture of cells, where the detachment process is closely

related to cell death [76], and also to other physical phenomena in which the particle is able to keep a quasi-spherical profile.

# Chapter 7

## Other approaches

During the realization of the thesis, several approaches (different to those presented so far) were attempted to optically study individual cells, either in cultures or suspensions were attempted. For different reasons, these lines of investigation were not as fruitful as we would have liked and, were not continued. In this chapter, some of these studies and models will be described and presented.

The first step in knowing the optical information attainable from a physical object is knowing its scattering and absorption response. Cells are complex entities, and to calculate their scattering is necessary to simplify its geometry, for instance by approximating its shape by a sphere of a given refractive index [116, 117]. In this context, the first option was Mie calculus. Limitations of Mie theory can be partially overcome by the DDA (Discrete Dipole Approximation) in the sense that it does not require the spherical shape and homogeneity demanded by Mie theory. In both cases, it would open a way to the calculation of the Mueller matrix of a sphere of radius and refractive index similar to that of cells.

Regarding other experimental approaches considered, we will mention here some initial tests regarding the use of speckle patterns produced by suspensions of cells in order to study movements connected to their motility, a property that is characteristic of migrant cancer cells and the process of metastasis.

### 7.1 Mie Scattering

By calculating the Mie scattering for several incident polarizations, we have obtained the Mueller matrix of an isolated sphere embedded in water. Parameters like its radius, refractive index and the wavelength of illumination were varied. The same study has been performed for a coated sphere as a simplified model of a cell with a nucleus and a cytoplasm of different refractive index.

#### 7.1.1 Isolated sphere

The scattering Mueller matrix of an isolated sphere embedded in water ( $n_w = 1.33$ , radius  $r = 5\mu\text{m}$ , refractive index  $n = 1.36$ ) was obtained for a wavelength  $\lambda = 500$  nm, and is shown in Figure 7.1. We obtain a symmetric Mueller matrix with null

values in the off-diagonal  $2 \times 2$  boxes, as corresponding to the axi-symmetric nature of the problem. There is a strong angular dependence in the values of the elements, with great amount of fluctuations, due to the high values of the size parameter  $r/\lambda$ .

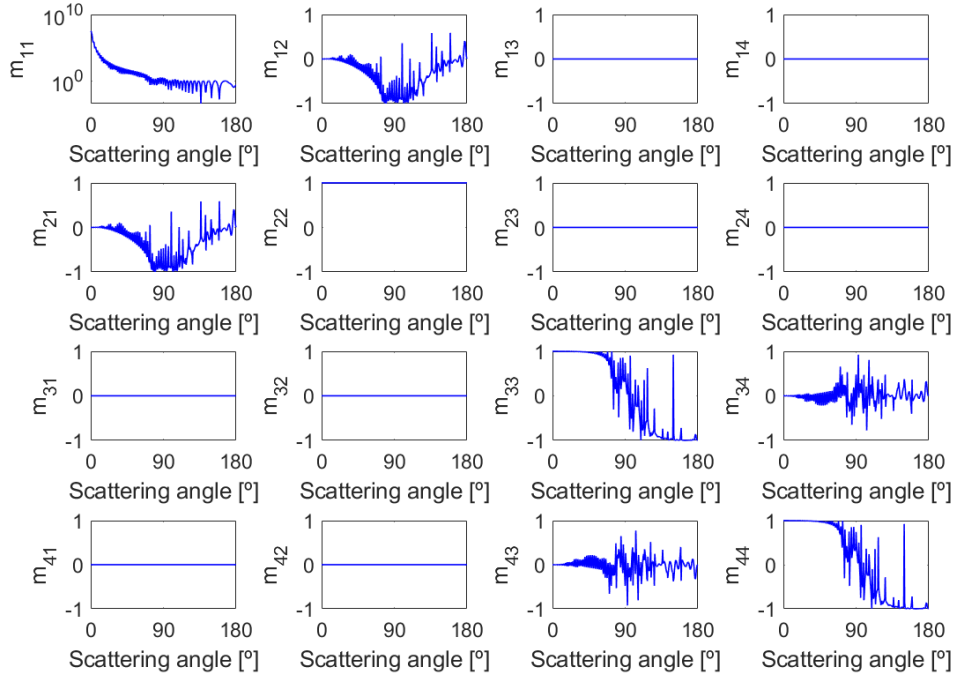


Figure 7.1 - Mueller matrix at  $\lambda = 500 \text{ nm}$  for an isolated sphere in water ( $n_w = 1.33$ ) with radius  $r = 5 \mu\text{m}$  and refractive index  $n = 1.36$ .

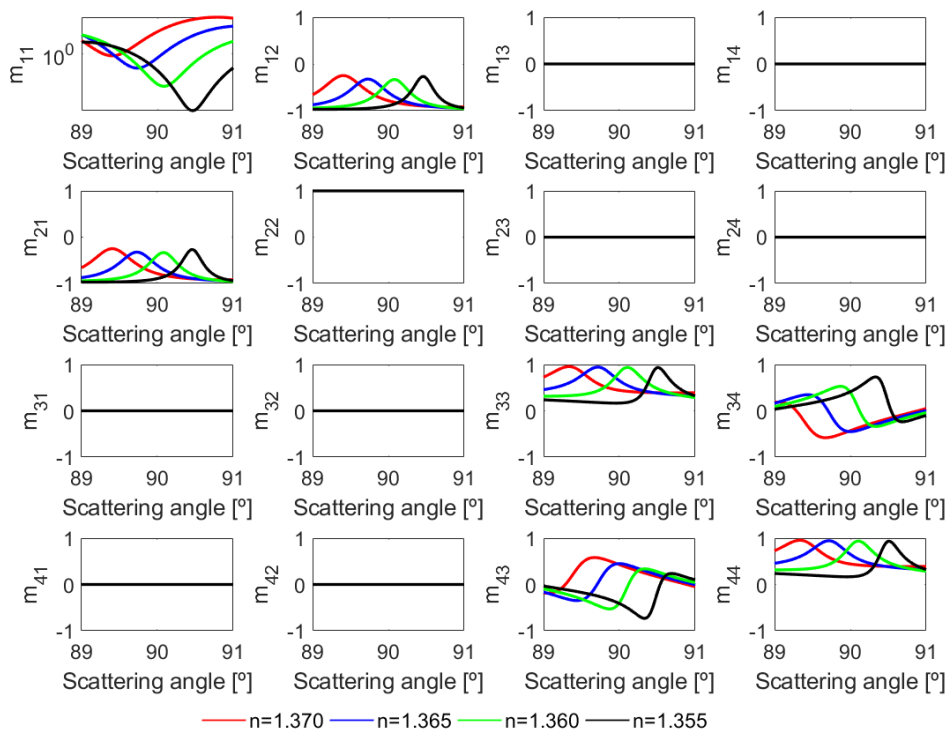


Figure 7.2 - Mueller matrix at  $\lambda = 500 \text{ nm}$  for an isolated sphere in water ( $n_w = 1.33$ ) with radius  $r = 5 \mu\text{m}$  and several refractive indices.

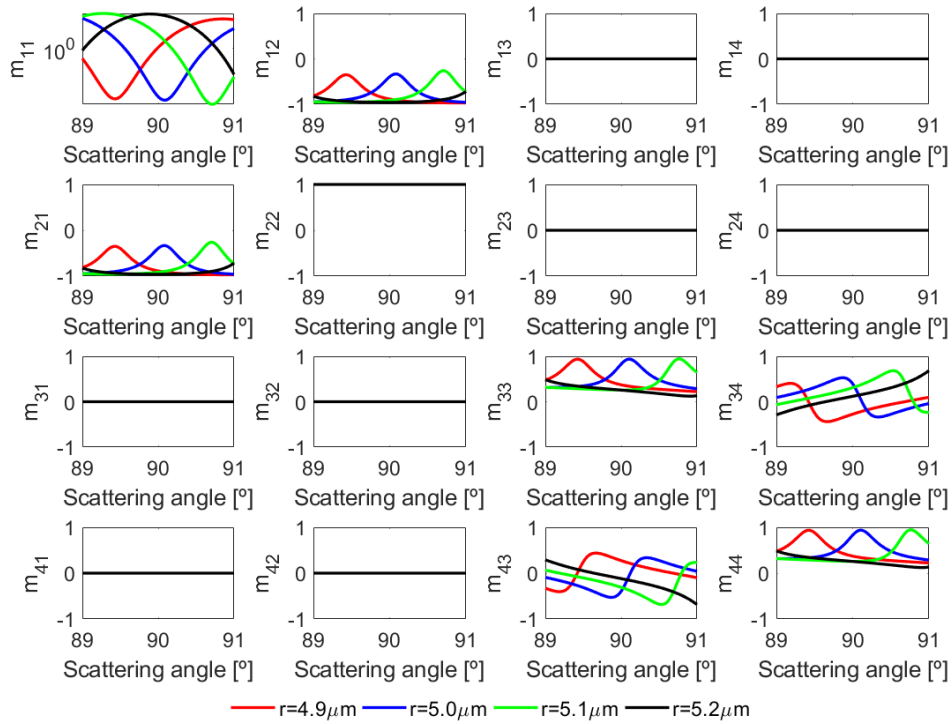


Figure 7.3 - Mueller matrix at  $\lambda = 500\text{ nm}$  for an isolated sphere in water ( $n_w = 1.33$ ) with refractive index  $n = 1.36$  and several radii.

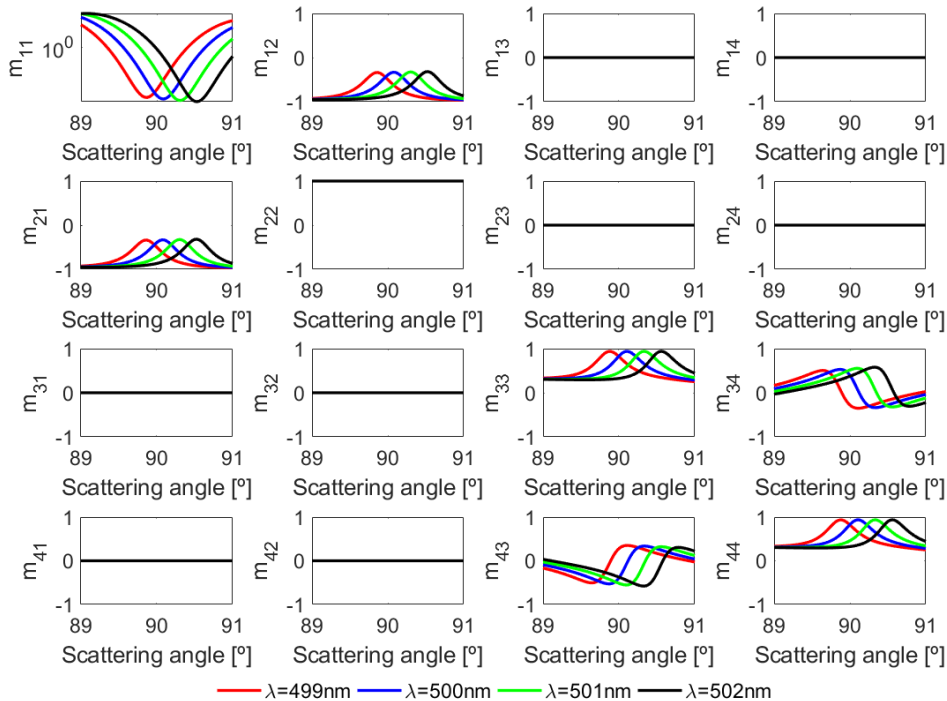


Figure 7.4 - Mueller matrix at several wavelengths for an isolated sphere in water ( $n_w = 1.33$ ) with radius  $r = 5\ \mu$  and refractive index  $n = 1.36$ .

In order to take a closer look at the angular dependences, a study of the variation of the  $\mathbf{M}$  elements centered around a scattering angle of  $90^\circ$  was performed. This

angle was selected based on typical experiments done with flow cytometry [118], a technique in which light scattered by cells at different angles is collected and compared in order to measure their physical characteristics such as the size and the granularity. Figures from 7.2 to 7.4 show the variations when i) the refractive index of the particle,  $n$ , is varied (Figure 7.2); ii) when its radius,  $r$ , changes (Figure 7.3) and iii) when the wavelength of illumination,  $\lambda$ , changes (Figure 7.4). (The range of values chosen for the refractive index is purposely more significant than the range chosen for  $r$  and  $\lambda$ ).

We observe that small variations in the size of the sphere or in the illuminating wavelength produce important changes in the value of the elements of  $\mathbf{M}$ , similar to the changes produced by the variations in the refractive index. This evidences that the possibility of experimentally studying the refractive index variations of cells by analysing its characteristic scattering is remote, since a realistic experiment involves important intervals of sizes and wavelengths

### 7.1.2 Coated sphere

Other test included calculus of the Mueller matrix for coated spheres, as an attempt to approach the sphere model to a cell, with a nucleus of higher refractive index and a cytoplasm. Figure 7.5 shows the Mueller matrix of a coated sphere embedded in water with a nucleus of radius  $r_1 = 2 \mu\text{m}$  and refractive index  $n_1 = 1.37$  and an external coat of  $r_1 = 5 \mu\text{m}$  and refractive index  $n_1 = 1.35$ .

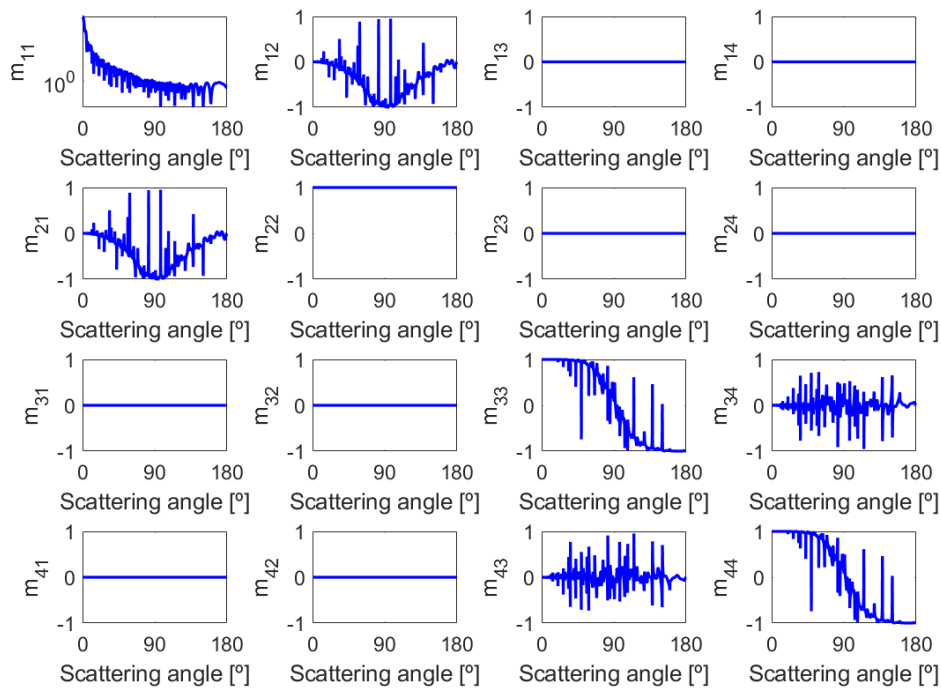


Figure 7.5 - Mueller matrix for a coated sphere in water ( $n_w = 1.33$ ) with radius  $r_1 = 2 \mu\text{m}$  and  $r_2 = 5 \mu\text{m}$  and refractive index  $n_1 = 1.37$  and  $n_2 = 1.35$ .

As before, elements of  $\mathbf{M}$  are very dependent of small changes either in the refractive index or the size of the different coats. The previous study has been carried out again

for the case of the coated sphere leading to the same conclusions. In what follows, the Mueller matrices obtained when different parameters of the coated sphere are changed are shown.

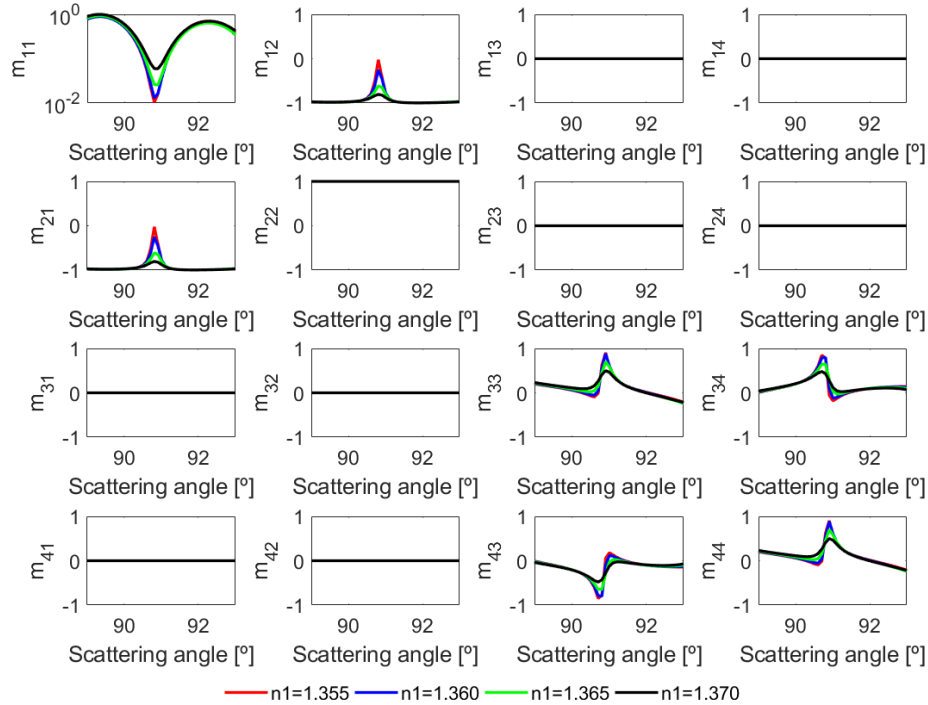


Figure 7.6 - Mueller matrix of a coated sphere in water ( $n_w = 1.33$ ) with radius  $r_1 = 2 \mu\text{m}$ ,  $r_2 = 5 \mu\text{m}$  and index  $n_2 = 1.35$ . Index  $n_1$  varies.

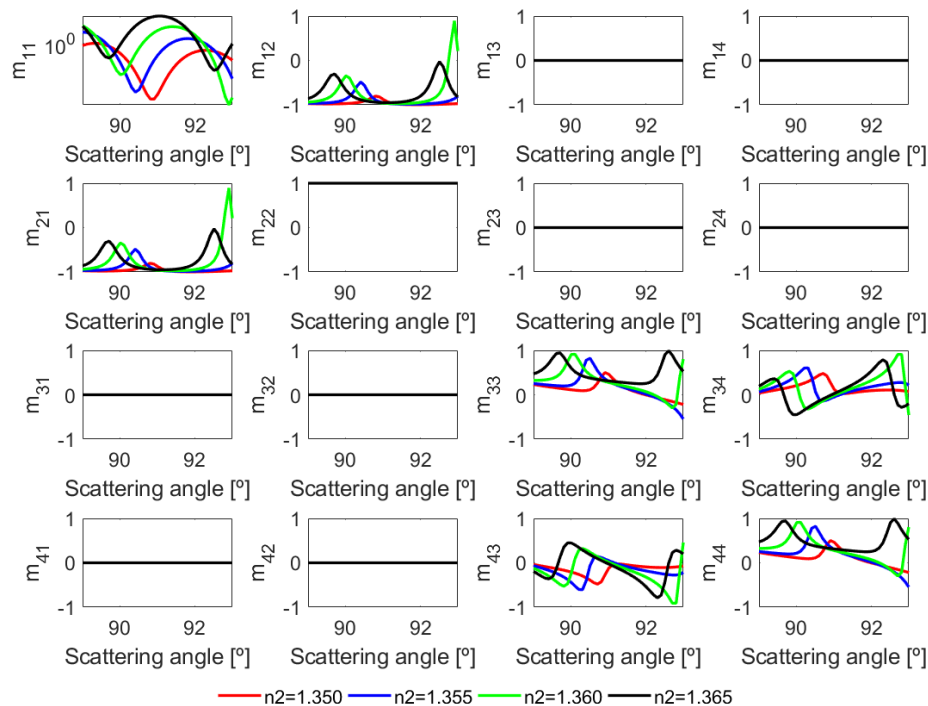


Figure 7.7 - Mueller matrix of a coated sphere in water ( $n_w = 1.33$ ) with radius  $r_1 = 2 \mu\text{m}$ ,  $r_2 = 5 \mu\text{m}$  and refractive index  $n_1 = 1.37$ . Index  $n_2$  varies.

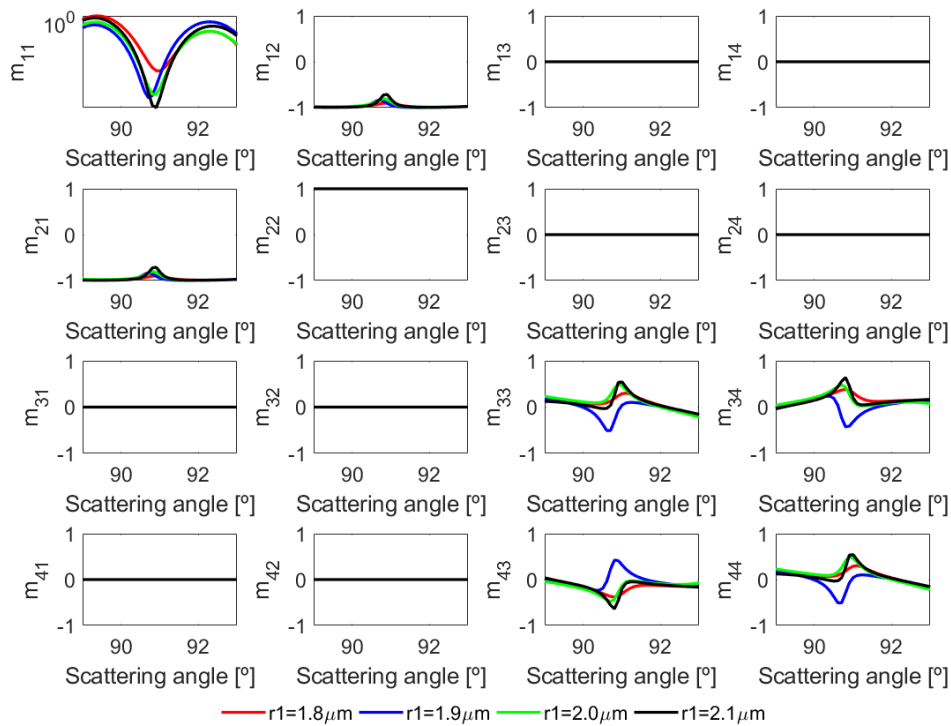


Figure 7.8 - Mueller matrix of a coated sphere in water ( $n_w = 1.33$ ) with variable radius  $r_1$ ,  $r_2 = 5 \mu\text{m}$  and refractive index  $n_1 = 1.37$  and  $n_2 = 1.35$ .

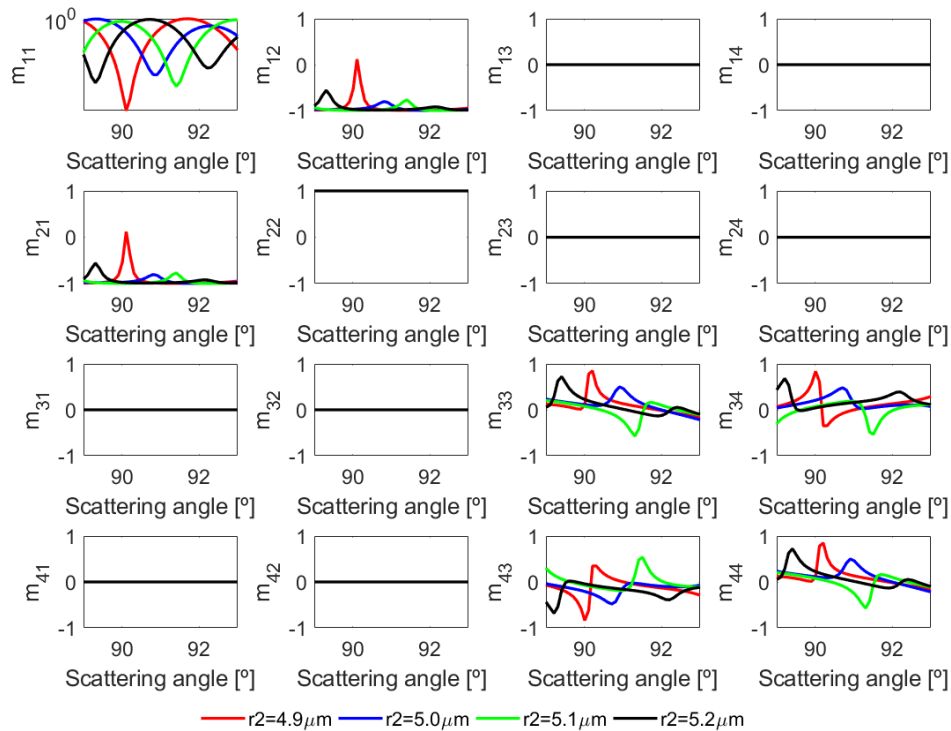


Figure 7.9 - Mueller matrix of a coated sphere in water ( $n_w = 1.33$ ) with radius  $r_1 = 2 \mu\text{m}$ , variable  $r_2$  and refractive index  $n_1 = 1.37$  and  $n_2 = 1.35$ .

## 7.2 Discrete Dipole Approximation (DDA)

This is a conventional numerical method for simulating light scattering from a certain target. The DDA calculus [119] is based on the discretization of the geometry of interest in periodically distributed dipoles, each one representing the optical properties of the material in that location. Consequently, it allows to calculate the Mueller matrix of an isolated particle, not necessarily a sphere. For this reason, it can be considered an adequate tool for simulating the optical response of a cell deposited, or partially adhered, to a surface which is the basic geometry of this research.

There are some technical aspects concerning discretization. For instance, the separation between dipoles,  $d$ , must be small compared to the size of any structure of the target and also smaller than the wavelength. For this last condition the following inequality must be fulfilled [120]:

$$|m|kd < 1 \quad (7.1)$$

where  $m$  is the refractive index of the target and  $k = 2\pi/\lambda$ .

Figure 7.10 shows the geometry and its discretization in dipoles, as a basic approach to study the adherence of a cell to a surface.

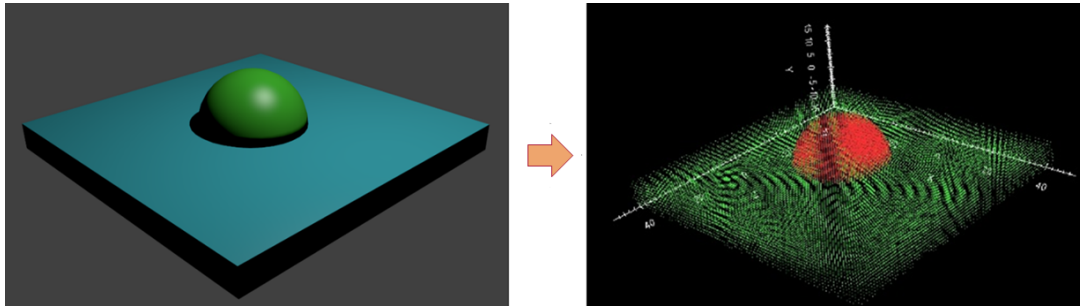


Figure 7.10 - Geometry to study adherence of spherical particles to surfaces (left) and dipole discretization in dipoles for DDA calculation (right).

Blender<sup>1</sup> animation software has been used to build the geometry. Next, it has been discretized using the nanoDDSSCAT+<sup>2</sup> online resource that allows to define the spacing between dipoles and the maximum length of the geometry so that the target is properly discretized in  $N$  dipoles following the equation:

$$V = Nd^3 \quad (7.2)$$

where  $V$  is the total volume of the target.

The drawback in this method of calculation is that the simulated sphere is very large ( $r = 5 \mu\text{m}$ ), provided that we want to produce simulations within the visible range. Then, the number of dipoles required to adequately discretize the entire space is of

<sup>1</sup><https://www.blender.org/>

<sup>2</sup><https://nanohub.org/resources/ddaplus>

the order of  $5 \times 10^5$ . In other words, to obtain a matrix similar to that calculated by Mie theory, the calculation time is extremely long: each configuration, size, shape, wavelength, etc., would require several days. So, this makes impractical the use of this calculation method.

It is interesting to mention that the potential of this method, when computing capacities allow for it, is huge. It could simulate microscopy images of the desired geometry reproducing the observation conditions, like numerical aperture. This is because the light scattered by each point of the target in a certain direction could be collected within a certain numerical aperture and the image could be formed for the desired observation plane. Performing these calculations for several incident polarizations would result in a calculated microscopic Mueller matrix image of the target, fully comparable to the one experimentally measured in the laboratory.

## 7.3 Speckle and cell motility

At an early stage of our work, we considered other experimental approaches to study living cells by means of optical techniques. One of these approaches deserves being mentioned: the study of the dynamic speckle. As it was already mentioned in Chapter 2 (section 2.3), the study of speckle is used to analyse processes in biological samples involving parasites, bacteria and cells [52–54, 51] and also in medical imaging [47, 50]. Due to the great sensitivity of the speckle pattern to small changes in the scattering elements, we thought it could be a suitable method to quantify cell motility or, maybe, identify, adherence or detachment processes. As a main drawback, in order to study long-term processes it is necessary to keep cells in an environment with the optimal conditions to guarantee their survival and correct development. In addition, it is necessary to keep a couple of optical systems (the source creating the speckle and the microscopy system that observes the illuminated region) aligned on the observation area. Another problematic aspect, once the correlation times of the speckle have been found, is to identify the process, or processes, leading to the observed changes.

### 7.3.1 Experimental method

Here we explain what constitutes a "proof of concept" of the proposed method. It gives evidence of its sensitivity but is not complete, in the sense that it lacks of a simultaneous observation through a microscope. Without it, this phase of the work is quite speculative. The experiments were performed with two cell lines: U937 and JURKAT (lymphocyte cells). Cells are suspended in 1.5 ml of R10 medium (RPMI growth medium used in cell culture with 10% of fetal bovine serum and 1% of Penicillin-Streptomycin and specially prepared to keep cells in optimal conditions and provide them the necessary nutrients to live and grow). The volume of suspension is deposited on a Petri dish of diameter  $\phi = 5$  cm creating a layer of less than 1 mm of thickness. The sample is illuminated by a solid state laser ( $\lambda = 650$  nm, spot of 1 mm in diameter approximately) at oblique incidence  $\alpha \approx 30^\circ$  with respect to the substrate normal (see Figure 7.11a). The illuminated

surface/volume produces a clear speckle pattern that is captured with a CCD camera (Retiga Exi Fast, 12 bit, 1392×1040 pixels) controlled from a computer and placed at an angle of approximately  $\beta \approx 40^\circ$  in order to avoid direct reflections. It was checked that both the R10 medium and the surface of the empty Petri dish do not produce a significant speckle signal as compared to that produced by the complete samples, so it can be assured that the main signal comes from the living cells.

In order to collect our signal we need to fix an integration time,  $t_i$ , long enough to produce a good signal.  $t_i = 50$  ms was chosen for our experiments. Images of the speckle pattern are taken each  $\Delta t$  during a period of time  $T$ . Here, we can proceed in two different ways: i) calculating the cross-correlation between every image and the initial one, that acts as a reference; and ii) calculating the cross-correlation between every image and the rest, and then averaging all values corresponding to an interval  $n\Delta t$ , being  $n$  the number of images separating the two images. In both ways, the corresponding decay gives an idea of how fast the speckle is changing and, therefore, the speed of the processes that take place in the cells. While the first operation is adequate to illustrate the changes of a system that degrades -or evolves- from an initial instant in time, the result is, in general, quite noisy, since it produces just one correlation value for each time shift  $n\Delta t$ . However, the second operation seems to be more adequate for stationary systems, in which the processes going on in it, and the corresponding changes introduced in the speckle pattern, are the same regardless of the instant chosen to start the measurement. This operation is less noisy, since the value for each time shift is obtained from an average of many correlation values.

Before starting the measurements, the laser is left to stabilize during one hour so the possible fluctuations of the laser do not affect the speckle produced by the sample (variations due to laser remain  $< 0.1\%$ ).

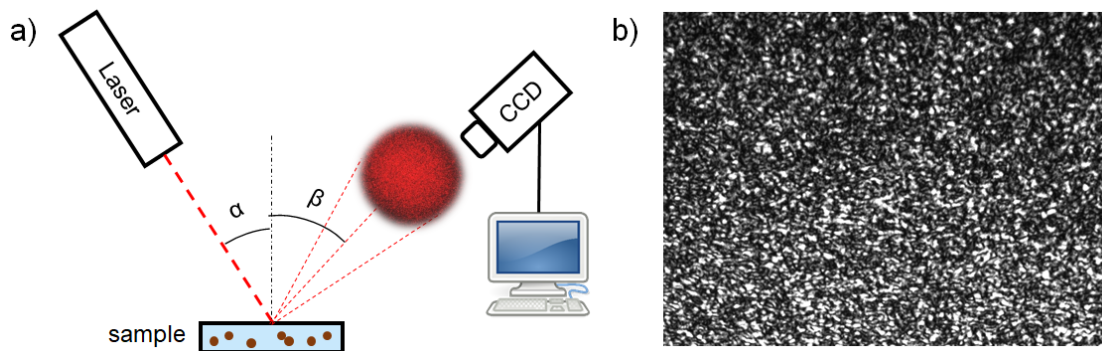


Figure 7.11 - a) Experimental setup used to measure the speckle produced by cell samples. A solid state laser ( $\lambda = 650$  nm) illuminates a Petri dish with cells in R10 medium and a CCD camera captures images of the speckle signal at fixed time intervals. b) One image of the speckle pattern produced by  $5 \times 10^5$  JURKAT cells.

Once a speckle pattern is formed (see Figure 7.11b), we can infer that the number of illuminated scatters is sufficiently high. This was expected since the ratio between the spot and cell sizes guarantees that the number of illuminated cells lies within the interval  $10^2$ - $10^3$ . The speckle contrast is in general smaller than 1 ( $C = 0.67$

for Figure 7.11b). The loss of contrast can be due to the presence of a background in the signal (light scattered in the medium interfaces) and even to the integrated light scattering produced by the small components of the R10 medium. If the cells were still, the speckle would be static and no further information would be expected. However, as a result of cell movement, we can observe a dynamic speckle, i.e. a pattern that evolves with time.

### 7.3.2 Results

Next, we present a group of results obtained from cell suspensions made with cultures of the HT29 and JURKAT cell lines.

#### Time evolution

The first sample is a suspension of 1.5 ml of R10 medium containing  $10^6$  HT29 cells, and placed on a Petri dish. In order to avoid cell death, measurements were taken only during the first hours after the sample preparation. Three independent experiments were carried out, taking images of the speckle patterns for  $T_1 = 6$  min,  $T_2 = 30$  min and  $T_3 = 60$  min each  $\Delta t = 3$  s and with 50 ms integration time. In this way we obtained the evolution of the speckle in short and long periods of time (as shown in Figure 7.12). We chose the dynamic correlation as our preferred operation in order to obtain a good *SNR*. It can be considered a good criterion, since our system is almost stationary during the measurement time. This is shown in Figure 7.13 where four 15 min-long successive measurements of the speckle correlation produce similar time decays.

Before analysing these plots, it is worth to discuss the role of Brownian motion in these experiments, from which, presumably, the fastest possible fluctuation of the signal comes. From the calculation of the translational diffusion coefficient,  $D_T$ , and our scattering conditions, the coherence time,  $\tau_c$ , associated to Brownian motion can be calculated<sup>3</sup>. We obtain  $\tau_c \approx 45$  ms. This time is smaller than the integration time used to collect the images so we would not be able to observe the speckle variation due to this phenomena. Actually, we should not be able to observe any speckle at all. Then, why do we obtain high contrast speckle images instead of blurred ones? The answer is that cells are gravitationally settled down in a very short time after the preparation and our samples are a deposit of cells instead of a suspension<sup>4</sup>. As a result, less than 10% of the substrate surface is covered with cells.

<sup>3</sup>Values used for the calculation: viscosity of water ( $T = 298$  K)  $\eta = 0.00089$  Pa·s; spherical radius  $r = 5 \times 10^{-6}$  m; scattering vector  $k = (4\pi n_m / \lambda) \sin(\theta/2)$ ; scattering angles  $\theta = 110^\circ$ ; wavelength  $\lambda = 0.65 \times 10^{-6}$  m; refractive index of medium  $n_m \approx 1.33$ . With these:  $D_T = (k_B T / 6\pi\eta R)$  being  $k_B$  the Boltzmann constant, and  $\tau = (D_T k^2)^{-1}$ .

<sup>4</sup>According to Stokes laminar flux, limit velocity is  $v_L \approx 3 \times 10^{-6}$  m/s. For the thickness of our solution this implies that in  $t \approx 5$  min all the cells are settled down. Values used: cell radius  $r_c \approx 5 \mu\text{m}$ , cell relative density  $\rho_c \approx 1.05$ , medium viscosity  $\eta \approx 9 \times 10^{-4}$  Pa·s and sample thickness  $z \approx 1$  mm.

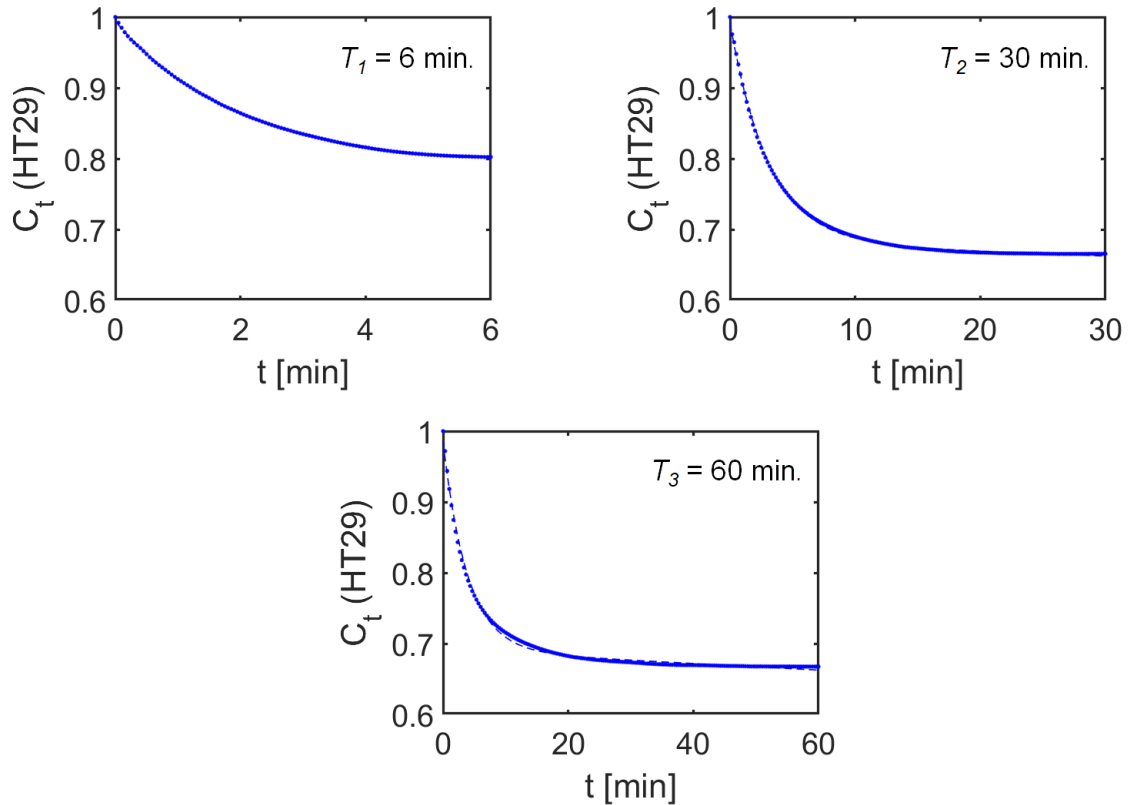


Figure 7.12 - Speckle correlation functions for three different experiments with HT29 cells in R10 medium. Fits to Equation 7.3 are shown with dashed lines

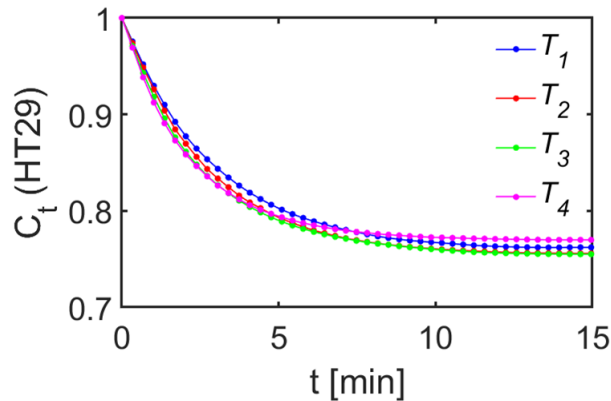


Figure 7.13 - Evolution of four 15 min-long successive measurements of the speckle correlation of HT29 cells in R10 medium. Similar decay is observed independently of the initial time chosen for the measurement.

The decays observed in Figure 7.12 are very fast but the correlation values at long correlation times are very high (between 0.65 and 0.8). The second feature reveals that there is a strong static component in the scattering system while the variation is restricted to a part of it. Concerning the decay, and in order to know about the characteristic fluctuation time, we have introduced a fit to a sum of two exponential functions (Equation 7.3) where coefficients  $a$ ,  $b$ ,  $c$  and  $d$  are always positive and greater than 0, as shown in Table 7.1:

$$f(t) = a * \exp(-bt) + c * \exp(-dt) \quad (7.3)$$

$T$ [min]	$a$	$b$ [ $\text{min}^{-1}$ ]	$c$	$d$ [ $\text{min}^{-1}$ ]	$R$
6	0.2163	0.4825	0.7776	0.0024	0.9997
30	0.3095	0.3229	0.6823	0.0010	0.9991
60	0.2945	0.2554	0.6908	0.0007	0.9954

Table 7.1 - Values of the coefficients  $a$ ,  $b$ ,  $c$  and  $d$  obtained after fitting the speckle correlation decay to a sum of two exponential functions (Equation 7.3) for three independent experiments with HT29 cells. Values of  $R$  – squared are also presented for each case.

Low value of coefficient  $d$  combined with the high values of  $c$  indicated that the quasi-static part of the speckle is the most important one. High values of  $b$  reveal that there is speckle variation with a characteristic time ( $b^{-1}$ ) of a few minutes (2-4 min). This is consistent with all the considerations made at the beginning of this section.

### Effect of cell concentration and different cell lines

In a second set of experiments we performed some tests with different cell concentrations ( $5 \times 10^5$  and  $10^6$  cells in 1.5 ml of R10 medium) of two cells lines: HT29 and JURKAT. Total measurement time was  $T = 60$  min for both cell lines. Results for the speckle correlation are shown in Figure 7.14 for each of the cell lines. The general evolution is similar in both cases to that analysed in the previous case. The resulting coefficients obtained from the fitting to Equation 7.3 are shown in Table 7.2.

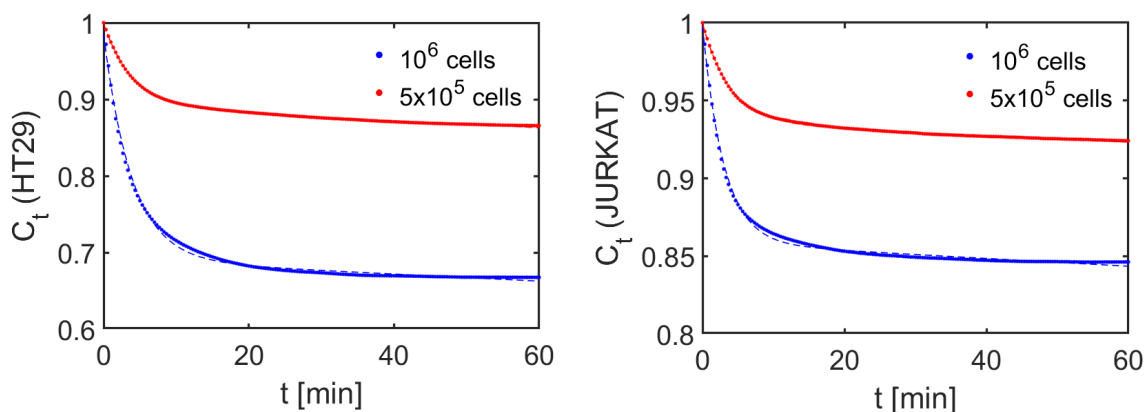


Figure 7.14 - Speckle correlation functions of  $5 \times 10^5$  and  $10^6$  HT29 and JURKAT cells in R10 medium. Fits to Equation 7.3 are shown with dashed lines.

From the values of  $c$  we can conclude that the static component increases its weight for lower concentrations for which the adherence to the substrate is more dominant. Concerning the dynamic component typical variation times ( $b^{-1}$ ) remain within the interval 2-4 min as in the previous case.

Cell line	Concentration	$a$	$b$ [ $\text{min}^{-1}$ ]	$c$	$d$ [ $\text{min}^{-1}$ ]	$R$
HT29	$10^6$	0.2945	0.2554	0.6908	0.0007	0.9954
	$5 \times 10^6$	0.1083	0.2508	0.8906	0.0005	0.9982
JURKAT	$10^6$	0.1395	0.3318	0.8587	0.0003	0.9952
	$5 \times 10^6$	0.06372	0.2597	0.9359	0.0002	0.9986

Table 7.2 - Values of the coefficients  $a$ ,  $b$ ,  $c$  and  $d$  obtained after fitting the speckle correlation decay to a sum of two exponential functions (Equation 7.3) for four experiments with HT29 and JURKAT cells at two concentrations. Values of  $R$  – squared are also presented for each case.

## 7.4 Analysis and conclusions

One of the problems that arises when studying light scattering from cells both in simulations and in experiments, is that they are mainly transparent and with a refractive index close to that of water. Therefore, the expected optical contrast is very small, and the corresponding scattered signal is very weak. In an attempt to simulate the scattered light of a biological cell, we tried several approaches that allow to calculate its Mueller matrix when illuminating with a plane wave of a certain wavelength.

Regarding the calculation of Mueller matrices using Mie scattering, we found that the results are highly angular dependent, with fast fluctuations. Small variations in the radius of the sphere and the illuminating wavelength produce a subtle but notable change in the elements of the matrix comparable to that produced by the refractive index variations. Then its use for the study of individual cells can be considered unrealistic since, within a population of cells, there is a certain range of sizes and shapes that make the refractive index variations inside cells (or between individual cells) almost impossible to assess by this means. In conclusion, the extreme sensitivity to angular variations plays against scattering as a means to detect changes occurring in cells. It could be employed to study changes in the mean size or mean refractive index of a population of cells in suspension as averaged magnitudes or to study characteristics of individual cells as it is done in flow cytometry.

As for the simulation with DDA, the main problem arising here is the huge size of the particle and the high discretization necessary to correctly performing the required calculations exceeds the computer capabilities. Still, it can be foreseen that the continuous growth of computing possibilities will allow at some point to develop "simulated microscopy" that could account for the local inhomogeneous properties of cells under almost any observation conditions.

Independently, we tried an experimental approach to the problem of motility based on the analysis of the variations in the speckle pattern produced by a deposit of living cells. We performed speckle measurements on two cell lines at different concentrations in a medium with nutrients. Then, the dynamic correlation was calculated as a function of time. Because the time between the sample preparation and the measurement is longer than the time the cells take to settle down, our

samples should be considered cell deposit instead of suspensions, and consequently Brownian motion is not playing a significant role. The main observations are: i) the importance of quasi-static speckle, even more for lower density samples in which the substrate increases its role, and ii) the typical fluctuations times (2-4 min) presumably associated to cell motility in these experiments.

In order to continue this line of investigation, it would be necessary to design and assemble a setup that allows, first, to keep living cells in optimal conditions and second, to align two experimental setups on the same sample point, one to illuminate and obtain the speckle and the second to monitor the image and know about their motion. Such setup would have applications to study cell motility, adherence, and other dynamic processes going on in a population of cells.

# Chapter 8

## Summary

In this chapter, a brief summary of the work done is presented, including the tasks carried out and the main conclusions reached during the realization of the thesis. In addition, the future lines of work are suggested, discussing the different possibilities and applications.

### 8.1 Completed tasks

This work has involved carrying out both computational and experimental task. At the same time, and due to the undeniable interdisciplinary character of this thesis, it was necessary to get familiar with the fundamentals of cell biology that allows to understand the processes under study. Some of these tasks have been:

- ▷ *Interdisciplinary thesis*: my background is physics and, in particular, optics and polarimetry. A deep revision of bibliography was required in order to understand the basics concepts in cell biology. Also, a wide revision of the applications of polarimetry and light polarization in the area of medicine and biology was carried out. In addition, working in a multidisciplinary environment with people from different areas has greatly contributed to enrich my understanding and skills during these years.
- ▷ *Experimental work*: adapting the previously existing setup to the new requirements has been a great effort. Observation of microscopic biological samples demanded a new imaging geometry and an adequate illumination systems. In addition to this a correct –and rather complicate- protocol had to be designed to prepare the samples and perform the polarimetric measurements in optimal conditions. As a result, we now possess a detailed and tested method to work with these samples in the context of optical measurements.  
At the same time, I had the possibility of enjoying two internships at LPICM, to work in a group with vast experience in polarimetry and to being able to handle another experimental setup. This has been of great help for clarifying theoretical concepts and learning new experimental skills.
- ▷ *Computational tasks*: I have developed both the scripts required to analyse the raw experimental Mueller matrix and the polarization ray tracing code to calculate the transmission Mueller matrices of big spheres and spherical caps

on substrates. The difficulties (the wide variety of ways to decompose and obtain optical parameters from the Mueller matrix, the lack of agreement in some sign criteria, the diversity of definitions in light polarization theory, the implementation of the equations, etc.) have made this part quite challenging for me.

## 8.2 General conclusions

We have addressed the problem of studying living cells by optical techniques from different perspectives, giving greater weight to the applied polarimetry. In particular, we have focused in three main processes that take place in living cells: apoptosis or cell death, adherence and motility.

The main conclusions are summarized below.

### 8.2.1 Polarimetry in cancerous cells: cell death detection

We have worked with 4 different cell lines: colorectal adenocarcinoma HT29 cell line, breast cancer MCF7 cell line and leukemia cell lines U937 and THP1. We have designed and optimized a protocol for preparing and measuring samples of biological cells by means of an imaging polarimeter. This includes: depositing an homogeneous layer of cells which cover the whole imaged surface and fixing them to the substrate while keeping them in optimal conditions so that they do not get stressed and die, and avoiding the appearance of artefacts in the culture that might affect the polarimetric measurements.

By measuring and decomposing the Mueller matrix of these cell samples, we have explored the polarimetric response of several cell populations, belonging to some well-known cell lines, after undergoing treatments with different chemotherapeutic agents, at different concentrations and times, commonly used to induce cell death. We observed that certain polarimetric parameters such as diattenuation, dichroism, anisotropy and birefringence, show a significant variation when cells undergo apoptosis.

A detailed study of cell death has been carried out over two cell lines, U937 and THP1. Cell death has been assessed with two traditional and commonly used essays: Alamar Blue (for evaluating cell viability) and trypan blue (for measuring cell death). In parallel, target samples were prepared from the cell cultures for each case, and polarimetric measurements were carried out on them. We treated a cell population of U937 with cisplatin for a long period of time, performing measurement of the Mueller matrix at several time points. We observed a similar trend in parameters such as diattenuation, birefringence and dichroism: an increase in their value according to the percentage of cell death. Diattenuation was chosen as the most sensitive magnitude. We found a strong correlation between cell death and diattenuation values, showing a significant increase even at short times and low cell death rates. Moreover, the spatial distribution of the diattenuation signal in the images (mainly observed in the edges of the cells) suggests that the diattenuation enhancement is associated with changes in the plasma membrane and in the geometry (shrinking) of the cell itself. This

is in agreement with the fact that plasma membranes suffer major changes during the apoptosis process including loss of phospholipid asymmetry, and alterations in membrane tension and curvature due to modification of membrane-associated molecules.

Therefore, we conclude that polarimetry could be an objective tool to detect cell death, useful both for assessing *in vitro* killing efficacy of drugs under development and for the follow-up of leukemia patients undergoing therapy with cytotoxic agents.

Although the type of cell death detected is likely to be apoptotic because cisplatin treatment induces apoptosis, further studies will reveal whether diattenuation is able to discriminate between the different types of cell death. Moreover, since this method can be implemented in a microscope (although further work is necessary for that), it could result in an objective (i.e. independent of the observer) polarimetric method of analysis, complementary to the traditional techniques used for cell death quantification.

### 8.2.2 Adherence of spherical particles to a flat surface

There are many situations of interest that are related to the geometry of soft spherical particles close -and adhering- to a surface. The case of biological cells is probably one of the most appealing ones because of their attachment/detachment processes, closely connected with their adhesion capacity and their ability to migrate.

Working with cells is a complicated task since they need specific conditions to stay alive. Experiments are quite limited by time, and because of this, we attempted different ways to simulate or mimic the optical behaviour of a cell. In order to do that, we developed two complementary approaches, one based on a phantom made of latex microspheres deposited on a glass substrate and other one based on polarization ray optics that allows to calculate the Mueller matrix of spheres and spherical caps of different refractive indices.

On one hand, the phantom made of latex microspheres allows to somehow mimic the shape and behaviour of the adhesion process of a cell to a flat substrate: by applying heat, these spheres partially melt, so that different degrees of curvature and spreading can be achieved. These samples, once they get cooled down are stable in time, making it easier to work with and to perform polarimetric measurements on them. On the other hand, the polarization ray tracing model allows to calculate the Mueller matrix of different geometries based on the sample created.

We explored the polarimetric behaviour of samples of spheres with different degree of adhesion (progressively melted) and compared them to the results given by the ray tracing calculation. Comparison between the experimental transmission Mueller matrices and the simulated ones have shown good agreement, reproducing special features observed in the experiment such as the interference rings appearing in the boundary at low degrees of melting and high numerical apertures. In particular we have found that the dependence of the appearance of an interference ring on the numerical aperture of the observing system can be used to assess the aspect ratio of

the cap formed by the adherent particle. Moreover, polarimetric parameters such as linear dichroism and birefringence seem to be the most sensitive to the change produced in the degree of curvature during the adhesion process. While the peak observed in the birefringence cross-sections decays rapidly once the particle begins to melt, the one associated to dichroism decreases progressively with the flattening produced during the adherence.

We conclude that the microscopic imaging of polarimetric parameters shows special features that can be very useful to determine the degree of adhesion of a particle to a surface or the curvature of an element close to a flat surface. This is something that can be applied, for instance, in the context of biological culture of cells, where the detachment process is related to cell death and the migration ability, but also in other physical areas with interest in processes involving soft (i.e. liquid) spherical particles.

### 8.3 Future work

Many promising aspects and ideas have emerged during these years of work. Some of them cannot be properly addressed and others, due to time constraints, have not been fully developed. However, there are several points we have worked on that deserve research and development in the future, and it is worth mentioning them here.

Regarding the work with living cells, investigation of cell death detection could be continued and extended to other cells lines and treatments. Exploring the polarimetric response to cell death on different cell lines and under different treatments would allow to consolidate the results obtained and perhaps lay the foundations for a future tool, based on polarimetry, that could be employed as a complementary laboratory method in cell death detection.

In the same way, one of the most promising aspects that was not attempted due to lack of time, was the application of the polarimetric approach to the detection of other cellular processes such as mitosis, making use of our current protocol to prepare this kind of biological samples. For instance, it is possible to "pause" the cell cycle in a given point, so that a high percentage of the population is in a particular phase, and then check the sensitivity of our polarimetric method. As with the samples at different times of cell death treatment, it is possible that one, or several, polarimetric parameters can differentiate some of the phases in the cycle. Eventually, and provided that the resolution of this technique is optimized, it could be applied to the detection of local, or structural, processes taking place inside the cells.

From the polarimetric point of view, another interesting aspect is the measurement configuration. A reflectance setup for instance could offer a new perspective of the polarimetric parameters of interest and their sensitivity.

Another promising line that deserves continuation is the cell motility assessment through speckle pattern correlation. We have observed in our proof-of-concept experiments the presence of static and variable components of the speckle obtained from living cells deposit, the typical time variations or the influence of cell concentration. Several tasks are required for further studies along this line. In the first place,

controlled proofs that allow to recognize the different origins of motility. Then, some advanced setup that combines microscopy observation and speckle collection systems, both aligned on the same spot and able to work alternatively. And this for a sample located in a isolated chamber where cells are kept in adequate conditions to assure their survival. This rather complicated setup could be able to monitor, in a comprehensive way, processes such as motility on a surface or attachment/detachment processes.

On the other hand, the polarization ray tracing model used to calculate the Mueller matrix of spheres and spherical caps offers some ways to upgrade its capabilities. Regarding the illumination, now running from substrate to cell, could be extended to the opposite direction. In addition, normal incidence could be extended to the oblique situations, though this is not an straightforward issue. With respect to the target geometry, another spherical, or quasi-spherical, pair of dioptrics, could be added inside the main cap so that, playing with different refractive indices and sizes, a more accurate model of a cell with a nucleus and surrounding cytoplasm could be simulated. Also, the model could be extended to other geometries so that the shape of a cell or soft particle adhered to a flat surface could be represented more in detail, taking into account, for example, the surface tension at the edges. For this purpose, other geometries could be used, such as ellipsoids or spheroids. In relation to this, it would be very interesting and clarifying to have high resolution images, and movies, of the process of adherence and further spreading of a cell in a flat substrate, as well as of the opposite, or detachment, process.

Finally, and in summary, this thesis has opened, in my opinion, the way to a line that can be very promising and prolific: the application of polarimetric imaging to cell analysis, as an approach that can provide new insights to the study and monitoring of cell processes and with numerous application in the area of cell biology.



Part III  
APPENDIX



# Appendix A

## Conferences contributions and publications

### A.1 Scientific publications

- ▷ A. Fernández-Pérez, T. Sang Hyuk Yoo, J.L Fernández-Lunac F.Moreno, E. García-Caurel, J.M. Saiz. *Polarimetric analysis of a fused sphere as a model for adherent particles*. (Sent for publication to Optik, currently under review).
- ▷ Andrea Fernández-Pérez, Olga Gutiérrez-Saiz, José Luis Fernández-Luna, Fernando Moreno and José María Saiz, *Polarimetric detection of chemotherapy-induced cancer cell death*. Applied Sciences 9 (14), 2019.
- ▷ Thomas Sang Hyuk Yoo, A. Fernández, F. Moreno, J. M. Saiz, R. Ossikovski, E. Garcia-Caurel, *Multimodal imaging Mueller polarimetric microscope to study polarimetric properties of spheroidal microparticles*. Proceedings Volume 10678, Optical Micro- and Nanometrology VII; 106780J (2018).
- ▷ A. Fernández J. M. Saiz Vega, F. Moreno y J. L. Fernández-Luna, *Mueller matrix imaging and analysis of cancerous cells*. Proceedings Volume 10453, Third International Conference on Applications of Optics and Photonics; 104531J (2017).
- ▷ R. Alcaraz de la Osa, A. Fernández, Y. Gutiérrez, D. Ortiz, Francisco Gonzalez, F. Moreno, J. M. Saiz, *The extended Kubelka-Munk theory and its application to colloidal systems*. Proceedings Volume 10453, Third International Conference on Applications of Optics and Photonics; 104531F (2017).

### A.2 Conference contributions

- ▷ A. Fernández, Thomas Sang Hyuk Yoo, J.L. Fernández-Luna, F. Moreno, Enric García-Caurel, J.M. Saiz, "Imaging polarimetry of adherent particles: Experimental model based on fused latex spheres." Poster at Photonics and Electromagnetics Research Symposium (PIERS 2019), Rome (Italy), June 2019.

- ▷ A. Fernández, J.L. Fernández-Luna, F. Moreno, J.M. Saiz, "Measurement of the Muller matrix of biological cells: polarimetry to detect cell death." Poster at 8th International Conference on Spectroscopic Ellipsometry , Barcelona (Spain), May 2019.
- ▷ A. Fernández, Thomas Sang Hyuk Yoo, J.L. Fernández-Luna, F. Moreno, Enric García-Caurel, J.M. Saiz, "Modelling the adhesion of a spherical particle to a substrate with geometric optics and polarimetry." Poster at Biophotonics and Optical Angular Momentum, Palaiseau (France), October 2018.
- ▷ A. Fernández, Thomas Sang Hyuk Yoo, J.L. Fernández-Luna, F. Moreno, Enric García-Caurel, J.M. Saiz, "Modelling the adherence of a cell to a flat substrate through polarimetric methods based on Mueller matrix formalism." Invited talk at Progress in electromagnetics research symposium, Toyama (Japan), August 2018
- ▷ Thomas Sang Hyuk Yoo, A. Fernández, F. Moreno, J. M. Saiz, R. Ossikovski, E. Garcia-Caurel, "Multimodal imaging Mueller polarimetric microscope to study polarimetric properties of spheroidal microparticles.", Talk at SPIE Photonics Europe, Strasbourg (France), April 2018
- ▷ D. Ortiz, J. M. Saiz, Ángela I. Barreda, Y. Gutiérrez, A. Fernández, R. Alcaraz de la Osa, F. González y F. Moreno, "Un resumen de la aportación al campo de la Nanofotónica del Grupo de Óptica de la Universidad de Cantabria" Talk at XII Reunión Nacional de Óptica, Castellón (Spain), July 2018
- ▷ A. Fernández, Thomas Sang Hyuk Yoo, J.L. Fernández-Luna, F. Moreno, Enric García-Caurel, J.M. Saiz, "Mueller matrix formalism applied to the study of biological cells", Poster at World Congress on Medical Physics and Biomedical Engineering, Prague (Czech Republic), June 2018.
- ▷ A. Fernández, Y. Gutiérrez, J. L. Fernández-Luna, F. Moreno y J. M. Saiz, "A polarimetric analysis applied to human cells." Poster at The 8th International Conference on Metamaterials, Photonic Crystal and Plasmonics, Incheon - Seoul (South Korea), July 2017
- ▷ R. Alcaraz de la Osa, A. Fernández, Y. Gutiérrez, D. Ortiz, Francisco Gonzalez, F. Moreno, J. M. Saiz, "The extended Kubelka-Munk theory and its application to colloidal systems." Talk at III International Conference on Applications of Optics and Photonics, Faro (Portuga), May 2017.
- ▷ A. Fernández J. M. Saiz Vega, F. Moreno y J. L. Fernández-Luna, "Mueller matrix imaging and analysis of cancerous cells". Poster at III International Conference on Applications of Optics and Photonics, Faro (Portuga), May 2017.

# References

- [1] Jose J. Gil and Razvigor Ossikovski. Polarized Light and the Mueller Matrix Approach. *CRC Press*, 2016.
- [2] Freddie Bray, Jacques Ferlay, Isabelle Soerjomataram, Rebecca L. Siegel, Lindsey A. Torre, and Ahmedin Jemal. Global cancer statistics 2018: GLOBOCAN estimates of incidence and mortality worldwide for 36 cancers in 185 countries. *CA: A Cancer Journal for Clinicians*, 68(6):394–424, 2018.
- [3] Frans Snik, Julia Craven-Jones, Michael Escuti, Silvano Fineschi, David Harrington, Antonello De Martino, Dimitri Mawet, Jérôme Riedi, and J. Scott Tyo. An overview of polarimetric sensing techniques and technology with applications to different research fields. In *An overview of polarimetric sensing techniques and technology with applications to different research fields*, volume 9099, page 90990B, 2014.
- [4] J. Scott Tyo, Dennis L. Goldstein, David B. Chenault and Joseph A. Shaw. Review of passive imaging polarimetry for remote sensing applications. *Appl. Opt.*, 45(22):5453–5469, 2006.
- [5] Nirmalya Ghosh. Tissue polarimetry: concepts, challenges, applications, and outlook. *Journal of Biomedical Optics*, 16(11):110801, 2011.
- [6] Russell A. Chipman. Polarimetry. *OSA Handbook of Optics*, pages 22.21–22.35, 1995.
- [7] James Hough. Polarimetry: A powerful diagnostic tool in astronomy. *Astronomy and Geophysics*, 47(3):31–35, 2006.
- [8] Honghui He, Jintao Chang, Chao He, and Hui Ma. Transformation of full 4 x 4 Mueller matrices: a quantitative technique for biomedical diagnosis. In *Transformation of full 4 x 4 Mueller matrices: a quantitative technique for biomedical diagnosis*, number April, page 97070K, 2016.
- [9] Iftikhar Ahmad, Manzoor Ahmad, Karim Khan, Sumara Ashraf, Shakil Ahmad, and Masroor Ikram. Ex vivo characterization of normal and adenocarcinoma colon samples by Mueller matrix polarimetry. *Journal of Biomedical Optics*, 20(5):056012, 2015.
- [10] Angelo Pierangelo, Abdelali Benali, Maria-Rosaria Antonelli, Tatiana Novikova, Pierre Validire, Brice Gayet, and Antonello De Martino. Ex-vivo characterization of human colon cancer by Mueller polarimetric imaging. *Opt. Express*, 19(2):1582–1593, 2011.
- [11] Angelo Pierangelo, Andre Nazac, Abdelali Benali, Pierre Validire, Henri Cohen, Tatiana Novikova, Bicher Haj Ibrahim, Sandeep Manhas, Clement Fallet,

- Maria-Rosaria Antonelli, and Antonello-De Martino. Polarimetric imaging of uterine cervix: a case study. *Optics Express*, 21(12):14120–14130, 2013.
- [12] Honghui He, Nan Zeng, Minghao Sun, Yihong Guo, Jian Wu, and Shaoxiong Liu. Mueller matrix polarimetry for differentiating characteristic features of cancerous tissues. *Journal of Biomedical Optics*, 19(7), 2014.
- [13] Iftikhar Ahmad, Manzoor Ahmad, Karim Khan, and Masroor Ikram. Polarimetry based partial least square classification of ex vivo healthy and basal cell carcinoma human skin tissues. *Photodiagnosis and Photodynamic Therapy*, 14:134–141, 2016.
- [14] R. S. Gurjar, V. Backman, L. T. Perelman, I. Georgakoudi, K. Badizadegan, I. Itzkan, R. R. Dasari, and M. S. Feld. Imaging human epithelial properties with polarized light-scattering spectroscopy. *Nature Medicine*, 7(11):1245–1248, 2001.
- [15] S. Firdous, M. Atif, and M. Nawaz. Study of Blood Malignancy in Vitro for the Diagnosis and Treatment of Blood Diseases Using Polarimetry and Microscopy. *Lasers in Eng.*, 19:291–305, 2010.
- [16] Miriam Menzel, Markus Axer, Katrin Amunts, Hans De Raedt, and Kristel Michielsens. Diattenuation Imaging reveals different brain tissue properties. *Scientific Reports*, 9(December 2018):1–12, 2019.
- [17] Romain Ceolato, Nicolas Riviere, Raphaël Jorand, Bernard Ducommun, and Corinne Lorenzo. Light-scattering by aggregates of tumor cells: Spectral, polarimetric, and angular measurements. *Journal of Quantitative Spectroscopy and Radiative Transfer*, 146:207–213, 2014.
- [18] Huafeng Ding, Jun Q Lu, R Scott Brock, Thomas J McConnell, Jenifer F Ojeda, Kenneth M Jacobs, and Xin-hua Hu. Angle-resolved Mueller matrix study of light scattering by B-cells at three wavelengths of 442, 633, and 850 nm. *Journal of Biomedical Optics*, 12(3):34032, 2013.
- [19] Woo June Choi, Do In Jeon, Sang-Gun Ahn, Jung-Hoon Yoon, Sungho Kim, and Byeong Ha Lee. Full-field optical coherence microscopy for identifying live cancer cells by quantitative measurement of refractive index distribution. *Optics Express*, 18(22):23285, oct 2010.
- [20] P. Y. Liu, Lip Ket Chin, Wee Ser, H. F. Chen, C.-M. Hsieh, Chau-Hwang Lee, K.-B. Sung, Teck Choon Ayi, Peng Huat Yap, Bo Liedberg, Kuan Wang, Tarik Bourouina, and Yamin Leprince-Wang. Cell refractive index for cell biology and disease diagnosis: past, present and future. *Lab on a chip*, 16:634–644, 2016.
- [21] Suman Shrestha, Aditi Deshpande, Tannaz Farrahi, Thomas Cambria, Tri Quang, Joseph Majeski, Ying Na, Michalis Zervakis, George Livanos, and George C. Giakos. Label-free discrimination of lung cancer cells through mueller matrix decomposition of diffuse reflectance imaging. *Biomedical Signal Processing and Control*, 40:505–518, 2017.
- [22] Wenhuan Jiang, Jun Qing Lu, Li V. Yang, Yu Sa, Yuanming Feng, Junhua Ding, and Xin-Hua Hu. Comparison study of distinguishing cancerous and normal prostate epithelial cells by confocal and polarization diffraction imaging. *Journal of Biomedical Optics*, 21(7):071102, 2015.

- [23] Zhidi Liu, Ran Liao, Jiachen Wan, Hui Ma, Priscilia T.Y. Leung, Meng Yan, Tak Cheung Wai, and Jiarui Gu. Polarization staining and high-throughput detection of marine microalgae using single cell average Mueller matrices. *Optik*, 180(October 2018):84–90, 2019.
- [24] Li Xianpeng, Ran Iao, Jialing Zhou, Priscilla T. Y. Leung, Meng Yan, and Hui Ma. Classification of morphologically similar algae and cyanobacteria using Mueller matrix imaging and convolutional neural networks. *Appl. Opt.*, 56(23):6520–6530, 2017.
- [25] Saeedesadat Badiyan, Arezou Dilmaghani-Marand, Mohammad Javad Hajipour, Ali Ameri, Mohammad Reza Razzaghi, Hashem Rafii-Tabar, Morteza Mahmoudi, and Pezhman Sasanpour. Detection and Discrimination of Bacterial Colonies with Mueller Matrix Imaging. *Scientific Reports*, 8(1):10815, 2018.
- [26] Sophie Brasselet. Polarization- Resolved Microscopy in the life sciences. *OPTICS & PHOTONICS NEWS*, 30(4):34–41, 2019.
- [27] Amelia Ahmad Khalili and Mohd Ridzuan Ahmad. A Review of cell adhesion studies for biomedical and biological applications. *International Journal of Molecular Sciences*, 16(8):18149–18184, 2015.
- [28] Shih-Yau Lu and Russell A. Chipman. Interpretation of Mueller matrices based on polar decomposition. *Journal of the Optical Society of America A*, 13(5):1106, 1996.
- [29] Honghui He, Nan Zeng, E. Du, Yihong Guo, Dongzhi Li, Ran Liao, and Hui Ma. A possible quantitative Mueller matrix transformation technique for anisotropic scattering media. *Photonics and Lasers in Medicine*, 2(2):129–137, 2013.
- [30] R. M. A. Azzam. Propagation of partially polarized light through anisotropic media with or without depolarization: A differential 4 x 4 matrix calculus. *Journal of the Optical Society of America*, 68(12):1756–1767, 1978.
- [31] Craig F. Bohren and Donald R. Huffman, editors. *Absorption and Scattering of Light by Small Particles*. Wiley-VCH Verlag GmbH, Weinheim, Germany, apr 1998.
- [32] Justiniano Casas. *OPTICA*. J. Casas. Librería Pons, Zaragoza (Spain), 1985.
- [33] Jan-Patrick Schäfer. *Implementierung und Anwendung analytischer und numerischer Verfahren zur Lösung der Maxwellgleichungen für die Untersuchung der Lichtausbreitung in biologischem Gewebe*. PhD thesis, Ulm University, 2011.
- [34] J. C. Dainty. *Laser speckle and related phenomena*. Springer-Verlag, second enl edition, 1984.
- [35] W. T. Welford. Laser speckle and surface roughness. *Contemporary Physics*, 21(4):401–412, 1980.
- [36] Hans M. Pedersen. Theory of speckle dependence on surface roughness\*. *Journal of the Optical Society of America*, 66(11):1204–1210, 1976.

- [37] A. M. Hamed, H. El-Ghandoor, F. El-Diasty, and M. Saady. Analysis of speckle images to assess surface roughness. *Optics and Laser Technology*, 36(3):249–253, 2004.
- [38] F. Rodríguez, I. Cotto, S. Dasilva, P. Rey, and K. Van der Straeten. Speckle characterization of surface roughness obtained by laser texturing. *Procedia Manufacturing*, 13:519–525, 2017.
- [39] Haibo Lin and Ping Yu. Speckle mechanism in holographic optical imaging. *Optics Express*, 15(25):16322, 2007.
- [40] A. M. Darskij and V. B. Markov. Measurement of small displacements by speckle holography. *Optics and Laser Technology*, 21(3):193–197, 1989.
- [41] Joseph L. McLaughlin. Focus-position sensing using laser speckle. *Applied Optics*, 18(7):1042, 1979.
- [42] Ilya Alexeev, Ji Wu, Michael Karg, Zeev Zalevsky, and Michael Schmidt. Determination of laser beam focus position based on secondary speckles pattern analysis. *Applied Optics*, 56(26):7413, 2017.
- [43] R. H. T. Bates. Astronomical speckle imaging. *Physics Reports*, 90(4):203–297, 1982.
- [44] Hector J. Rabal Jr. and Roberto A. Braga, editors. *Dynamic Laser Speckle and Applications*. CRC Press, Taylor & Francis, 2009.
- [45] J. W. Goodman. Laser Speckle and Related Phenomena. Topics in Applied Physics. In J.C. Dainty, editor, *Laser Speckle and Related Phenomena. Topics in Applied Physics*, chapter Statistica. Springer-Verlag, Berlin, second enl edition, 1984.
- [46] Qiankai Wang. Discussion on the fully developed speckle field. *Optik*, 124(17):2948–2950, 2013.
- [47] Kausik Basak, M Manjunatha Pranab, and Kumar Dutta. Review of laser speckle-based analysis in medical imaging. *Med Biol Eng Comput*, 50:547–558, 2012.
- [48] Y. Aizu and T. Asakura. Bio-speckle application blood flow. *Optics & Laser Technology*, 23(4), 1991.
- [49] L. Peng, M. R. Melloch, D. D. Nolte, J. J. Turek, M. Mustata, and P. Yu. Time-dependent speckle in holographic optical coherence imaging and the health of tumor tissue. *Optics Letters*, 29(1):68, 2004.
- [50] Lioudmila Tchvialeva, Harvey Lui, David I Mclean, and Tim K Lee. Polarization speckle imaging as a potential technique for in vivo skin cancer detection. *Journal of Biomedical Optics*, 18(6):061211, 2013.
- [51] Rolando J. González-Peña, Roberto A. Braga, Rosa M. Cibrián, and Teresa San Miguel. Monitoring of the action of drugs in melanoma cells by dynamic laser speckle. *Journal of Biomedical Optics*, 19(5):057008, 2014.

- [52] J. A. Pomarico, H. O. Di Rocco, L. Alvarez, C. Lanusse, L. Mottier, C. Saumell, R. Arizaga, H. Rabal, and M. Trivi. Speckle interferometry applied to pharmacodynamic studies: Evaluation of parasite motility. *European Biophysics Journal*, 33(8):694–699, 2004.
- [53] Evelio E. Ramírez-Miquet, Humberto Cabrera, Hilda C. Grassi, Efrén de J. Andrades, Isabel Otero, Dania Rodríguez, and Juan G. Darias. Digital imaging information technology for biospeckle activity assessment relative to bacteria and parasites. *Lasers in Medical Science*, 32(6):1375–1386, 2017.
- [54] Hilda Cristina Grassi, Lisbette C. García, María Lorena Lobo-Sulbarán, Ana Velásquez, Francisco A. Andrades-Grassi, Humberto Cabrera, Jesús E. Andrades-Grassi, and Efrén D.J. Andrades. Quantitative Laser Biospeckle Method for the Evaluation of the Activity of *Trypanosoma cruzi* Using VDRL Plates and Digital Analysis. *PLoS Neglected Tropical Diseases*, 10(12):1–26, 2016.
- [55] Inácio M. Dal Fabbro, Giovanni Rabelo, Héctor J. Rabal, Ricardo Arizaga, Flávio M. Borem, Marcelo Trivi, and Roberto A. Braga. Assessment of Seed Viability by Laser Speckle Techniques. *Biosystems Engineering*, 86(3):287–294, 2003.
- [56] Bernard Drévilion Enric Garcia-Caurel, Razvigor Ossikovski, Martin Foldyna, Angelo Pierangelo and Antonello De Martino. Ellipsometry at the Nanoscale. In M. Losurdo and K. Hingerl, editors, *Ellipsometry at the Nanoscale*, chapter Advanced M, pages 225–256. Springer, 2013.
- [57] Adeeba Fathima, Mahima Sharma B.S., and N. Sujatha. Selective sensitivity of Mueller imaging for tissue scattering over absorption changes in cancer mimicking phantoms. *Optics and Lasers in Engineering*, 102(November 2017):112–118, 2018.
- [58] José J. Gil and Eusebio Bernabeu. A depolarization criterion in Mueller matrices. *Optica Acta Letters*, 32(3):259–261, 1985.
- [59] José J. Gil. On optimal filtering of measured Mueller matrices. *Appl. Opt.*, 55(20):5449, 2016.
- [60] Jose Jorge; Eusebio Bernabeu Gil. Obtainment of the polarizing and retardation parameters of a non-depolarizing optical system from the polar decomposition of its Mueller matrix. *Optik*, 76(2):67–71, 1987.
- [61] Shane R. Cloude. Conditions For The Physical Realisability Of Matrix Operators In Polarimetry. In *Conditions For The Physical Realisability Of Matrix Operators In Polarimetry*, volume 1166, pages 177–185, 1989.
- [62] F. Le Roy-brehonnet and B. Le Jeune. Utilization of Mueller matrix formalism to obtain optical targets depolarization and polarization properties. *Prog. Quarr. Elecrr.*, 21(2):109–151, 1997.
- [63] Razvigor Ossikovski. Interpretation of nondepolarizing Mueller matrices based on singular-value decomposition Razvigor. *J. Opt. Soc. Am. A*, 25(2):473–482, 2008.
- [64] Razvigor Ossikovski. Analysis of depolarizing Mueller matrices through a symmetric decomposition. *J. Opt. Soc. Am. A*, 26(5):1109, 2009.

- [65] Razvigor Ossikovski. Differential matrix formalism for depolarizing anisotropic media. *Optics Letters*, 36(12):2330–2332, 2011.
- [66] M. K. Swami, S. Manhas, P. Buddhiwant, N. Ghosh, A. Uppal, and P. K. Gupta. Polar decomposition of 3 x 3 Mueller matrix: a tool for quantitative tissue polarimetry. *Optics express*, 14(20):9324–9337, 2006.
- [67] J. M. Sanz, C. Extremiana, and J. M. Saiz. Comprehensive polarimetric analysis of Spectralon white reflectance standard in a wide visible range. *Applied Optics*, 52(24):6051, 2013.
- [68] Nirmalya Ghosh, Michael F. G. Wood, Shu-hong Li, Richard D. Weisel, Brian C. Wilson, Ren-Ke Li, and I. Alex Vitkin. Mueller matrix decomposition for polarized light assessment of biological tissues. *Journal of Biophotonics*, 2(3):145–156, 2009.
- [69] Nirmalya Ghosh, Michael F. G. Wood, and I. Alex Vitkin. Mueller matrix decomposition for extraction of individual polarization parameters from complex turbid media exhibiting multiple scattering, optical activity, and linear birefringence. *Journal of Biomedical Optics*, 13(4):044036, 2008.
- [70] Satish Kumar, Harsh Purwar, Razvigor Ossikovski, I Alex Vitkin, and Nirmalya Ghosh. Comparative study of differential matrix and extended polar decomposition formalisms for polarimetric characterization of complex tissue-like turbid media. *Journal of biomedical optics*, 17(10):105006, 2012.
- [71] H. Arwin, A. Mendoza-Galván, R. Magnusson, A. Andersson, J. LAndin, K. Järrendahl, E. García-Caurel, R. Ossikovski, and H. Arwin. Structural circular birefringence and dichroism quantified by differential decomposition of spectroscopic transmission Mueller matrices from *Cetonia aurata*. *Optics Letters*, 41(14):3293–3296, 2016.
- [72] Honghui He, Jintao Chang, Chao He, and Hui Ma. Transformation of full 4 x 4 Mueller matrices: a quantitative technique for biomedical diagnosis. *Proc. of SPIE*, 9707(April):97070K, 2016.
- [73] Chao He, Honghui He, Jintao Chang, Yang Dong, Shaoxiong Liu, Nan Zeng, Yonghong He, and Hui Ma. Characterizing microstructures of cancerous tissues using multispectral transformed Mueller matrix polarization parameters. *Biomedical Optics Express*, 6(8):2934, 2015.
- [74] Wei Sheng, Weipeng Li, Ji Qi, Teng Liu, Honghui He, and Yang Dong. Quantitative Analysis of 4 × 4 Mueller Matrix Transformation Parameters for Biomedical Imaging. *Photonics*, 6(345):1–14, 2019.
- [75] Williamm C. Earnshaw Thomas D. Pollard. *Cell Biology*. Saunders Elsevier, second edi edition, 2004.
- [76] S. Vinjimore Kesavan, F. Momey, O. Cioni, B. David-Watine, N. Dubrulle, S. Shorte, E. Sulpice, D. Freida, B. Chalmond, J. M. Dinten, X. Gidrol, and C. Allier. High-throughput monitoring of major cell functions by means of lensfree video microscopy. *Scientific Reports*, 4:1–11, 2014.
- [77] Raghu Kalluri and Robert A. Weinberg. The basics of epithelial-mesenchymal transition. *The Journal of Clinical Investigation*, 119(6):1420–1428, 2009.

- [78] Thilo Baronsky, Daja Ruhlandt, Bastian Rouven Brückner, Jonas Schäfer, Narain Karedla, Sebastian Isbaner, Dirk Hähnel, Ingo Gregor, Jörg Enderlein, Andreas Janshoff, and Alexey I. Chizhik. Cell-Substrate Dynamics of the Epithelial-to-Mesenchymal Transition. *Nano Letters*, 17(5):3320–3326, 2017.
- [79] Noel M. Rysavy, Lori M. N. Shimoda, Alyssa M. Dixon, Mark Speck, Alexander J. Stokes, Helen Turner, and Eric Y. Umemoto. Beyond apoptosis : The mechanism and function of phosphatidylserine asymmetry in the membrane of activating mast cells. *BioArchitecture*, 4(4-5):127–137, 2014.
- [80] Sefhra N. Rampersad. Multiple applications of alamar blue as an indicator of metabolic function and cellular health in cell viability bioassays. *Sensors (Switzerland)*, 12(9):12347–12360, 2012.
- [81] Warren Strober. Trypan Blue Exclusion Test of Cell Viability. *Current protocols in immunology / edited by John E. Coligan ... [et al.]*, 21(1):1–3, 2001.
- [82] P. Y. Liu, L. K. Chin, W. Ser, H. F. Chen, C.-M. Hsieh, C.H. Lee, K.-B. Sung, T. C. Ayi, P. H. Yap, B. Liedberg, K. Wang, T. Bourouina, and Y. Leprince-Wang. Cell refractive index for cell biology and disease diagnosis: past, present and future. *Lab on a chip*, 16(4):634–644, 2016.
- [83] Andreas H. Hielscher, Judith R. Mourant, and Irving J. Bigio. Influence of particle size and concentration on the diffuse backscattering of polarized light from tissue phantoms and biological cell suspensions. *Applied Optics*, 36(1):125–135, 1997.
- [84] Lixun Sun, Yuquan Zhang, Yijia Wang, Chonglei Zhang, Changjun Min, Yong Yang, Siwei Zhu, and Xiaocong Yuan. Refractive index mapping of single cells with a graphene-based optical sensor. *Sensors and Actuators B: Chemical*, 242:41–46, 2017.
- [85] F. Carmagnola, J. M. Sanz, and J. M. Saiz. Development of a Mueller matrix imaging system for detecting objects embedded in turbid media. *Journal of Quantitative Spectroscopy and Radiative Transfer*, 146:199–206, 2014.
- [86] Juan Marcos Sanz and Textil Santanderina. Polar decomposition of the Mueller matrix: a polarimetric rule of thumb for square-profile surface structure recognition. *Applied Optics*, 50(21), 2015.
- [87] J. M. Sanz Casado. *Polarimetría de sistemas difusores con microestructuras: efector de difusión múltiple*. PhD thesis, Universidad de Cantabria, 2010.
- [88] Dennis H. Goldstein. Mueller matrix dual-rotating retarder polarimeter. *Applied Optics*, 31(31):6676, 1992.
- [89] Sang Hyuk Yoo, Razvigor Ossikovski, and Enric Garcia-Caurel. Experimental study of thickness dependence of polarization and depolarization properties of anisotropic turbid media using Mueller matrix polarimetry and differential decomposition. *Applied Surface Science*, 421:870–877, 2017.
- [90] Cheryl M. Koh. *Preparation of Cells for Microscopy using Cytospin*, volume 533. Elsevier Inc., 1 edition, 2013.
- [91] Debao Wang, Dabin Yu, Mingwang Shao, Xianming Liu, Weichao Yu, and Yitai Qian. Dendritic growth of PbS crystals with different morphologies. *Journal of Crystal Growth*, 257(3-4):384–389, 2003.

- [92] Zewei Quan, Chunxia Li, Xiaoming Zhang, Jun Yang, Piaoping Yang, Cuimiao Zhang, and Jun Lin. Polyol-Mediated Synthesis of PbS Crystals : Shape Evolution and & DESIGN 2008. *Cryst. Growth Des*, 8(7):2384–2392, 2008.
- [93] Simple Solution Route. Hierarchical , Star-Shaped PbS Crystals Formed by a 2004. *CRYSTAL GROWTH & DESIGN*, 4(2):351–354, 2004.
- [94] Simple Aqueous and Phase Route. Shape Controllable Preparation of PbS Crystals by a 2004. *CRYSTAL GROWTH & DESIGN 2004*, 4(4):759–764, 2004.
- [95] Christina Westmose Yde and Olaf Georg Issinger. Enhancing cisplatin sensitivity in MCF-7 human breast cancer cells by down-regulation of Bcl-2 and cyclin D1. *International Journal of Oncology*, 29(6):1397–1404, 2006.
- [96] Praseetha Prabhakaran, Foteini Hassiotou, Pilar Blancafort, and Luis Filgueira. Cisplatin Induces Differentiation of Breast Cancer Cells. *Frontiers in Oncology*, 3(June):1–10, 2013.
- [97] Amélie Rebillard, Xavier Tekpli, Olivier Meurette, Odile Sergent, Gwenaëlle LeMoigne-Muller, Laurent Vernhet, Morgane Gorria, Martine Chevanne, Markus Christmann, Bernd Kaina, Laurent Counillon, Erich Gulbins, Dominique Lagadic-Gossmann, and Marie Thérèse Dimanche-Boitrel. Cisplatin-induced apoptosis involves membrane fluidification via inhibition of NHE1 in human colon cancer cells. *Cancer Research*, 67(16):7865–7874, 2007.
- [98] Douglas J. Taatjes, Burton E. Sobel, and Ralph C. Budd. Morphological and cytochemical determination of cell death by apoptosis. *Histochemistry and Cell Biology*, 129(1):33–43, 2008.
- [99] Punya Shrivastava, Ajit Sodhi, and Priya Ranjan. Anticancer drug-induced apoptosis in human monocytic leukemic cell line U937 requires activation of endonuclease(s). *Anti-Cancer Drugs*, 11(1):39–48, 2000.
- [100] Vadim A. Frolov, Anna V. Shnyrova, and Joshua Zimmerberg. Lipid Polymorphisms and Membrane Shape. *Cold Spring Harb Perspect Biol.*, 3(11):1–14, 2011.
- [101] A. J. Miles and B. A. Wallace. Chem Soc Rev Circular dichroism spectroscopy of membrane proteins. *Chemical Society Reviews*, 45(18):4859–4872, 2016.
- [102] Scott T. Milner, Charles E. Snyder, Ralph H. Colby, Laura Mely Ramírez, and Darrell Velegol. Controlled Flats on Spherical Polymer Colloids. *Langmuir*, 26(10):7644–7649, 2009.
- [103] Marino Arroyo and Antonio Desimone. Relaxation dynamics of fluid membranes. *Physical Review E - Statistical, Nonlinear, and Soft Matter Physics*, 79(3):1–17, 2009.
- [104] Camilla L. Owens, Edgar Schach, Martin Rudolph, and Geoffrey R. Nash. Surface nanobubbles on the carbonate mineral dolomite. *RSC Advances*, 8(62):35448–35452, 2018.
- [105] Huy Bich Nguyen and Jyh Chen Chen. Effect of slippage on the thermocapillary migration of a small droplet. *Biomicrofluidics*, 6(1):1–13, 2012.

- [106] Pablo Peñas-López, Miguel A. Parrales, and Javier Rodríguez-Rodríguez. Dissolution of a CO<sub>2</sub> spherical cap bubble adhered to a flat surface in air-saturated water. *J. Fluid Mech.*, 775:53–76, 2015.
- [107] A.S. Dimitrov, P.A. Kralchevsky, A.D. Nikolov, Hideaki Noshi, and Mutsuo Matsumoto. Contact angle measurements with sessile drops and bubbles. *Journal of Colloid and Interface Science*, 145(1):279–282, 1991.
- [108] Warren J. Jasper and Nadish Anand. A generalized variational approach for predicting contact angles of sessile nano-droplets on both flat and curved surfaces. *Journal of Molecular Liquids*, 281:196–203, 2019.
- [109] Enric García-Caurel, A De Martino, and B Drevillon. Spectroscopic Mueller polarimeter based on liquid crystal devices. *Thin Solid Films*, 456:120–123, 2004.
- [110] Eric Compain, Stéphane Poirier, and Bernard Drevillon. General and self-consistent method for the calibration of polarization modulators, polarimeters, and Mueller-matrix ellipsometers. *Appl. Opt.*, 38(16):3490–3502, 1999.
- [111] Nicolas B E Sawyer, Stephen P Morgan, Michael G Somekh, Chung W See, Eugene Astrakharchik-Farrimond, and Boris Y Shekunov. Spherical Particles. *Applied Optics*, 42(22):4488–98, 2003.
- [112] James A. Lock. Ray scattering by an arbitrarily oriented spheroid. II. Transmission and cross-polarization effects. *Applied Optics*, 35(3):515–31, 1996.
- [113] Ovrin and Izen. Imaging of transparent spheres through a planar interface using a high-numerical-aperture optical microscope. *Journal of the Optical Society of America. A, Optics, image science, and vision*, 17(7):1202–13, 2000.
- [114] Max Born, Emil Wolf, A. B. Bhatia, P. C. Clemmow, D. Gabor, A. R. Stokes, A. M. Taylor, P. A. Wayman, and W. L. Wilcock. *Principles of Optics*. Cambridge University Press, Cambridge, 1999.
- [115] Razvigor Ossikovski and Enric Garcia-Caurel. Explicit expressions for the elementary polarization properties of a weakly anisotropic, homogeneous medium. *Optics Letters*, 41(15):3487, 2016.
- [116] A. Brunsting and P. F. Mullaney. Light scattering from coated spheres: model for biological cells. *Applied optics*, 11(3):675–680, 1972.
- [117] Gordon Videen, Dev R. Prabhu, Melvin Davies, Francisco González, and Fernando Moreno. Light scattering fluctuations of a soft spherical particle containing an inclusion. *Applied optics*, 40(24):4054–7, 2001.
- [118] Aysun Adan, Günel Alizada, Yağmur Kiraz, Yusuf Baran, and Ayten Nalbant. Flow cytometry: basic principles and applications. *Critical Reviews in Biotechnology*, 37(2):163–176, 2017.
- [119] Bruce T. Draine and Piotr J. Flatau. Discrete-Dipole Approximation For Scattering Calculations. *Journal of the Optical Society of America A*, 11(4):1491, 2008.
- [120] Bruce T. Draine and Piotr J. Flatau. User Guide for the Discrete Dipole Approximation Code DDSCAT 6.1, 2004.



*"Cause sometimes to stay alive you gotta kill your mind."*  
Migraine (Vessel) - Twenty One Pilots

